STUDIES OF MAGNETOSPHERIC CONVECTION: BALANCED AND UNBALANCED

by

Anna D. DeJong

A dissertation submitted in partial fulfillment
of the requirements for the degree of
Doctor of Philosophy
(Atmospheric and Space Sciences)
in The University of Michigan
2008

Doctoral Committee:

Professor C. Robert Clauer, Co-Chair
Associate Professor Aaron Ridley Co-Chair
Professor Dennis S. Bernstein
Associate Professor Michael Liemohn
James Spann, NASA Marshall Space Flight Center

I would like to dedicate my thesis to my father, Gary DeJong. He has always been a scientific inspiration to me and I think he would be very proud of me receiving a Ph.D. in Space Science. I miss him very much.

ACKNOWLEDGEMENTS

I would like to thank my husband, Jared, for all of his help and support while I was writing my thesis, especially for proof reading. Thank you to my son Keegan for being the cutest and happiest baby ever. Thank you mom and Amity for all your support and love. Special thanks to Xia Cai for all of her help with the sawtooth oscillations. Thank you to both of my advisors Bob Clauer and Aaron Ridley for all of their help and support over the years. I'd also like thank my colleages for all of there help and support with writing IDL codes and understanding data.

TABLE OF CONTENTS

LIST OF FIGURES

Figure

LIST OF TABLES

Table

LIST OF APPENDICES

Appendix

CHAPTER I

Introduction

1.1 Steady Magnetospheric Convection: SMCs

When the interplanetary magnetic field (IMF) is oriented oppositely to that of Earth's intrinsic magnetic field (B_z negative or southward), reconnection between the two field lines can occur. This opens Earth's reconnected magnetic field lines to the solar wind. As the solar wind travels tailward, it carries with it the open field lines. The open field lines enter the magnetotail lobes and eventually reconnect in the plasma sheet at the center of the tail between the northern and southern lobes. These open field lines map to the region poleward of the aurora. Thus, the open closed field line boundary can be approximated by the poleward auroral boundary. Using this boundary, the amount of open magnetic flux in the polar cap (F_{pc}) can be calculated.

Siscoe and Huang [1985] state the following formulation of Faraday's Law:

$$\frac{dF_{pc}(t)}{dt} = \Phi_D(t) - \Phi_N(t). \tag{1.1}$$

Where F_{pc} is the amount of open flux in the polar cap, Φ_D and Φ_N are the dayside and nightside reconnection rates, respectively. Hence, the temporal evolution of the

F_{pc} can indicate a balance or imbalance of reconnection rates [*Siscoe and Huang*, 1985; *Cowley and Lockwood*, 1992]. If the dayside reconnection rate, also known as the merging rate, is greater than the nightside reconnection rate, then the amount of F_{pc} increases. This occurs during the growth phase of a substorm. Because the merging rate is higher, the open field lines load the tail region, and hence the polar cap, with magnetic flux. Conversely, when the reconnection rate on the nightside is greater than the merging rate the magnetic flux is unloaded from the tail, causing the F_{pc} to decrease. This occurs during the expansion phase of a substorm. If the merging rate and the nightside reconnection rate balance, then the F_{pc} remains steady ($dF_{pc}(t)/dt = 0$) and a steady magnetospheric convection event (SMC) ensues.

Periods of magentospheric activity without substorm signatures have been termed "convection driven negative bays" [*Pytte et al.*, 1978] or steady magnetospheric convection (SMC) events [*Sergeev*, 1977]. However, the definition of an SMC most commonly used today was expounded by *Sergeev and Lennartsson* [1988] as:

1. stable, continuously southward IMF for more than 4-6 hours,

2. enhanced convection during that period (AE $\geq$ 200 nT),

3. no substorm signatures in ground-based data,

4. no current sheet disruptions or plasmoid releases in the near-Earth magnetotail.

While this definition has been used for many years, it possesses limitations. Principle among these is that it does not describe a physical state of the magnetosphere. Instead, this definition describes one phenomenon, SMCs, by the lack of another phenomenon, substorms. Since substorm signatures in data can be interpreted differently, it is difficult to definitively state whether or not a substorm has occurred.

Also, this definition of an SMC describes a magnetospheric event by its solar wind drivers. Thus, a new, physical definition of SMCs is needed: A balance of reconnection rates on the dayside and nightside of the magnetosphere. This balance of reconnection rates occurs when large scale convection is steady in the magnetosphere. Thus, it describes the physical state of the magnetosphere during an SMC event.

Not only is the current definition of a steady magnetospheric convection event not physically intuitive neither is its name. This name implies that the entire magnetosphere must remain steady during an SMC. This is not so. When convection is steady on a large scale, it is not always steady on a small scale. Some SMCs have a slow evolution in AE, AL and D_{st}, while others may have small perturbations in the data. One type of perturbation observed during SMCs are pseudo-breakups, or auroral brightenings that appear to be the onset of a substorm expansion phase [*Sergeev et al.*, 1996]. However, the expansion never occurs and the brightening never moves polarward [*Akasofu*, 1964]. Because these variations occur in the data and the magnetosphere is not absolutely steady, a new name is proposed – Balanced Reconnection Interval (BRI). This name better describes the physical state of the magnetosphere during these events.

If the reconnection rates are truly balanced, then the open-closed boundary, and hence the amount of open magnetic flux in the polar cap (F_{pc}), should remain steady. Thus, this new definition allows us to utilize the F_{pc}, which is derived using data from the Polar UVI and IMAGE FUV instruments, to identify BRI/SMC events. If the F_{pc} is fairly steady for at least 3 hours and there are no other signs of a substorm during that period, then the event is grouped as a BRI/SMC. Thus, the name balanced reconnection intervals allows for a more precise and physical description of these type of events, eliminating confusion over the term "steady". By using the F_{pc} to

identify these events, a larger range of activity levels and more diverse events can be included in this classification. Furthermore, the F_{pc} measures the beginning and end times of event more accurately, allowing the entire event and only the event to be studied.

While there have been numerous studies of BRIs/SMCs, none of them have utilized polar cap open magnetic flux (F_{pc}) as a selection criteria. Until now, F_{pc} has been used only to support other data, rather than as a way to determine if an event is an SMC [*Yahnin et al.*, 1994]. *Sergeev et al.* [1996] studied several SMC events, but were limited to 5 due to lack of coverage in the magnetotail. The global coverage did, however, allow them to do a very detailed analysis of the magnetospheric dynamics during these events. *Yahnin et al.* [1994] also did an in-depth study on features occurring in the November 24, 1981 SMC. While these investigations illuminated many features of steady magnetospheric convection, there has been a lack of statistical analysis of SMCs. *O'Brien et al.* [2002] presented a large scale statistical study of SMCs, but their selection criteria was only that AL(t)-AL(t-1min) $\leq$ -25 nT. This led them to find SMCs that occured during weaker periods of geomagnetic activity. They also imposed no time limit on the events, so substorm recovery phases were most likely included in their study.

Tanskanen et al. [2005] used Geotail data to study loading and unloading phases along with BRIs/SMCs. Their analysis supported *O'Brien et al.* [2002]; *Sergeev et al.* [1996], finding that BRIs/SMCs are more likely to occur when the 0 nT $>$ IMF $B_z \geq$ -5 nT. Furthermore, approximately half of their 28 SMCs had bursty bulk flows (BBF) in the tail. *Hughes and Bristow* [2003] studied the Harang discontinuity during two SMCs and found that convection patterns during SMCs were typical for southward IMF. Recently, *Goodrich et al.* [2007] ran a Lyon-Fedder-Mobarry (LFM)

global MHD simulation of an SMC. Their findings of "an intense current sheet in the inner magnetosphere and a thick midtail plasma sheet" supported the global convection pattern put forth by *Sergeev et al.* [1996]. When they increased the IMF B_z, thus increasing the merging rate, by 50 % in magnitude, they still had a case of quasi-steady reconnection in the tail. The stronger B_z created a reconnection line that was closer to Earth. This caused a more dipolar inner magnetosphere and produced a wide auroral oval, corroborating findings by *Yahnin et al.* [1994].

All of these studies are important for understanding BRIs, but this dissertation provides the first true measure of convection during these events. It is also the first time that both Polar UVI and IMAGE FUV data are used in conjunction in a single study. Finally, no one has yet to do a comparative study of three different modes of convection: (1) isolated substorms, (2) sawtooth injections, and (3) BRIs.

Before a detailed description of the three different modes of convection is given, we must first understand the basics of Earth's magnetosphere and its interactions with the solar wind and interplanetary magnetic field (IMF).

1.2 The Earth's Magnetosphere

1.2.1 The Sun and solar wind

The Sun's energy is driven by the nuclear fusion of hydrogen that occurs deep within its core. This energy is transferred through the different layers of the Sun by radiation and convection. After passing through these layers it will eventually reach the photosphere, or the surface of the sun, and continue on to the atmosphere. This atmosphere or, solar corona, has a temperature of approximately 1,000,000 Kelvin.

The convection of hot plasma on the surface of the Sun creates a magnetic field. This magnetic field continually changes and reverses polarity every 11 years. During

this 11 year interval the Sun's magnetic field changes from a magnetic dipole state to a more complex magnetic field. As the magnetic field lines twist, they inhibit convection and a local area of cooler plasma forms. This cool plasma appears as a dark spot on the photosphere and is referred to as a sun spot. The number of sun spots is directly related to the complexity of the Sun's magnetic field. When the Sun is in a dipole state, solar minimum, there are very few sun spot. As the magnetic field lines begin twist the number of sun spots increase and will reach a maximum, solar maximum, approximately 5.5 years after the minimum. After solar maximum is reached the field lines will begin to untwist and the sun spot number will begin to decrease until solar minimum is once again achieved. The new solar minimum will have a polarity that is opposite to previous solar minimum. Thus, the complete cycle take 22 years.

Due to the extreme pressure in the solar corona and low pressure of interplanetary space, the Sun's corona expands radially outward into the solar system. This expansion causes solar plasma to be expelled from the Sun in the form of solar wind [*Parker*, 1958]. The solar wind plasma contains mostly hydrogen ions (H^+) (or protons (p^+)) and electrons (e^-). *Parker* [1958] mathematically described the solar wind as a spiral being expelled from the Sun. In 1960, using a simple isothermic model of the solar wind, he showed that by the time the solar wind reaches the Earth it is super-Alfvenic and supersonic [*Parker*, 1960].

Because the solar wind is a plasma it has magnetic properties that allow it to carry a "frozen in" magnetic field as it travels through the interplanetary space. This magnetic field is referred to as the interplanetary magnetic field or IMF. Assuming the simplest magnetic field configuration in the Sun, a dipole, the IMF will become stretched such that the magnetic field lines will become antiparallel at a location

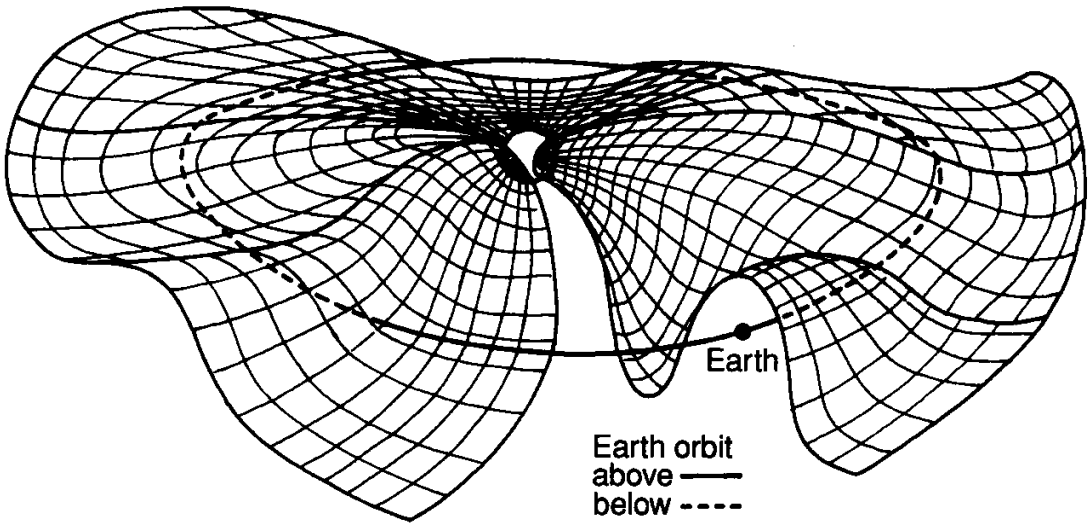

Figure 1.1: Structure of the interplanetary current sheet, "ballerina skirt" [*Kelley*, 1989]

close to the equator. Because these field lines are parallel but opposite in polarity, they create an interplanetary current sheet. Since the rotation of the Sun and its magnetic field are not aligned there is rotational axis to the magnetic field lines. This axis causes the current sheet to take the shape of a ballerina skirt, as shown in Figure 1.1. By the time the solar wind and IMF reach Earth their properties have changed. The average solar wind and IMF values measure at Earth are listed in Table 1.1.

While the solar wind is always traveling out from the Sun, it is not constant. Due to magnetic activity on the surface of the Sun the solar wind and IMF properties fluctuate. A large expulsion matter from the Sun, called a coronal mass ejection (CME), can have a large effect on the solar wind characteristics and the strength of the IMF. CMEs can have great impact on the Earth and its magnetic field.

1.2.2 Regions of Earth's magnetosphere

Due to its molten core the Earth has an intrinsic magnetic field. This magnetic field has a tilt angle of $\sim 11^\circ$ with respect to the rotational axis and a dipole mo-

Table 1.1: The average solar wind and IMF values at Earth (1 AU)

Quantity	Value
Electron density	7.1 cm^3
Flow speed	450 km/s
Temperature (proton)	1.2 x 10^5 K
Magnetic field	7.0 nT
Acoustic speed	60 km/s
Alfven speed	40 km/s

ment of approximately 7.84×10^{15} T $\cdot$ m^3. The polarity of Earth's magnetic field is opposite to its geographic poles, the magnetic north pole is in the southern hemisphere. Because magnetic field lines are always drawn with arrows pointing from the north magnetic pole to the south magnetic pole, the Earth's magnetic field lines are drawn with arrows pointing to the geographic north pole. When ever the magnetic North pole or northern magnetic field is discussed in this dissertation it is the pole, or magnetic field, that occurs in the geographic north.

Because the Earth is an object in the supersonic solar wind it has a bow shock. This shock is collisionless and is created as the supersonic and superalfvenic solar wind slows to subsonic and subalfvenic speeds. As the solar wind plasma passes through the bow shock its kinetic energy is converted to thermal and magnetic energy, thus heating and slowing the plasma. Thermal and magnetic pressure are created as the solar wind ram pressure interacts with the bow shock.

After passing through the Earth's bow shock the solar wind particles enter the magnetosheath, see Figure 1.2. They will then encounter the magnetopause. The magnetopause is a boundary layer that balances the magnetic pressure of the Earth against the combined magnetic and thermal pressures in the magnetosheath. In order to create this balance currents must flow along the magnetopause. These currents will be discussed in more detail later in the chapter.

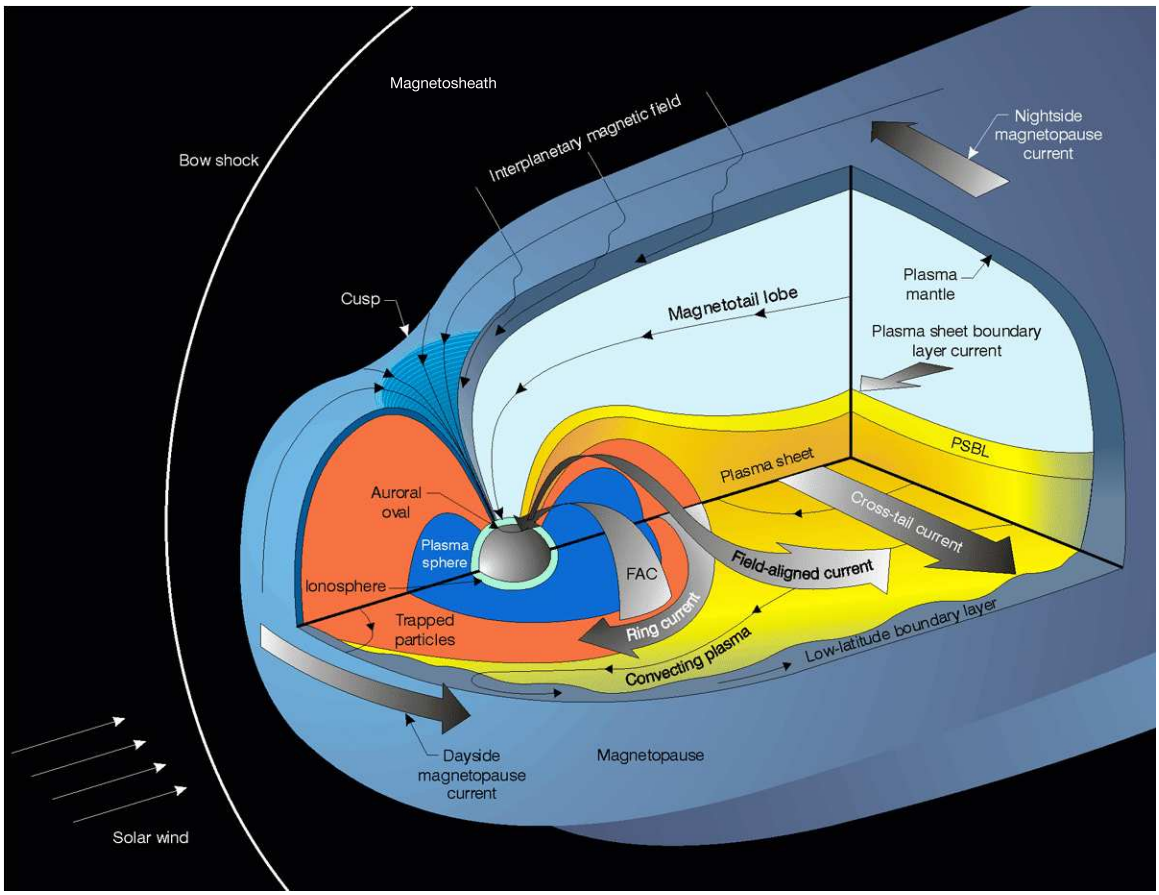

Figure 1.2: A general picture of the Earth's magnetosphere

The region of space bounded by the magnetopause is referred to a the magnetosphere and may be separated into a dayside and nightside. The nightside stretches from the Earth in the anti-Sunward direction and is designated the magnetotail. As can be seen in Figure 1.2, the magnetotail region is comprised of the plasma mantle, tail lobes, plasma sheet boundary layers, and the central plasma sheet. The plasma mantle is a high latitude region of current systems that allows the interplanetary magnetic fields to balance the Earth's intrinsic magnetic field and is typically considered to be just tailward of the cusp. The tail lobes contain plasma that is diffuse, (0.01 cm^3) and magnetic fields with an average strength of 20 nT. This combination of low density and high magnetic field causes a low plasma Beta, the ratio of

thermal pressure to magnetic pressure. The magnetotail lobes can be separated into north and south lobes. The field lines in each lobe are stretched until they become anti-parallel. In other words, the field lines in the north lobe are directed toward the Earth whereas the field lines in the south lobe are directed away from the Earth. These parallel, yet oppositely directed, field lines create a need for a cross tail current to form in the central plasma sheet that separates them. This current or plasma sheet has a relatively large density (0.3 cm^3) and a reduced magnetic field strength (10 nT), which causes a large plasma beta (~ 10). Due to electric fields imposed by the solar wind, plasma from the plasma sheet is convected earthward into the inner magnetosphere.

1.2.3 Ionosphere

Another important component of the magnetosphere is its coupling to the ionosphere through a series of field aligned current systems, which will be discussed in the next section. The ionosphere is the ionized region of Earth's upper atmosphere that ranges from 60 km to 1000 km. The ionosphere can be separated into different regions (D, E, F1 and F2) using the maximum electron density at each region, see Figure 1.3. From this figure, it can be seen that the dayside electron densities are higher than the nightside. This is because the ions and electrons densities are enhanced by dayside photoionization. The main sources of ionization on the nightside are transport from the dayside and production due to magnetospheric particle precipitation.

At high latitudes, conductance in the ionosphere plays large role in its connection to the magnetosphere. Charge particles can flow into the ionosphere along the Earth's magnetic field lines, $\mathbf{B}$, the currents that are formed from the flow of these particles

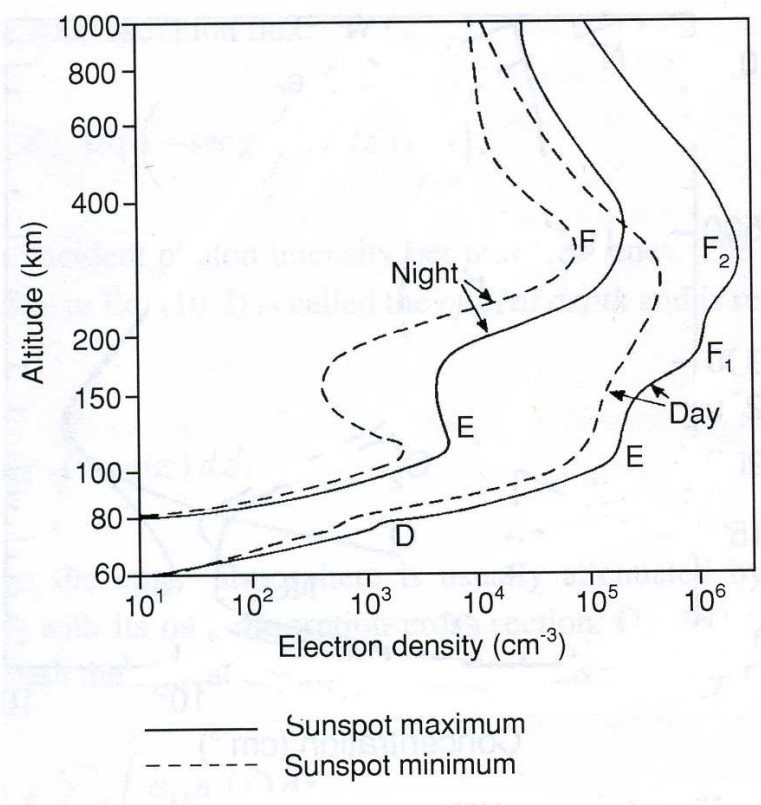

Figure 1.3: Typical vertical profile of the electron density in the midlatitude ionosphere [*Hargreaves*, 1992]

are called Birkeland Currents or Field Aligned Currents (FAC). Due to the imposed electric field from the IMF, currents in the ionosphere can also flow perpendicular to $\mathbf{B}$. The currents that flow parallel to $\mathbf{E}_\perp$ are called Pederson Currents and those that flow in the $\mathbf{E}_\perp \times \mathbf{B}$ are Hall Currents. From Ohm's law, we know that $\mathbf{j} = \sigma\mathbf{E}$. In the ionosphere this becomes, $\mathbf{j} = \sigma_P\mathbf{E}_\perp - \sigma_H(\mathbf{E}_\perp \times \mathbf{b}) + \sigma_o\mathbf{E}_\parallel$, where parallel and perpendicular reference orientation to $\mathbf{B}$ and σ_o, σ_P and σ_H are the specific, Pederson and Hall conductivities respectively. Because the electron-neutral collision frequency is much less than the electron gyroradius, the Pederson conductivity relies only on ions while the Hall conductivity relies on both ions and electrons. When the ion-neutral collision frequency is low (higher altitude), the ions and electrons

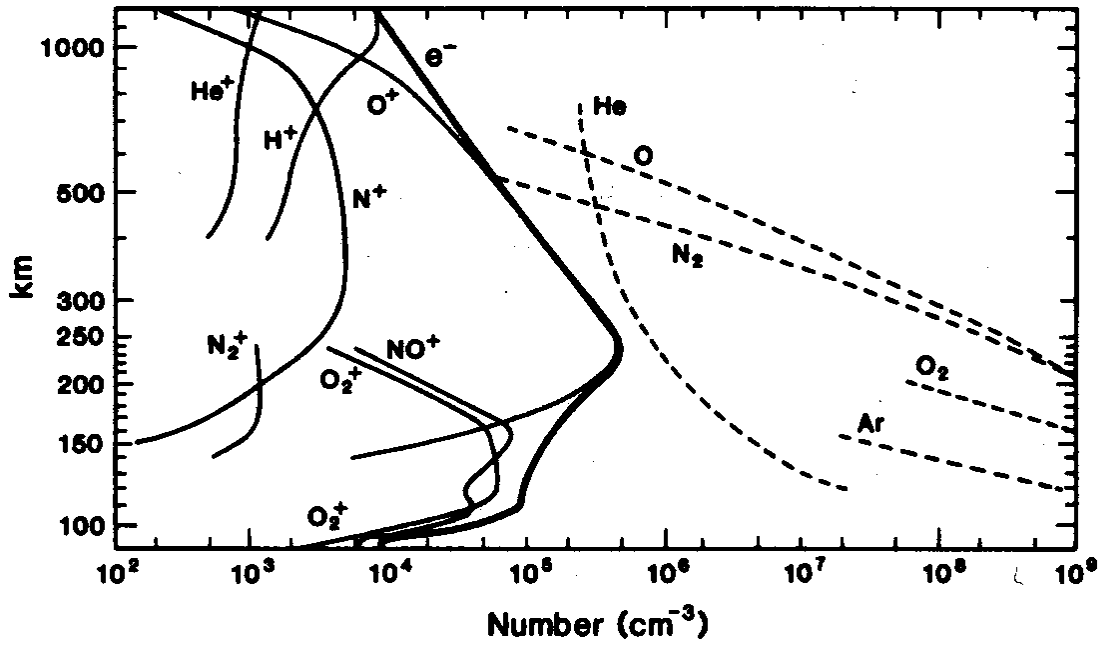

Figure 1.4: Typical vertical profile of the ion and neutral densities in the midlatitude ionosphere. [*Johnson*, 1969]

will $\mathbf{E} \times \mathbf{B}$ drift in the same direction, thus creating no current. The ion-neutral collision frequency becomes substantial in the D and E regions thus allowing only the electrons to $\mathbf{E} \times \mathbf{B}$ drift. Because of this, the Hall currents only play a role in the D and E regions of the ionosphere. The Pederson currents, on the other hand, flow throughout the ionosphere. Both Pederson and Hall conductivities peak between 90 and 140 km above the Earth. Figure 1.5 is from *Kelley* [1989] and shows a plot of the conductivity vs altitude for the three primary conductivities.

1.2.4 Formation of the aurora

Auroral emissions in the ionosphere are primarily caused by precipitating electrons from the magnetosphere. Diffuse aurora occurs at all times and is created

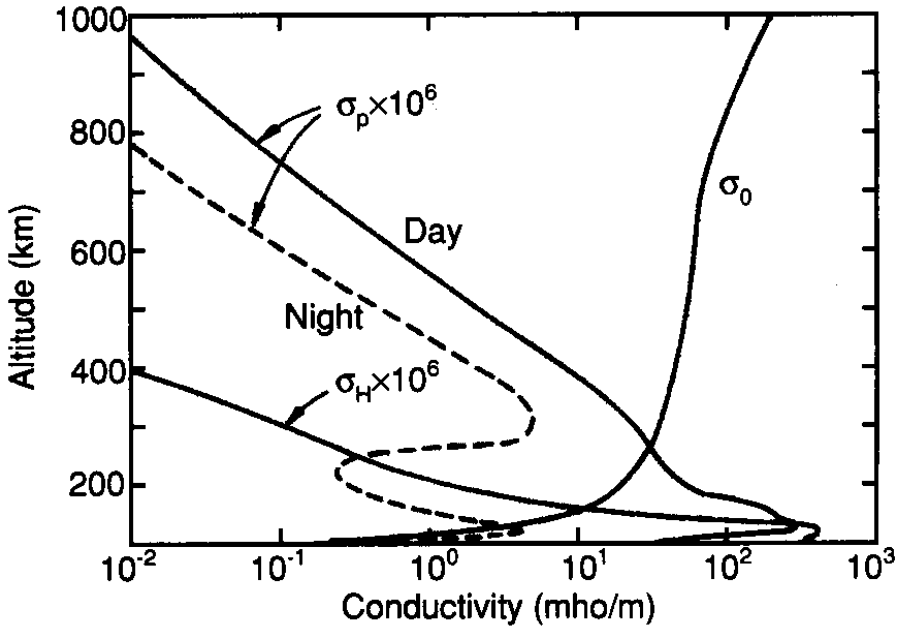

Figure 1.5: Vertical profile of the different ionospheric conductances [*Kelley*, 1989]

mostly by electrons that fall into the loss cone when traveling through the inner magnetosphere. Once in the loss cone, the electrons will travel into the ionosphere where they react with neutrals and create auroral emissions. Discrete aurora, on the other hand, occurs during active times. These auroral emissions are created by precipitating energetic electrons along field-aligned currents.

The kinetic energy from auroral particles can be deposited into the ionosphere by: (1) collisions that lead to transitional, vibrational and rotational energization of atoms and molecules, (2) the impact-exciation of bound electrons from their ground state to an excited state, or (3) electron ionization caused by impacts [*Jones*, 1974]. These different options lead to auroral emissions in the ultraviolet (UV), visible, and infrared (IR) spectrums. The emissions contain atomic lines and molecular-band spectra of the primary constituents of the upper atmosphere, plus some minor

species. The optical-emission wavelength λ, in nanometers is related to the energy released in keV by $E = 1.240/\lambda$. The visible auroral emissions are created by N_2 (blue),

$$N_2 + e \longrightarrow (N_2^+)^* + e' + e_n \tag{1.2}$$

$$(N_2^+)^* \longrightarrow +h\nu(391.4 + 427.8nm) \tag{1.3}$$

Oxygen (green),

$$O(^3P) + e \longrightarrow O(^1S) + e' \tag{1.4}$$

$$O(^1S) \longrightarrow O(^1D) + h\nu(557.7nm) \tag{1.5}$$

and O (red),

$$O(^3P) + e \longrightarrow O(^1D) + e' \tag{1.6}$$

$$O(^1D) \longrightarrow O(^3P) + h\nu(630/636.4nm), \tag{1.7}$$

where e' has less energy than e.

An example of auroral emission in the ultraviolet are those created by N_2:

$$N_2(X^1\Sigma_g^+) + e \longrightarrow N_2(a^1\Pi_g) + e' \tag{1.8}$$

$$N_2(a^1\Pi_g) \longrightarrow N_2(X^1\Sigma_g^+) + h\nu(LBH) \tag{1.9}$$

where LBH is the Lyman Birge Hopfield spectrum that ranges from about 135 nm to 180 nm. Because of the vertical variation in composition of the thermosphere, different aurora take place at different altitudes, ranging from 100 to 300 km above the Earth. The peak of auroral emissions however is not solely dependent on the peak density of the molecule or atom being excited. Due to a long transition time, O(^{1}D)

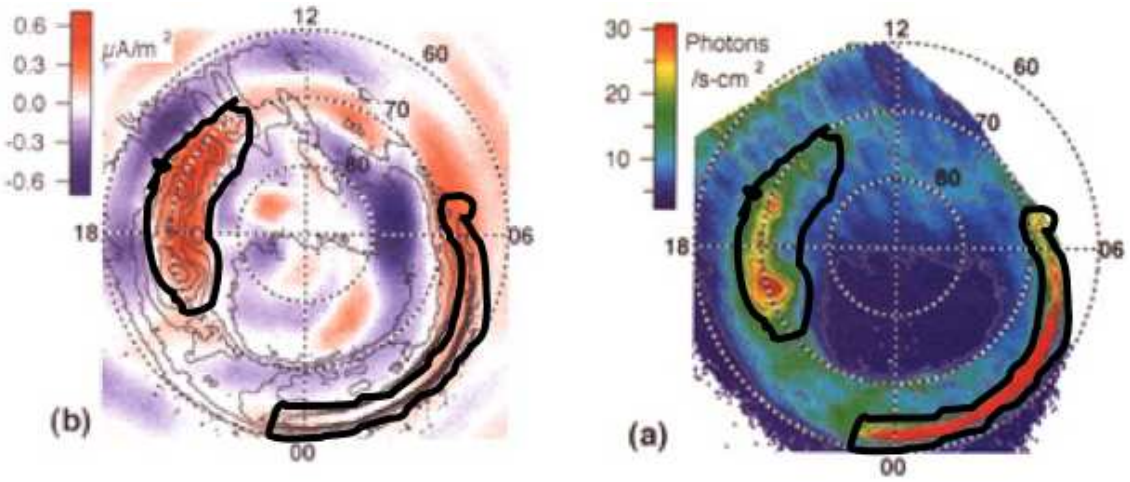

Figure 1.6: (a) FACs as determined by Iridium array of satellites, highlighted are the downward FAC. (b) Auroral image from POLAR UVI for the same day as the image on the left, highlighted is the brightest aurora. Note that the bright aurora and the upward FACs overlap.

is likely to experience a collision before it has a chance to emit a photon. Thus, the 630 nm emission line is expected to peak above 200 km, even though the expected peak of O(^{1}D)is near 100 km [*Carlson and Egeland*, 1995]. The LBH emission tends to peak between 120 and 140 km [*Meier et al.*, 1982].

Discrete auroral emissions, as mentioned earlier, are created by the flow of electrons from the magnetosphere into the ionosphere via field-aligned currents. The upward flowing FACs are downward flowing electrons. Thus, the discrete auroral emissions overlap with the upward FACs, see Figure 1.6. The cusp region is another route electrons can follow, causing aurora on the dayside of the ionosphere. During active times in the magnetosphere, currents flow from the plasma sheet to the ionosphere via the substorm current wedge. This causes a large amount of energetic electrons to flow into the night side ionosphere, thus causing significant auroral displays during substorms.

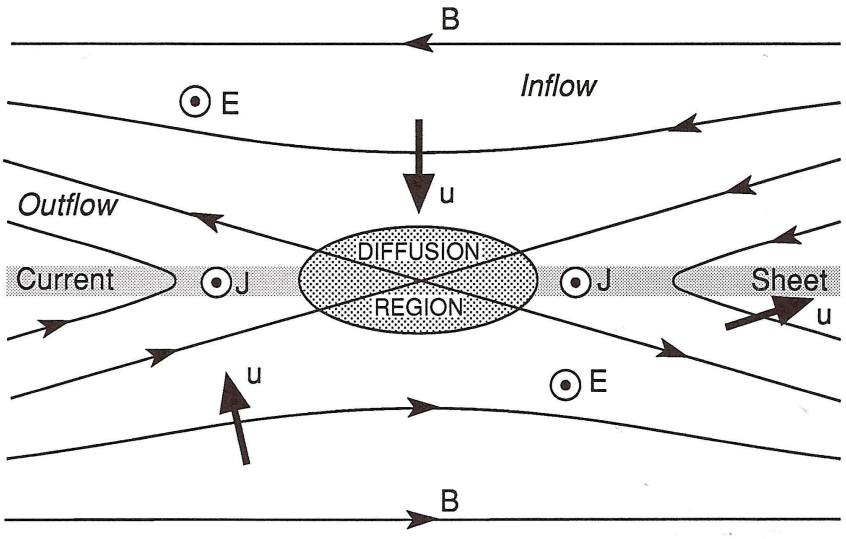

Figure 1.7: Schematic of magnetic reconnection. Magnetic field lines (**B**) flow inward into the diffusion region where they are cut and reconnected. They then flow outward along the sides [*Hughes*, 1995].

The atmosphere does not only give off emissions in the auroral zone but also in the form of dayglow or "airglow" [*Chamberlain*, 1961]. Emissions are considered dayglow if solar radiation is the initial source of energy. Thus, the difference between dayglow and auroral emissions is how they are formed. Dayglow is created by photoelectrons while auroral emissions are created by precipitating electrons.

1.2.5 Magnetic reconnection

Due to its magnetic properties, when plasma moves on large scales, such as the magnetosphere, it brings with it the magnetic fields, these fields are referred as "frozen in flux". This keeps the plasma tied to one field line, so plasma on one field line, or flux tube, does not interact with plasma from a different flux tube. This leads to the formation of thin boundaries between different plasma regimes. The magnetic fields on either side of the boundary are tangential to the boundary, and the two

fields can have different orientations and strengths. If the magnetic field lines are flowing toward this boundary, the current sheet along the boundary will adjust in thickness to balance the diffusion and convection at the edges of the sheet [*Hughes*, 1995]. Because the current sheet thickness is small compared to the global scale of the system, frozen in flux no longer holds inside the sheet. Thus, plasma is now free to move along different field lines and interact with plasma from other regions.

Figure 1.7 shows a simple model of reconnection occurring at an x-type magnetic neutral line. The E_y out of the page, drives flow inward from the top and bottom and flow outward from both sides. The small shaded region is the diffusion region in which frozen in flux breaks down. Magnetic field lines enter the diffusion region where they are "cut" and "reconnected" to different partners. This processes allows plasma that was once tied to a "closed" flux tube to flow along the newly created "open" flux tube and interact with plasma from other regions. Now, the plasma is free to be exchanged readily and hence mass, energy and momentum [*Hill*, 1975; *Cowley*, 1986].

1.2.6 Convection in the magnetosphere

There are two models of solar wind/IMF interaction with Earth. The first is a shield model suggested by *Axford and Hines* [1961] that says the IMF does not directly interact with the Earth's magnetosphere. Thus, the energy that is gained by the magnetosphere during geomagnetic storms comes from a viscous interaction along the magnetopause [*Axford*, 1964]. It is widely accepted that this model can not provide enough energy to the magnetosphere, and therefore plays only a small role in magnetospheric dynamics. Conversely, the *Dungey* [1961] model states that the IMF interacts with the Earth's magnetic field via reconnection. This reconnection occurs

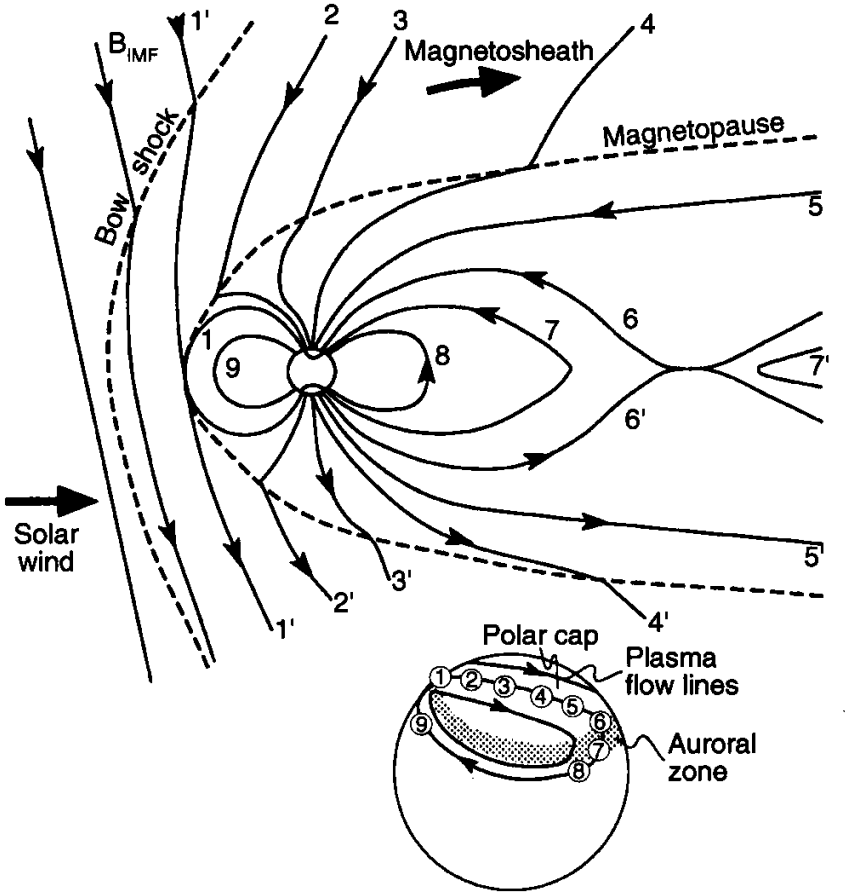

Figure 1.8: Convection of the magnetic fields in the magnetosphere when the IMF B_z is southward, also mapped to the ionosphere.[*Hughes*, 1995]

when the IMF is antiparallel to the Earth's magnetic field. This usually happens when the IMF B_z is oriented southward (negative IMF B_z), see magnetic field lines 1' and 1 on Figure 1.8. The reconnected field lines are considered open field lines because the Earth's magnetic field is now connected to the IMF and therefore open to the solar wind. The open field lines are then convected toward the night side of the magnetosphere by the solar wind (lines 2-5 on Figure 1.8). Eventually the open field lines will reconnect in the tail region, field lines 6' and 6. The foot print of the reconnected field lines maps to the poleward edge of the auroral zone. Hence, the

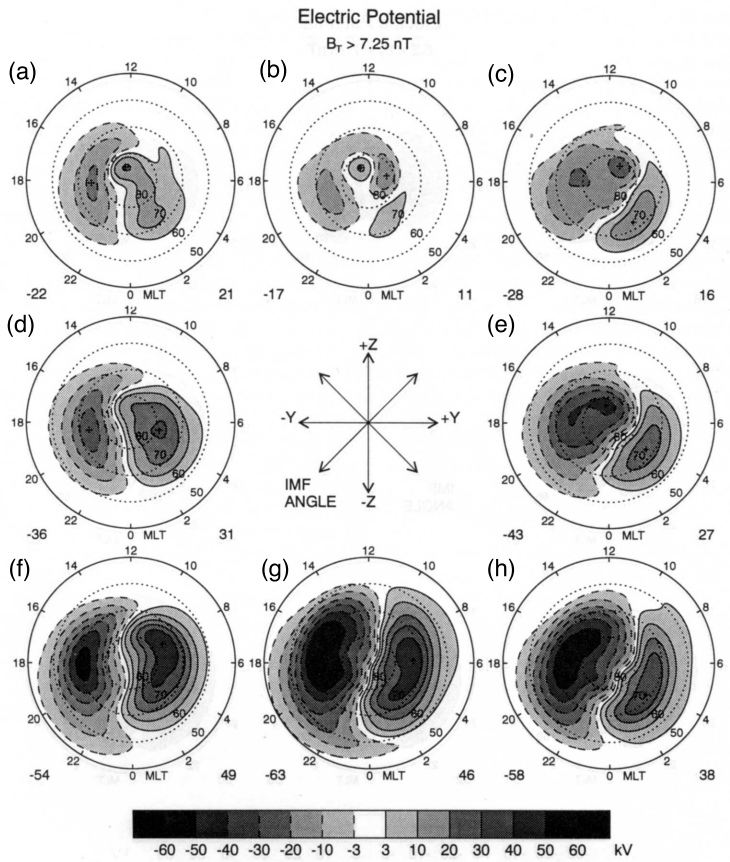

Figure 1.9: Potential patterns in the ionosphere for different IMF orientations [*Weimer*, 1995]. Dotted lines are negative equipotenials and solid lines are positive equipotentials.

poleward edge of the aurora is a proxy for the open-closed boundary because the field lines poleward of the boundary are open and those equatorward are closed. The new closed field lines then convect to the dayside magnetopause to start the process over again.

Because the open magnetic field lines are connected to the IMF, they are moving with the solar wind velocity. Thus, there is an imposed electric field ($\mathbf{E} = -\mathbf{v} \times \mathbf{B}$) in the dawn to dusk direction. The electric field maps to the ionosphere and creates an $\mathbf{E} \times \mathbf{B}$ drift in the antisunward direction across the polar cap. On the closed field

lines, the electric field is dawn to dusk, thus, convecting the plasma back toward the Sun. This plasma flow is depicted by the bottom illustration in Figure 1.8. The combination of the antisunward flow across the polar cap and the sunward flow equatorward of the open-closed boundary creates at two cell convection pattern in the ionosphere. The guiding center drift path of the convecting plasma follows the electric potential pattern in the ionosphere (see Figure 1.9 (g)).

When the IMF is oriented in the northward direction, IMF B_z positive, reconnection takes place in the cusp region. This creates a four cell convection pattern in the ionosphere. The two nightside cells are the similar to those observed during southward IMF, but smaller. The other two cells are associated with the cusp (N B_z) field aligned currents. The dayside cells flow oppositely to those for IMF B_z negative. This pattern can seen in Figure 1.9 (b).

Figure 1.9 shows results from an empirical model of the ionospheric potential patterns for different IMF orientations [*Weimer*, 1995]. As stated above, since the plasma is $\mathbf{E}_\perp \times \mathbf{B}$ drifting the potential patterns and convection patterns are the same. When B_z is positive (negative) and B_y is zero, the four (two) cell pattern discussed above can be seen. IMF B_y can also have an effect on the potential patterns in the ionosphere. When $B_y > 0$, the dawn cell is enhanced, and when $B_y < 0$ the dusk side exhibits the enhancement.

1.3 Magnetospheric Convection Modes

This section describes the three different convection modes that will be studied in this dissertation: (1)isolated substorms, (2) SMCs, and (3) sawtooth injections. Since the classic definition of Steady Magnetospheric Convection (SMC), here referred to as Balanced reconnection intervals (BRIs), relies on the definition of a substorm,

substorms will be explored first.

1.3.1 Substorms

A substorm occurs when energy is transferred from the solar wind/IMF and stored in the magnetotail lobes. This energy is then released into the inner magnetosphere and ionosphere. One of the most common ways to describe a substorm is to use a phenomenological triphasic model that has been developed over years of data collection. This model breaks the substorm into a growth, expansion and recovery phase [*McPherron et al.*, 1973].

There are many different models that describe the magnetospheric dynamics during a substorm. They tend to agree on the processes during the growth and recovery phases but differ in there descriptions of the onset of the expansion phase. The substorm growth phase transfers the solar wind/IMF energy into the magnetotail. When the IMF B_z is negative and magnetic reconnection occurs on the dayside of the magnetosphere, open magnetic field lines convect toward the tail resulting in a build up of magnetic pressure in the tail lobes that stretches the magnetotail. The expansion phase is the release of the tail lobe pressure and energy into the inner magnetosphere and ionosphere. There is still controversy over how this energy and pressure is released. The different phenomenological models are described below:

1. **The Driven Model**

   The Driven model was first described by *Perreault and Akasofu* [1978]. They developed an energy-coupling parameter ϵ, which is defined as $\epsilon = l_o^2 u B^2 \sin^4(\theta/2)$ where $l_o^2 = (6R_E)^2$, is the area on the magnetopause through which magnetic energy (Poynting flux) enters the magnetosphere. In this model, a southward turning IMF enhances the coupling of the solar wind electric field to the iono-

sphere. The substorm expansion phase in this model occurs when the upward field-aligned current density near midnight exceeds a threshold value, causing the field-aligned potential to drop, drawing more current and increasing ionospheric conductivity. Thus, creating a magnetosphere-ionosphere feed back loop. This early substorm model is now considered a small component of other substorm models.

2. **Near Earth Neutral Line (NENL) Model**

   In the near earth neutral line model, the substorm expansion phase begins when magnetic pressure builds up in the tail lobes and causes the plasma sheet to thin. This thin plasma sheet allows the oppositely directed magnetic field lines to get close enough to form a new reconnection point in the magnetotail. This new reconnection point is referred to as the Near Earth Neutral Line (NENL). The formation of the NENL is the onset of the substorm expansion phase [*McPherron et al.*, 1973; *Russell and McPherron*, 1973; *McPherron*, 1991]. After the onset, the magnetic field lines on the earthward side of the NENL dipolarize (become more dipolar like). The field lines downtail from the NENL create a plasmoid which is pulled down the tail by pressure differences in the tail and interplanetary space. The plasma on the Earthward side travels down the plasma sheet toward Earth, where it enters the inner magnetosphere and a substorm current wedge is produced that allows the currents to travel down field lines into the ionosphere (see Figure 1.10).

3. **Current-Sheet-Disruption Model**

   The current-sheet disruption model is similar to the NENL model in that the plasma sheet thins during the growth phase of the substorm for the same rea-

sons. However, in this model, the current becomes unstable due to nonadiabatic ions streaming across the current sheet and interacting with adiabatic electrons drifting in the opposite direction [*Lui et al.*, 1990]. At the same time, the density gradient on the boundary of the plasma sheet drives the lower-hybrid-drift instability. These two instabilities produce an anomalous resistance in the plasma sheet that disrupts the cross-tail current. The current is then diverted along the field lines into the ionosphere. Thus, causing the onset of the expansion phase [*Lui*, 1991]. Subsequently, reconnection is initiated, and the substorm progresses as described in the NENL model.

4. **Magnetosphere-Ionosphere Coupling Model**

   The magnetosphere-ionosphere coupling (MIC) model emphasizes the positive feedback that changes the ionospheric conductivity can have on the sources of field-aligned currents in the magnetotail [*Kan et al.*, 1988; *Rothwell et al.*, 1988]. These models provide possible explanations for the dynamic development of auroral substorm features, such as the surge, Pi-2 pulsation burst and poleward bulge.

The recovery phase of a substorm begins once the energy that was stored in the tail during the growth phase has been released (no matter by which process) and the expansion phase ceases. During the recovery phase, the magnetosphere returns to its ground state. If the IMF is still southward during the recovery phase, the process should start over again with a new growth phase.

The onset of the substorm expansion phase can be detected in many different types of data. In the auroral regions, a geomagnetic index called the auroral index can be used. This index is a measure of the perturbations in the north/south com-

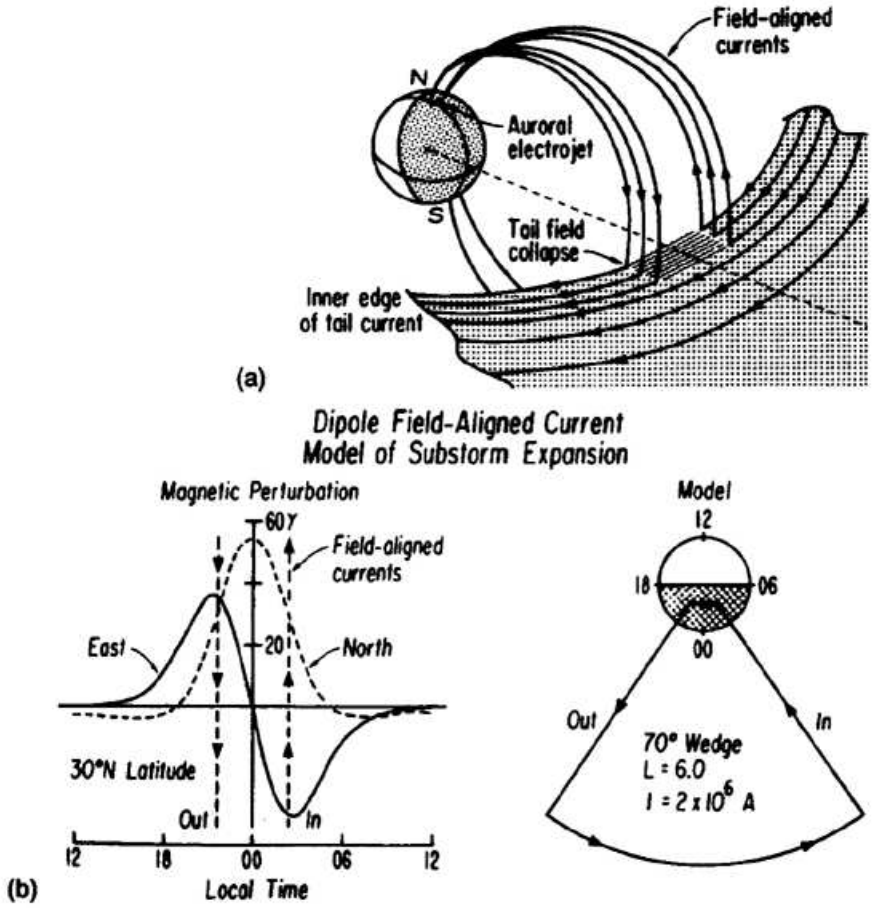

Figure 1.10: (a) The substorm current wedge and associated field aligned currents. (b) Perturbations in the magnetic field at 30 degrees north latitude. [*Clauer and McPherron*, 1974]

ponent of the magnetic field at high latitudes: AU for auroral upper or an eastward current, AL for auroral lower or a westward current and AE, auroral electrojet, for the difference between AU and AL. AL is essentially a measure of the westward electrojet that can be caused by the closing of the FACs that connect the substorm current wedge to the ionosphere. AU therefore measures an eastward current that can occur on the dayside. Since AU is usually much smaller than the AL, AE is representative of the westward surge that can occur in the aurora during substorms.

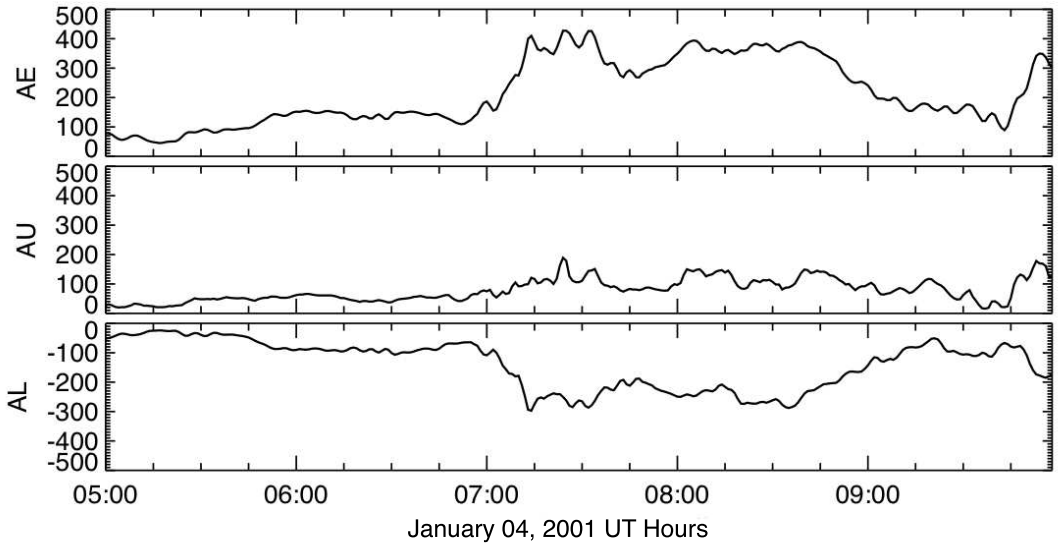

Figure 1.11: AE, AU and AL for the substorm on January 04, 2001. Onset of the expansion phase a 06:52 UT.

A drop in AL, or increase in AE, is often used to indicate the onset of the substorm expansion phase. Figure 1.11 is a plot of AE, AU and AL for the substorm that occurred on January 04, 2001. The onset time of the expansion phase of the substorm is 06:52 UT, at which time AE (AL) starts to increase (decrease). The substorm ends at about 09:15 when the recovery phase ends and AE and AL return to their initial measurements.

While AE and AL are indicators of the substorm current wedge at high latitudes, a mid- latitude positive bay measures the substorm current wedge at mid-latitudes. This positive bay is detected by ground based magnetometers and is an increase in the north/south component of the perturbations in Earth's magnetic field [*McPherron et al.*, 1973]. The increase in the measured magnetic field is caused by a decrease in the tail current in the inner magnetosphere. The tail current is diverted through the substorm current wedge into the high latitude ionosphere, which causes the auroral electrojets. Figure 1.10(a) is a diagram of the substorm current wedge. Figure

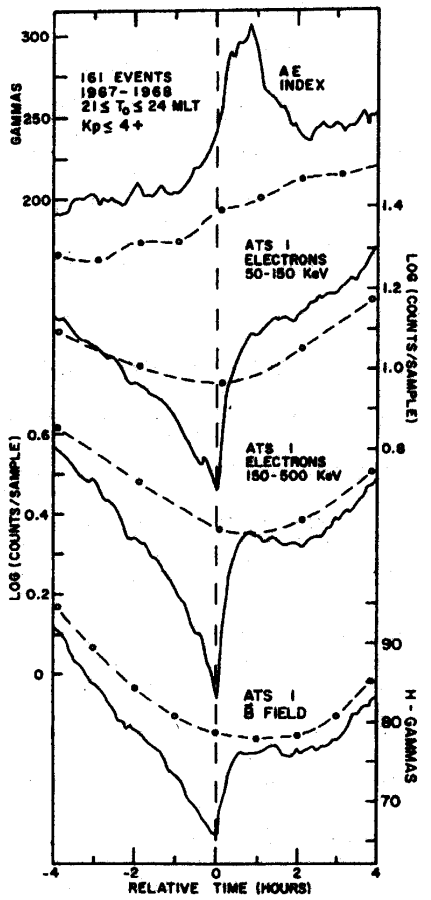

Figure 1.12: Superposed Epoch of Particle injection during a substorm [*Swanson*, 1978].

1.10(b) is a plot of ground based magnetometer readings of the substorm current wedge at 30° N latitude. The dotted line represents the mid-latitude positive bay (north/south component), while the solid line shows the east/west perturbations in the magnetic field.

In magnetometer data, both ground and satellite based, an ultra low frequency (ULF) wave, known as a Pi2 pulsation, is measured during substorm expansion onset. The Pi2 pulsations are in the period range from 40 to 150s [*Jacobs*, 1970]. These pulsations are generated by the onset of field-aligned currents and compressional waves in the near-Earth plasma sheet associated with substorm onsets [*Olson*, 1999].

Magnetospheric substorms can also be detected by geosynchronous satellites. Magnetometers measure changes in the magnetic field configuration, consistent with stretching and dipolarization of the Earth's magnetic field [*Cummings et al.*, 1968; *Kokubun and McPherron*, 1981]. Energetic particles fluxes show a gradual decrease and rapid increase near local midnight [*Sauvaud and Winckler*, 1980; *Erickson et al.*, 1979]. Figure 1.12 shows a superposed epoch analysis of energetic particle fluxes from 161 substorms along with the AE index. During the growth phase of the substorm the decreased particle fluxes correspond to the thinning plasma sheet [*Reeves et al.*, 1996]. The sharp increase in fluxes coincides with the onset of the expansion phase and the magnetic dipolarization. When the particles are measured close to the injection site, all energies will arrive at the approximately the same time. However, this does not always happen, so if the measurement is taken away from the injection site there will be dispersion in the energies meaning that higher energy particles arrive first, while less energetic, or slower moving, particles arrive later.

During the International Geophysical year (IGY) in 1957 many all sky cameras were place in the auroral regions of the northern hemisphere. From the images collected by these cameras, *Akasofu* [1964] was able to put together the morphology of the auroral substorm. Figure 1.13 shows a schematic presentation of the stages of an auroral substorm [*Akasofu*, 1964]. The substorm starts from quiet time (panel A) where there are multiple arcs drifting equatorially. The onset of the substorm starts as a brightening on the most equatorward arc near the midnight sector (panel b). The brightening then expands rapidly westward and poleward (panel C). A short time after this the bright bulge expands covering a larger part of the nighttime sector. The aurora within this bulge is very dynamic, with arcs appearing and disappearing and patches forming and pulsating. This time of active aurora is called

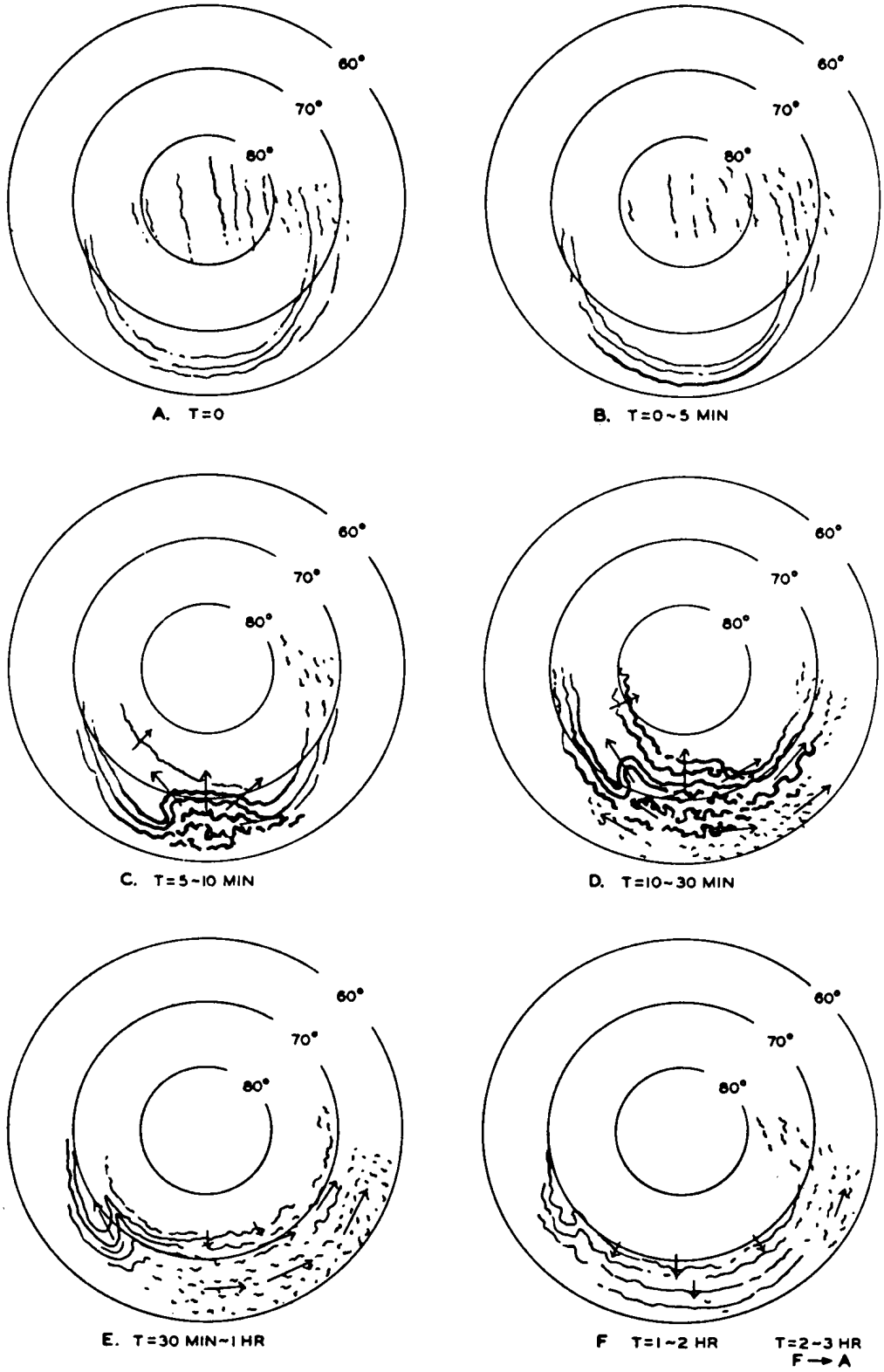

Figure 1.13: Phases of a substorm seen in the aurora [*Akasofu*, 1964].

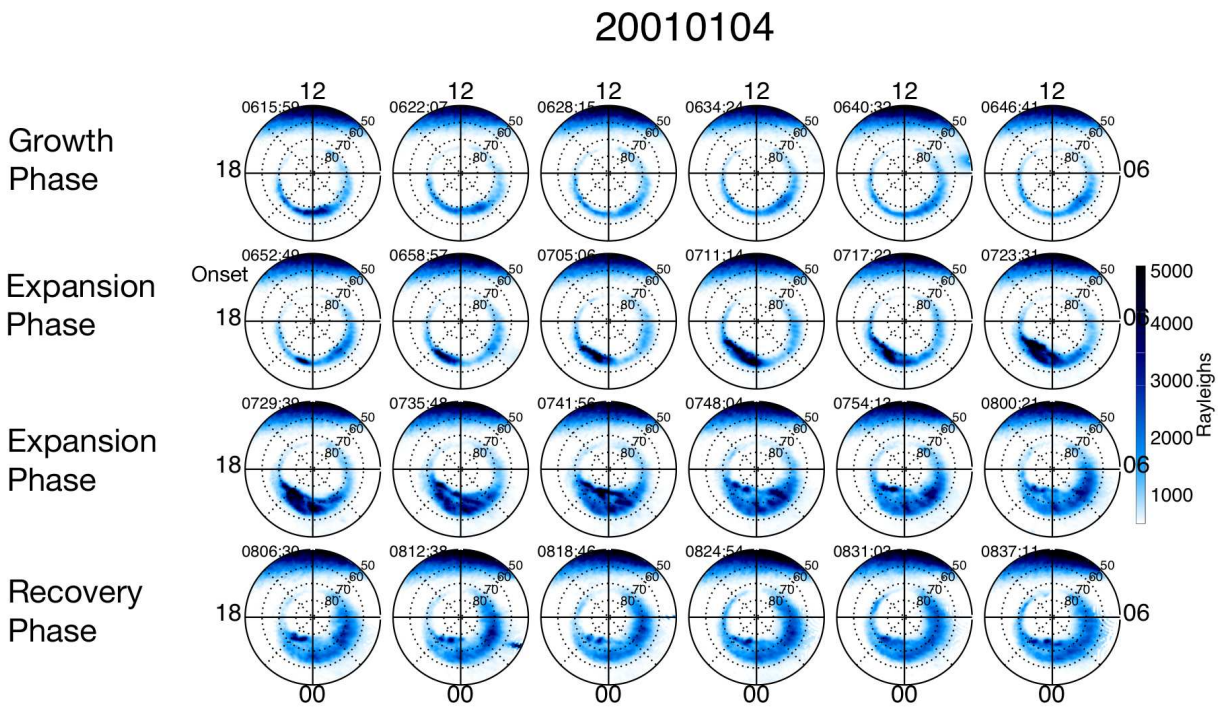

Figure 1.14: Phases of a substorm seen in the aurora. The first line is the growth phase, the second and third are the expansion phase and last line is the recovery phase. Onset of the expansion phase is at 652 UT. Images are from IMAGE FUV WIC.

the substorm expansion phase. A westward-traveling surge will usually form as the auroral bulge develops a sharp kink at its westward edge that will join with the bright arc extending westward (panels C and D). On the eastern edge, omega bands form and extend poleward (panel D). Eventually, the aurora activity ceases to expand poleward and the aurora begins to dim (panel E), thus, ending the expansion phase and starting the recovery phase. Finally the aurora returns to its quiet state as seen in panel F.

Similar to Figure 1.13, Figure 1.14 also shows the phases of a substorm as observed in auroral ultraviolet emissions, although the small auroral features (arcs and omega bands) cannot be seen due to the resolution of the images. (All auroral figures in this

paper will appear in the same manner, apex magnetic coordinates with noon on the top, midnight on the bottom, dusk to the left, and dawn to the right. The center of the figure is the magnetic north pole, while the outer ring is 50° magnetic latitude. During the growth phase, the aurora on the night side moves equatorward, which can be seen in the top row of Figure 1.14. This happens due to a larger reconnection rate on the dayside than the nightside. The onset of the expansion phase is seen as a brightening in the aurora at around 23 magnetic local time (MLT) and 0652 universal time (UT). The first image on the second line of Figure 1.14. The auroral bulge then moves both along the existing aurora and also poleward. This is usually referred to as poleward expansion. During the recovery phase, the last line of images in Figure 1.14, the aurora starts to weaken and the poleward boundary slowly returns to its original position, completing the substorm.

In conclusion, in order to classify an event as a substorm, at least 4 of the following should be seen in the data, if that data is available during the time frame of interest:

1. An increase in AE (drop in AL) of at least 25 nT in 1 minute [*O'Brien et al.*, 2002]

2. Mid-latitude positive bay in ground based magnetometers.

3. Energetic particle injection near midnight in geosynchronous satellite data.

4. Dipolarization of the magnetic field at geosynchronous orbit.

5. Auroral Brightening near midnight with a subsequent poleward expansion.

6. Pi2 pulsations in magnetometer data.

If 4 substorm identifiers are not seen, it does not mean necessarily that the event is not a substorm; it's just that there is not enough data to state that it definitely is

a substorm. This can cause confusion between researchers, since each person has a data set they prefer to use in order measure and study substorms. Thus, if someone says they see a substorm in their data, say AE, but someone else does not see it in their data, say Pi2, they will not agree on whether or not the event is a substorm. For this reason we look for at least 4 identifiers in our studies. We only require four of the six data points, because there are times when data is missing or satellites are in the wrong location to measure the substorm. So, if substorm onset signatures are measured in at least 4 of the 6 data sets we can be confident it is not pseudo-breakup or an anomaly in the data.

1.3.2 Steady Magnetospheric Convection

If the IMF B_z stays negative for an extended period of time, the substorm process should be periodic. As one recovery phase finishes, a new growth phase should begin. However, this does not always occur. Sometimes, if the IMF B_z is negative and steady for an extend period of time, then the reconnection rate on the nightside will eventually balance the dayside reconnection rate and enhanced steady magnetospheric convection (SMC) will ensue. When convection is steady, there is an enhancement of geomagnetic activity without substorm signatures [*Pytte et al.*, 1978; *Sergeev*, 1977], *i.e.* no poleward movement of the aurora, AL and AE should be fairly steady and no particle injections at geosynchronous orbit. The difference between an SMC and quiet times is that SMCs are driven active events in the magnetosphere. During SMCs, energy is entering the magnetosphere that is then deposited into the ionosphere with little storage in the magnetotail lobes.

In the past, SMCs have been defined as a lack of substorm signatures [*Sergeev et al.*, 1996]. However, this is not enough to truly define steady convection. First, by

this definition, an SMC must begin and end with a substorm; however, this is not necessarily the case. Second, it defines one type of event by the lack of another type of event. Since scientists cannot always agree when there is a substorm in the data, there can be controversy about when there is not a substorm. One way to solve this dilemma is to define SMCs by the balance of reconnection rates. If the reconnection rates on the dayside and nightside are balanced, then the area inside the polar cap (discussed in section 1.1.3) should remain steady for that period of time. Polar cap area (A_{pc}) can easily be measured using auroral images from space. This technique will be discussed further in Chapter 2. Thus, these events will not only be referred to as SMCs but also as Balance Reconnection Intervals (BRIs) which is a more accurate term. One reason for the new terminology is the word "steady" implies that the entire magnetosphere is steady. This is not always so. Steady convection on a large scale does not require the magnetosphere to be perfectly steady on a small scale. In many of our BRI/SMC events, there are small scale perturbations in the data. One example is a pseudo-breakup, where a brightening in the aurora appears to be the onset of a substorm but fades within minutes and no substorm expansion develops.

1.3.3 Sawtooth Oscillations

Magnetospheric sawtooth events were first identified in the Los Alamos National Lab (LANL) geosynchronous particle data by *Belian et al.* [1995]. They are defined as large amplitude, quasiperiodic oscillations of the energetic particle fluxes. Sawtooth oscillations acquired the name from saw blade formation seen in the plotted data of the Synchronous Orbit Particle Analyzer (SOPA) proton fluxes between 50 keV and 400 keV. The rapid flux increases and gradual decreases are associated with

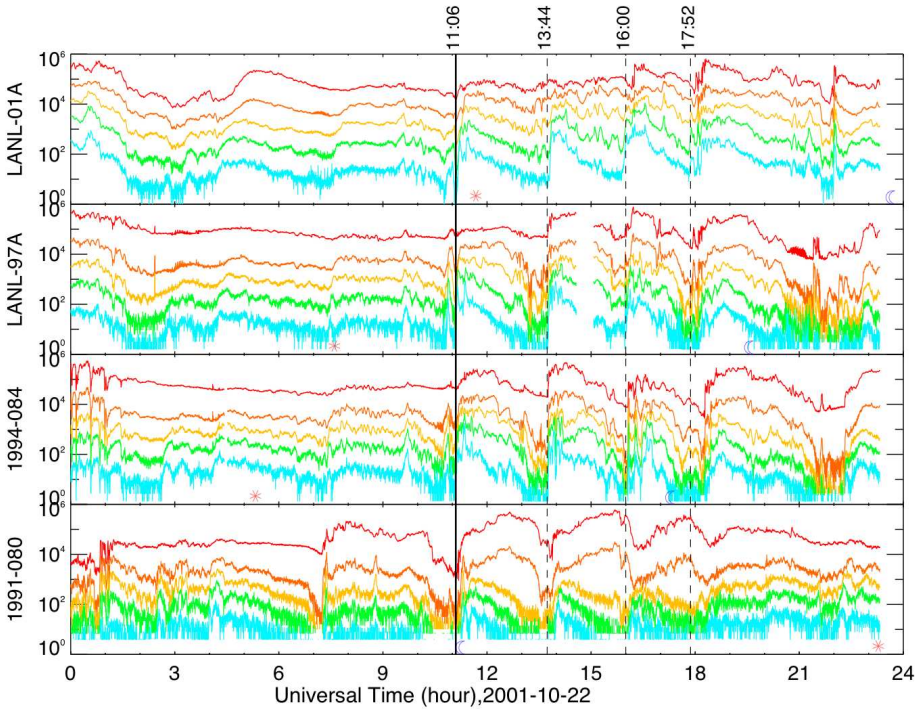

Figure 1.15: Los Alamos National Lab satellite flux data for proton particle injection for the Sawtooth oscillation on Oct. 22 2001.The energies shown from red to blue are as follows: 75 – 113 keV, 113 – 170 keV, 170 –250 keV, and 250 – 400 keV. The red star indicates when the satellite is at local noon while the blue moon is local midnight.

dipolarization and stretching of the magnetic fields at geosynchronous orbit [*Henderson et al.*, 2006a]. In order to identify an event as a sawtooth oscillation first there must be at least one LANL satellite near local noon (±3 MLT) and one simultaneously near local midnight (± 3 MLT). The particle injections must also be observed quasi-globally [*Cai et al.*, 2006a, b].

Figure 1.15 is a plot of the LANL SOPA proton flux from 4 different satellites for the sawtooth event on October 22, 2001. The vertical lines represent the onset times for each individual sawtooth injection. One of the main differences between sawtooth events and periodic substorms is that individual sawtooth injections occur over a larger local time range then substorms [*Reeves et al.*, 2002]. For example, most of the

injections in Figure 1.15 were measured by all 4 satellites. Substorm injections will typically only be measured by satellites close to local midnight. Another difference between substorms and sawtooth injections is that the sawtooth injections show little to no dispersion in the energy channels. This is due to an injection that occurs over much a larger area in local time [*Henderson*, 2004]. There is still debate as to whether sawtooth injections are large substorms or a different phenonmon [*Henderson*, 2004; *Henderson et al.*, 2006b; *Cai et al.*, 2006a, b]. While sawtooth injections will be discussed in this thesis, this question will not be addressed.

While sawtooth injections appear like large substorm in the data, the solar wind/IMF drivers are much like those for SMCs. Sawtooth oscillations appear to be driven by steady, strong IMF B_z ($\sim$ - 10 nT) [*Henderson*, 2004; *Henderson et al.*, 2006a], while SMCs are driven by steady moderate IMF B_z ($\sim$ - 4 nT). These solar wind/ IMF drivers will be studied in more detail in Chapter 5.

1.3.4 Magnetospheric Storms

When the IMF B_z is negative and strong (<-5 nT) [*Burton et al.*, 1975] for an extended period of time, a geomagnetic storm should occur. A magnetic storm is defined by an enhancement of the ring current. The strength of a magnetic storm is measured by the D_{st} (Disturbance storm time) index. D_{st} is the disturbance of the north/south component of the surface magnetic field at low latitudes and is a measure of the symmetric component of the ring current. In order for an event to be considered a geomagnetic storm, D_{st} should be less than -50 nT [*Joselyn and Tsurutani*, 1990].

Many storms start with a sudden impulse or storm sudden commencement (SSC), which is a consequence of an increase in the solar wind dynamic pressure. The

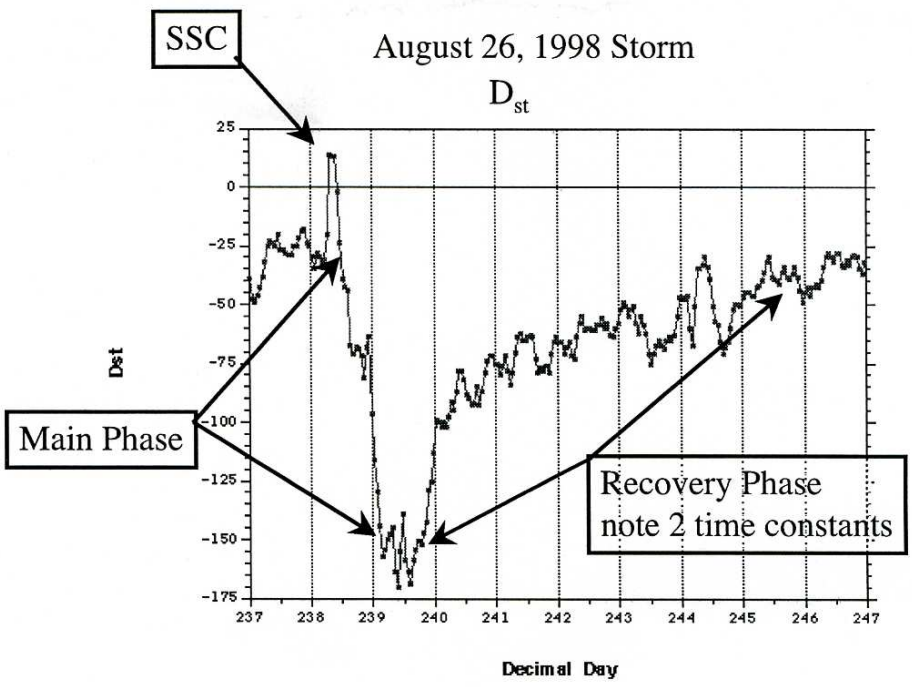

Figure 1.16: D_{st} for storm on August 26, 1998.

increase causes an enhancement in the magnetopause current, which is measured by a positive perturbation in the magnetic field at low latitudes. When the magnetosphere is quiet, particles are drifting around the Earth in a gradient-curvature drift which is balanced by the $\mathbf{E} \times \mathbf{B}$ in the plasma sheet. When IMF B_z is negative there in an enhancement of the IMF electric field, this electric field is then imposed on the magnetotail through convection (see section 1.2.3). This enhanced convection electric field allows plasma sheet particles to penetrate closer to Earth. The plasma sheet protons drift westward while the electrons drift eastward, thus setting up the ring current. When there are more particles entering the inner magnetosphere than leaving D_{st} drops. This is the main phase of the storm. When the number of particles being injected lessen or the $\mathbf{E}$ decreases then the number of particle leaving is greater then the number entering and D_{st} will start to rise, thus beginning the recovery phase.

Figure 1.16 shows the D_{st} for the storm on August 26, 1998. Note the length of time for each phase, lasting almost a day for the main phase and up to seven days for the recovery phase.

Storms are not a completely independent mode of the magnetosphere. Substorms, SMCs (BRI) and sawtooth oscillations can all occur during storm time.

1.4 Scientific Motivation

As described above, all three different modes of convection differ in their magnetospheric signatures and solar wind/IMF drives. Sawtooth injections in many ways resemble large isolated substorms. *Cai et al.* [2006a, b] compared statistically the differences between sawtooth injections and isolated substorms in terms of the ionospheric potential patterns and magnetic dipolarization. They found the sawtooth injections to be larger and more global than the isolated substorms as did *Henderson et al.* [2006a, b]; *Clauer et al.* [2006]. They also found that the first tooth in a series can differ from the other teeth, in that they tend to be more substorm like. Thus, many believe global sawtooth oscillations to be large periodic substorms [*Huang et al.*, 2003, 2005].

There are also many ways both isolated substorm and sawtooth oscillations can be similar to BRIs. While sawtooth oscillations tend to occur when the IMF B_z is steady at approximately -8 nT, BRIs occur when it is steady at around -3 nT [*O'Brien et al.*, 2002; *McPherron et al.*, 2008]. Also double ovals in the aurora have been seen during both BRIs and sawtooth oscillations [*Henderson et al.*, 2006a].

Due to these differences and similarities, it is important to include all three event types in the same investigation. Thus, the large question to be addressed in this dissertation is: "Under what conditions, internal and external, does the magnetosphere

enter into different convection modes?" In order to answer this question first three smaller questions will be investigated. Each chapter in this dissertation is devoted to one of the questions below.

1. How diverse are BRIs and how do the reconnection rates begin to balance and become unbalanced?

2. What are the similarities and differences of the F_{pc} and therefore the convection during different convection modes?

3. How important are the steadiness and the magnitude of the solar wind/IMF drivers in determining which convection mode the magnetosphere will enter and what are the implications of the these drivers on the balance or imbalance of reconnection rates?

The first question will be addressed in Chapter 3 in which four BRIs are studied. Each event has a unique attribute allowing for a comparison of the diversity during this convection mode. Also it has been stated that all BRIs/SMCs begin and end with substorms [*Sergeev et al.*, 1996]. Our case studies do not support this idea, we have found that BRI can begin with a slow build up activity in the magnetosphere and end with a slow return to quiet levels. Thus, Chapter 3 investigates different ways convection can become balanced and unbalanced.

Question 2 is investigated in Chapter 4 where the auroral images and F_{pc} for each convection mode are compared. This is the first time a case study for each type of event has appeared in the same study. By comparing the different types of events, we hope to discover similarities and differences in the reconnection rates, convection, and auroral signatures.

From recent studies, [Borovsky, 2004] it has been found that the solar wind drivers for SMCs are very similar to those for sawtooth events. It appears that with weak to moderate driving in the IMF B_z the magnetosphere will enter a substorm mode. If IMF B_z remains weak to moderate and is steady, then a BRI will ensue. If the IMF B_z driver is strong and steady, then global sawtooth oscillations will occur. While holds for the IMF B_z driver, it remains to be seen if this is true for other solar wind and IMF drivers. Thus, Chapter 5 will investigate both the magnitude and the steadiness of the solar wind and IMF drivers, therefor addressing the last question. Along with the drivers, some ionospheric and magnetospheric indicies are included (D_{st}, CPCP, and AL) so that the intensity and steadiness of the ionosphere and magnetosphere can be compared.

CHAPTER II

Data and Methodology

2.1 Satellites and Data: Comparing UVI and FUV

2.1.1 Polar UVI

The Polar space craft was launched by NASA on February 24, 1996 with the purpose of studying the Sun-Earth connection and Earth's magnetosphere. The orbit of Polar is highly elliptical at 86 degrees inclination and it has a period of 17.5 hours. The large eccentricity of the orbit is ideal for auroral imaging, allowing Polar to spend most of its time high enough above the Earth to image the global aurora. The large eccentricity of the orbit also allows for approximately 8-10 hours of continuous imaging [*Torr et al.*, 1995]. It is the Ultraviolet Imager (UVI) instrument on Polar that takes these auroral images. The UVI instrument rotates between 5 filters and has a viewing field of 8 degrees in diameter. The two filters of interest for these studies are the Lyman Birge Hopfield N_2 (LBH) long and short short. Unless other wise stated, all images and Polar UVI data in this study are LBHl. LBH spectrum is formed by the following chemical equations:

$$N_2(X^1\Sigma_g^+) + e^* \longrightarrow N_2(a^1\Pi_g) + e \tag{2.1}$$

$$N_2(a^1\Pi_g) \longrightarrow N_2(X^1\Sigma_g^+) + h\nu_{LBH} \tag{2.2}$$

The LBHl measures 160-180 nm. In this range, there is little to no O_2 absorption. The LBHs filter measures 140-160 nm, which does include O_2 absorption. Because the LBH auroral emissions peak at approximately 120 km [*Meier et al.*, 1982] it is assumed that the images are of auroral emissions at 120 km.

When creating the auroral images, the raw image in counts must first be corrected. A flat-field correction is needed since each pixel may have a slightly different sensitivity. This is done by putting a 'flat-field' source through the detector and calibrating it so that each pixel reads the same intensity. Once this is done a table with each pixel correction is created so that it can be removed from the image. Other correction needed are due to the integration period and the rotation of the instrument on the satellite. There are also tables created for these calibrations during the testing phase. Once in space the instrument can be calibrated using stars of known FUV intensities.

Once all the calibrations have been done the image can be calibrated to units of photons/cm^2/s, Rayleighs or ergs/cm^2/s. Using the spin axis direction, and spacecraft position in geocentric inertial (GCI) coordinates the images are transformed to geographic coordinates. The size of the image, in pixels, is limited by the readout element of the detector, which in this case is a charge coupled device (CCD) with 488×550 photosensitive pixels. Due to the configuration of the instrument the edges of the CCD are not illuminated, once these edges are discarded an oval frame with 200×228 pixels remains *Torr et al.* [1995]. Thus, the geographic images are 200×228 pixels . Each pixel has an associated, solar zenith angle, space craft zenith angle, magnetic latitude, and magnetic local time (MLT) hour in degrees. With these parameters the image can then be converted to magnetic coordinates. In order to truly compare the magnetic images they must all have the same pixel resolution, despite

there geographic resolution (see below). In order to accomplish this each pixel that lies across the center of the image or vertically through the center of the image a resolution of 0.5 degrees magnetic latitude when converted. Since, a minimum magnetic latitude of 50° is used the image in MLT coordinates is 160×160 pixels. It is these images in magnetic coordinates that are used through out my investigations.

UVI uses an exposure time of 36 seconds and this along with the changing of the filters, produces images that range from 36 seconds to 6 minutes apart. The 8 degree diameter field of view allows of a resolution of approximately 40×35 km/pixel at apogee ($\sim$ 9 R_E) and 10×9 km/pixel at perigee ($\sim$ 1.8 R_E) [*Torr et al.*, 1995]. Thus, the entire auroral oval can usually been imaged when the spacecraft is at apogee, but as the distance from the Earth decreases less of the aurora can be imaged. So, only images that show the nightside aurora and have coverage that is more than 50% complete are used in these studies.

2.1.2 IMAGE FUV

The IMAGE (Imager for Magnetopasue-to-Aurora Global Exploration) satellite followed Polar by 4 years with its launch on March 25, 2000. By this time, Polar's orbit had been precessing with its apogee approaching the equator, thus creating less complete auroral images. IMAGE helped fill the gap in auroral imaging with its highly eccentric orbit that has an apogee of approximately 7 Re, an inclination of 90 degrees and an orbital period of 13.5 hours [*Mende et al.*, 2000]. One draw back of IMAGE is the shorter orbital period limits our contiguous images. Instead of 8-10 hours of images from Polar, IMAGE only produces about 6 hours.

In order to get comparable imaging to that of Polar UVI LBHl, IMAGE's Far Ultraviolet Imager (FUV) with the Wideband Imaging Camera (WIC) was used.

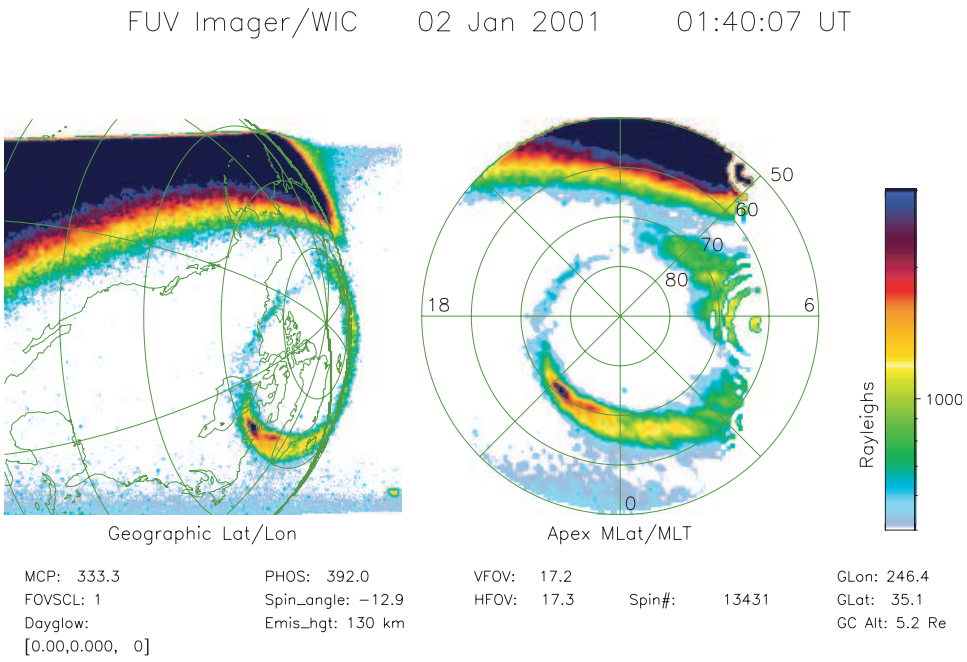

Figure 2.1: Images taken from IMAGE FUV WIC in Rayleighs. The image on the left is in geographic coordinates, while the one on the right is in magnetic coordinates.

IMAGE FUV WIC has a spectral range from 130-180 nm with a peak sensitivity at 150 nm. Once again the images must first be be corrected and converted to magnetic coordinates before use in these studies. Once again the number of pixels per image is dependent upon the detector, the images from FUV WIC have 256×256 pixels. The field of view is 17×17 degrees allowing for a resolution of 0.18° for each cell, one cell is approximately twice a pixel diameter. Therefore, at apogee the resolution is 120 km/cell and at perigee it is 3.1 km/cell [*Mende et al.*, 2000]. Similar to UVI, when converting from geographic to magnetic coordinates a 0.5 degree resolution is used. However, in the processing of the image it is smoothed to a 256×256 resolution. This smoothes out the pixels and allow the image to look more "realistic", however, it also causes a loss of some the finer structures in the aurora. It can also create a variation in the open-closed boundary we are measuring, but since this is done for

each image, it is of little effect when comparing boundaries created only by FUV. It will cause some minor differences when comparing those boundaries created by UVI to those crated by FUV.

The image on the left of Figure 2.1 is a FUV WIC image in geographic coordinates, the right side is the same image in magnetic coordinates. Because the aurora is on the edge of the geographic image there is distortion in the aurora and its boundary. Since the edge of the aurora is not the same distance to the space craft as other portions, when it projected into MLT coordinates it is difficult to know the exact magnetic coordinates of the pixels. hen this occur the image and the boundary are no longer reliable where is an edging effect. If the edging effect is to great then the image is not used for the event analysis. If the effect is small then boundary is interpolated in that region, the same as if the aurora was missing.

This an other distortions can also occur because the coordinate for each pixel are only precise for the bottom left corner of that pixel. So, an MLT image taken a perigee will be have less resolution per pixel than the original images, it will be compressed. An MLT image taken a apogee will have more resolution, and be smeared. This creates a loss in small scale structures when converting to coordinates. It can also cause a shift in the boundary we are measuring. However, since it is the open magnetic flux in the polar cap we are interested in the effects are minimal.

2.1.3 Comparison of Image sets

Figure 2.2 shows a plot of the instrument wavelength sensitivity for a 4 keV electron beam for both Polar UVI and IMAGE FUV WIC. Note that Polar UVI has two peaks (LBHl and LBHs), while the FUV WIC band width is much larger, covering both LBHl and LBHs. While the peaks are larger for UVI the larger bandwidth for

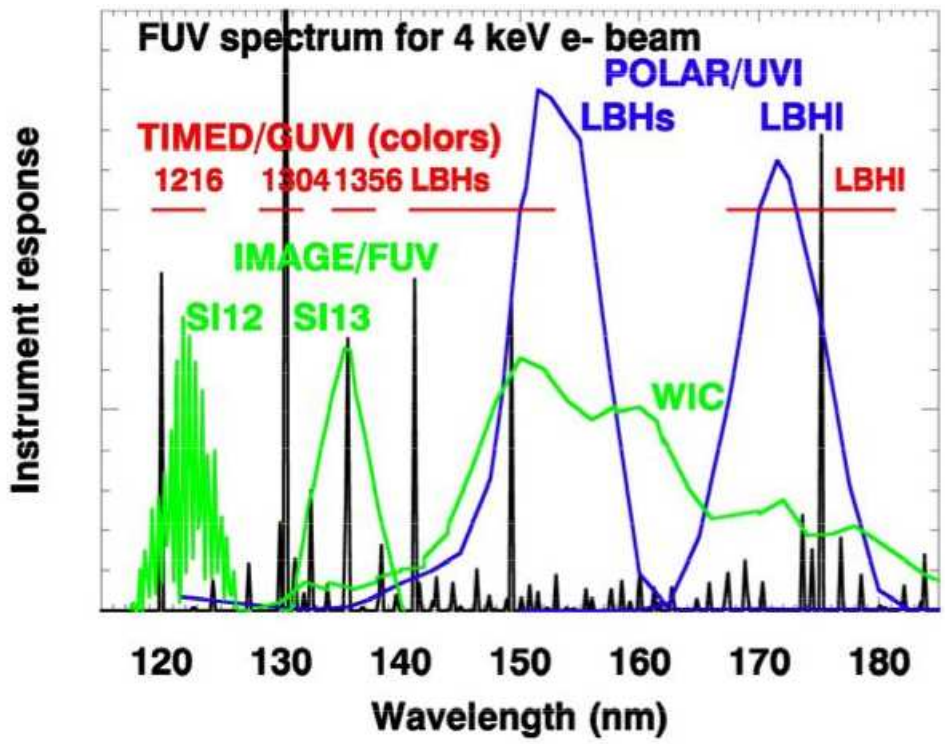

Figure 2.2: A plot of the the sensitivity of FUV WIC and UVI LBHl and LBHs for different wavelengths when a 4 keV electron beam put through the detector.

FUV causes the FUV WIC images to be much brighter than the UVI images. Figure 2.3 shows images taken by UVI and FUV instruments during the same event. Note that the UVI has larger pixels and a slightly smaller field of view. However, most of the auroral features can be seen in both sets of images. In general, the FUV images are about 3 times brighter than the UVI images.

Figure 2.4 illustrates how a keogram is created from auroral images for an isolated substorm on January 04, 2001. The upper images are in Apex magnetic coordinates, with the magnetic north pole in the middle of the image at 90 degrees latitude, noon at the top and midnight on the bottom. The keogram on the bottom is created by taking a slice of the aurora at a chosen Magnetic Local Time, or MLT (01 MLT in Figure 2.4) and then plotting it against universal time. The color shows the auroral

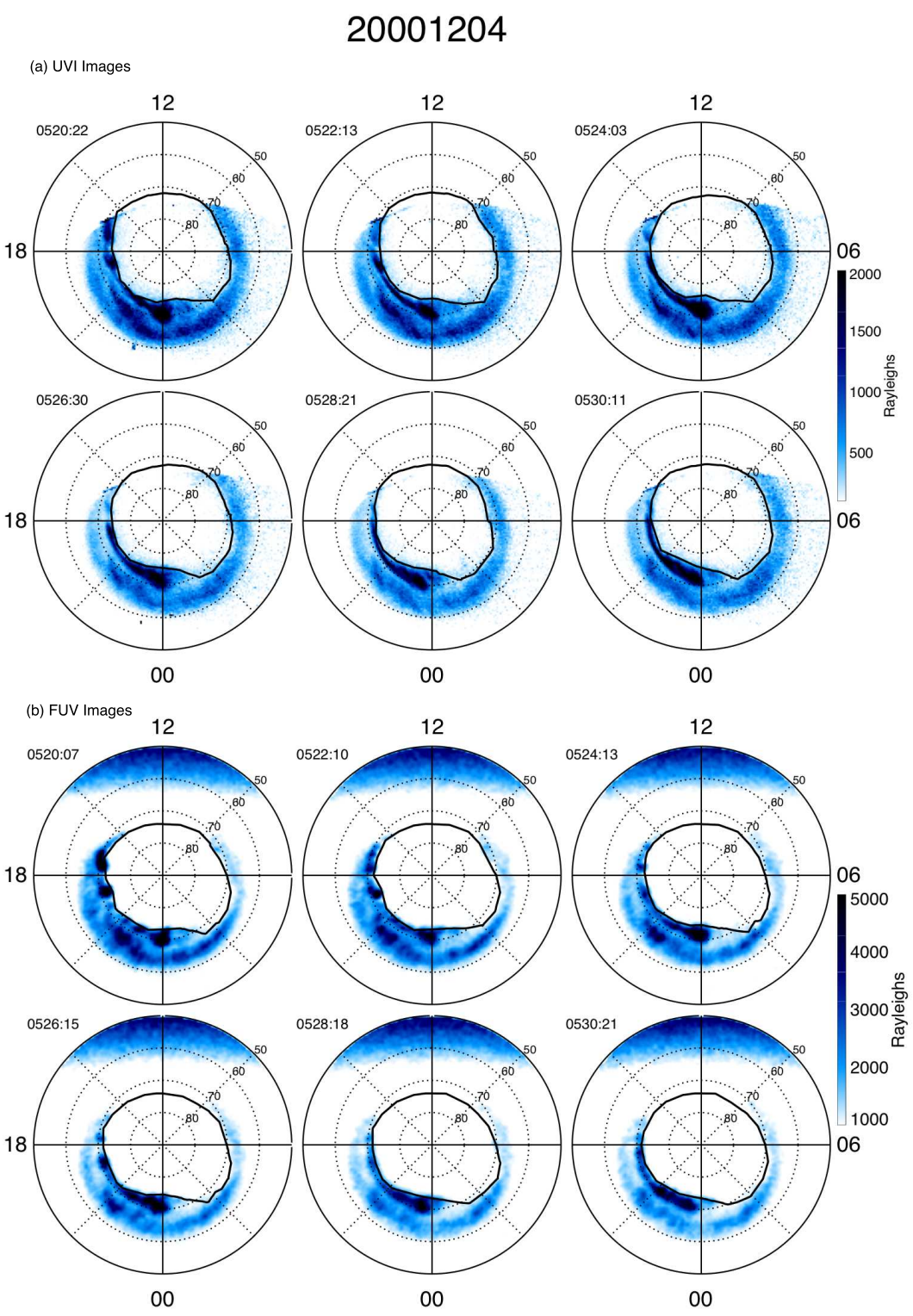

Figure 2.3: (a) plot of the aurora on December 04, 2000 taken by Polar UVI LBHl. (b) The same plots as (a) but taken with IMAGE FUV WIC. Also, note that the maximum intensity scale for the Polar UVI LBHl images is 2000 Rayleighs while FUV WIC instrument images have a maximum of 5000 Rayleighs.

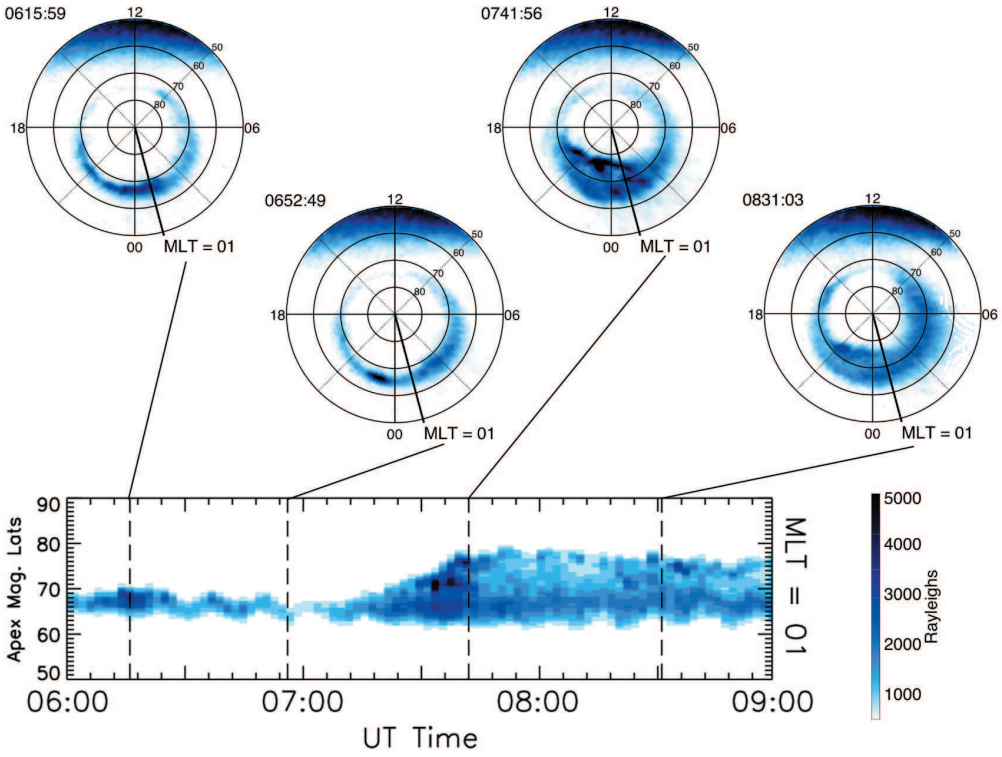

Figure 2.4: An example of how a keogram is made using data from the isolated substorm on January 04, 2001. Top shows images from IMAGE FUV WIC in apex magnetic latitude with noon at the top and midnight at the bottom. To make a keogram a slice is taken (01 MLT) and then plotted vs. universal time. The color show the intensity of the aurora in Rayleighs.

intensity in Rayleighs while the y-axis is Apex magnetic latitude. The keogram starts at 50 apex magnetic latitude at the bottom and goes to 90, or the magnetic north pole, at the top. This configuration allows us to see the poleward and equatorward movement of the aurora at a specific MLT. However, a keogram at only one MLT conveys a limited amount of information. For example, the auroral onset of the substorm can be seen in the auroral image taken at 06:52 UT at about 22 MLT, but since the keogram only shows 01 MLT it appears that the onset would be about 10 minutes later. For this reason, we show keograms for each event at intervals of 02 MLT, spanning from 18 to 06 MLT and going through midnight. This allows us to

see the movement of the aurora both in magnetic latitude and magnetic local time (MLT). Keograms of this type will be used in to study the auroral images in detail in Chapter 4.

2.2 Calculation of Open flux

As stated in section 1.1.3, the boundary between open and closed magnetic field lines in the magnetosphere maps approximately to the polarward edge of the aurora. This poleward boundary can be measured using Polar UVI LBHl and IMAGE FUV WIC data. *Baker et al.* [2000] compared the auroral boundary as measured by Polar UVI LBHl and DMSP. He found that a cutoff brightness of about 4.3 photons/cm^2/sr ($\sim$ 130 Rayleighs) compares well to the open-closed boundary determined using DMSP particle precipitation data. However, when the aurora is active, this intensity cutoff increases and thus must be accounted for in our methodology. Although this method of finding the open-closed boundary is not exact, it is close enough for these studies since it is the temporal changes in this boundary we are interested in. For example, if the image boundary shifts or changes then the "true" open-closed boundary should change by the same amount.

At this time, no one has conducted a study similar to *Baker et al.* [2000] for IMAGE FUV WIC. So, in order to find the proper intensity (brightness) cutoff, we compared Polar UVI LBHl to IMAGE FUV WIC. First, we found periods where both Polar UVI LBHl and IMAGE FUV WIC were collecting data. We used northern winter images during active times. This insured that dayglow would not have to be removed, as it may affect intensity levels of the aurora. After a series of comparisons, it was concluded that the appropriate cutoff for IMAGE FUV WIC is $\sim$ 900 Rayleighs. Figure 2.3 shows the images for approximately the same times for both

Polar UVI LBHl and IMAGE FUV WIC, with the boundary over plotted. In general, the FUV images are about 3 times brighter than the the UVI images. However, this does not affect the boundaries. Figure 2.3 shows that the boundaries created with FUV and UVI images are very similar, thus both types of data can be used in the same study. Figure 2.5 (a) is a plot of the area inside the boundaries, or the polar cap area (A_{PC}), for the images in Figure 2.3. The red line is the A_{PC} from the FUV images, while the blue line is from the UVI images. While the two lines are not exactly the same, it can seen that they both follow the same trends. The bottom plot in Figure 2.5 is a plot of the difference between the two lines above (A_{FUV} – A_{UVI}) the maximum difference between the two lines is 1.2×10^6 km^2. This is about 10% of the total value of the area at this time, which may seem large, but since it is the trends and changes in the A_{PC} that are of interest in these studies, the A_{PC} from both types of images are similar enough to use here.

Once the boundaries are found for all the available images for an event, then the area inside the boundary is calculated. This area is the polar cap area or A_{pc}. In order to calculate the total amount of open magnetic flux in the polar cap (F_{pc}), the magnetic field inside the polar cap is integrated over the area inside the polar cap. The International Geomagnetic Reference Field (IGRF) is used to calculate the magnetic field. Changes in the F_{pc} indicate changes in the convection and reconnection rates in the magnetosphere. For example, if the reconnection rates on the dayside are higher than on the nightside, as in the growth phase of a substorm, then the F_{pc} will increase, as seen in Figure 2.6. When the near Earth neutral line (NENL) is formed and nightside reconnection increases to becomes greater than the dayside merging rate, as in the expansion phase of a substorm, the F_{pc} will decrease. If the dayside and nightside reconnection rates are balanced, as in an SMC, than the F_{pc}

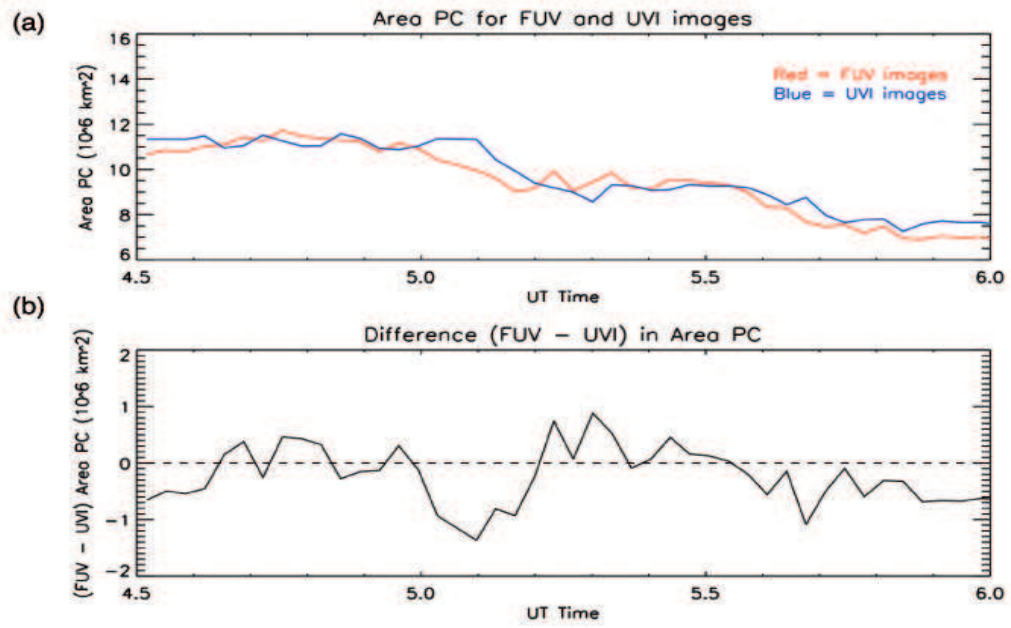

Figure 2.5: (a) Plot of the polar cap area created from UVI (red) and FUV (blue) images. (b) A plot of the difference between the polar cap areas calculated from UVI and FUV ($A_{FUV} - A_{UVI}$)

will remain constant. Thus, it is the changes in the boundary and in the F_{pc} that we are truly interested in.

Figure 2.6 is a plot of the F_{pc} for the substorm on January 4, 2001 and was created from the auroral images in Figure 1.9. Note that, as the night side boundary moves equator ward on the first line of Figure 2.6, the F_{pc} shows a slight increase. At the onset of the expansion phase, the aurora starts to move poleward, decreasing the amount of open flux in the polar cap. During the recovery phase of this substorm, the aurora does not move. Instead it just fades, so there is no change in the F_{pc}, as seen in Figure 2.6.

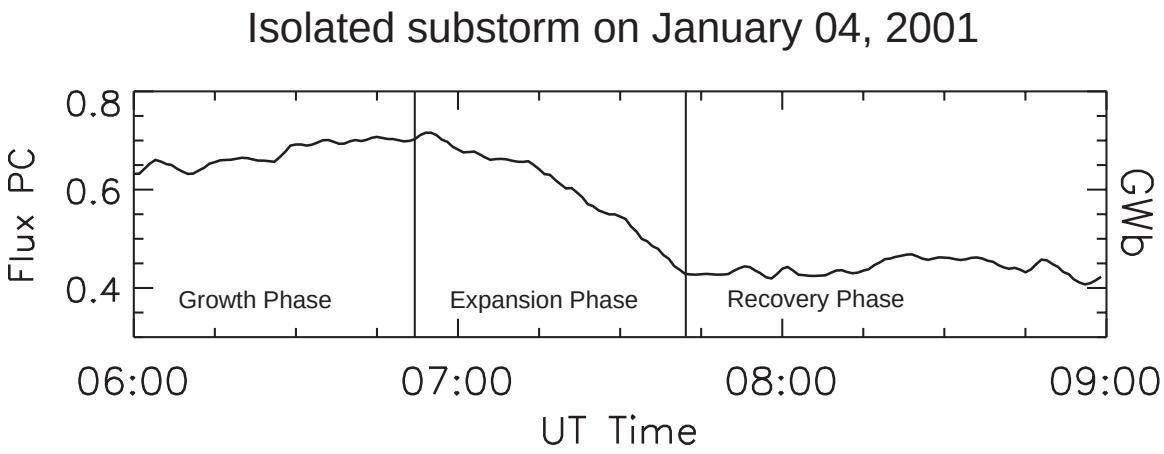

Figure 2.6: The F_{pc} for the substorm on January 04, 2001.

2.3 Dayglow and it's removal

Dayglow is the term used to describe the ultraviolet emissions from Earth's upper atmosphere caused by solar energetic electrons *Chamberlain* [1961]. Since we are studying the magnetic pole of the northern hemisphere, dayglow is of little concern during the winter months (December, January and February). However, during the rest of the year it can interfere with the dayside and sometimes the entire auroral image. Since we need to find the poleward auroral boundary in order to calculate the amount of open magnetic flux, it is important that we remove dayglow during the spring, summer, and fall months. Dayglow is removed from images only when it interferes with the ability to determine the auroral boundary.

Our dayglow removal process is based on the methodology set forth in *Immel et al.* [2000] Although he used Dynamics Explorer 1 (DE-1) FUV data, we found his formulation useful for both Polar UVI LBHl and IMAGE FUV WIC data. The equations from *Immel et al.* [2000] are as follows:

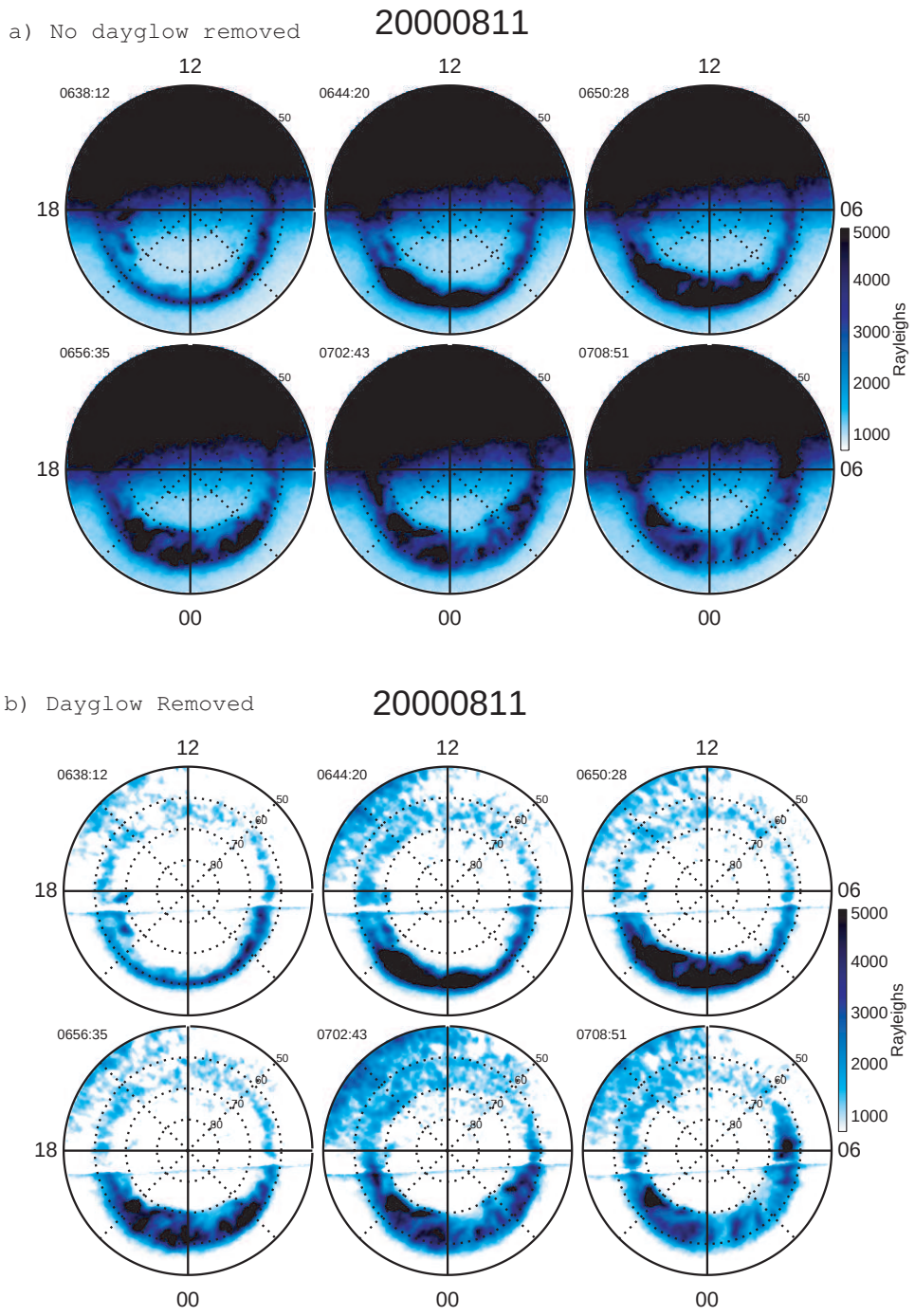

Figure 2.7: (a) plot of the aurora on August 11, 2000 with out dayglow removed. (b) The same plots as (a) with dayglow removed

$$B = e^{x_2 + D * x_3} \tag{2.3}$$

$$x = 0.75 - D * 0.003 \tag{2.4}$$

$$Brightness = B * cos(S)^x + x_1 \tag{2.5}$$

where D is the space craft zenith angle in degrees and S is the solar zenith angle in radians. The coefficients x_1, x_2, and x_3 are unknown and must be determined on an orbit by orbit basis, using the following methodology:

1. The average auroral zone (60 - 80 magnetic latitude) is removed from each image of an orbit, leaving only dayglow.

2. The pixels for all the images are binned by solar zenith angle (S) and space craft zenith angle (D).

3. Random numbers are chosen for our coefficients, x_1, x_2, and x_3, and the brightness is calculated.

4. The random numbers are narrowed down until the averaged squared difference between the pixel by pixel brightness of the true image and calculated brightness is reduced below a chosen threshold.

5. The coefficients for each S and D bin are saved.

A second code then opens the saved file with the coefficients and calculates brightness for each pixel, including the aurora zone, of an image. It then removes the dayglow (brightness) value from the measured pixel value according to its S and D. Figure 2.7 shows images both without (a) and with (b) dayglow removed. Dayglow removal is not an exact process as there are times when too much or too little dayglow may be removed. For example, in many of the images there is a line across

the terminator where it is difficult to remove the correct amount of dayglow. The problem can also occur in empirical models where the dayglow is averaged by day of year, solar zenith angle and space zenith angle and then removed [Germany, personal communication]. Thus, it is not something that can be corrected for easily.

2.4 Other Data sets used

The indices used in this thesis (AE,AL, CPCP, and D_{st}) are derived by assimilative mapping of ionospheric electrodynamics (AMIE), which has been applied to approximately 150 ground based high latitude magnetometer records [*Ridley and Kihn*, 2004; *Cai et al.*, 2006a]. The interplanetary magnetic field (IMF) and solar wind parameters have been propagated to Earth using the *Weimer et al.* [2002]; *Weimer et al.* [2003]; *Weimer* [2004] psuedo-minimum variance technique. The propagation is accurate to approximately 6 minutes, thus onsets and triggers may not occur at the exact same time.

CHAPTER III

Balanced Reconnection Intervals: Four case studies

The first question listed in section 1.2,"How diverse are BRIs and how do the reconnection rates begin to balance and become unbalanced?" will be addressed in this chapter. Thus, this chapter examines 4 BRIs (SMCs) that exhibit very distinct features from one another. While each event is classified as a BRI according to our definition, they all differ in the magnetospheric physics producing them. These events represent some of the diversity that can occur during this class of phenomenon. The first event is very steady and represents the expected observations during an SMC. The second BRI has no substorm to conclude it, because the reconnection rates stay balanced until the IMF B_z turns completely northward. The third case study has no substorm to initiate the BRI, because the reconnection rates balance without an unloading process first. While the final event begins and ends with substorms, it differs from the others because it occurs during a higher level of magnetospheric activity.

3.1 Events

3.1.1 Event 1: Classic BRI (SMC) (February 3 & 4, 1998)

Figure 3.1 is a stack plot of data for the BRI that begins at 16:30 UT on the 3^{rd} of February and ends at 01:00 UT on the 4^{th}. The top panel is a MLT- UT plot of the maximum brightness from Polar UVI LBHl images. The center of the plot is midnight while the top and bottom are noon. Thus, any auroral brightenings associated with substorms should take place toward the center of the plot. One such brightening is associated with the substorm that occurs at 15:00 UT on the 3^{rd}. The second panel is the amount of open magnetic flux in the polar cap (F_{pc}) in GigaWebers (GWb). The next four panels are CPCP (kV), AE (nT), AL (nT), and D^*_{st} (nT), all calculated from AMIE [*Ridley and Kihn*, 2004]. The Weimer propagated IMF B_z is plotted on the bottom panel.

Although this event has previously been studied by *Goodrich et al.* [2007], it remains a key component of this investigation because it represents a "classic" BRI. This event is described as "classic" since it fits the definition of an SMC set forth by *Sergeev and Lennartsson* [1988]; *Sergeev et al.* [1996]. The IMF B_z is steady at approximately - 6 nT. AE, AL and D_{st} all exhibit very little variation. The F_{pc} remains steady at 0.51±0.04 GWb and the aurora is enhanced with very few brightenings and little movement. There are also substorms before and after the BRI, following the more classic definition of an SMC. The first substorm onsets at 15:00 UT and recovers before the BRI starts. Because the F_{pc} remains steady until the concluding substorm, it is difficult to separate the growth phase of the substorm from the BRI. Since there is no measurable loading of the tail, the BRI ends with the onset of the expansion phase of the substorm. However, it appears that this substorm was triggered by the IMF B_z turning northward at 01:00 UT. Thus, termination of

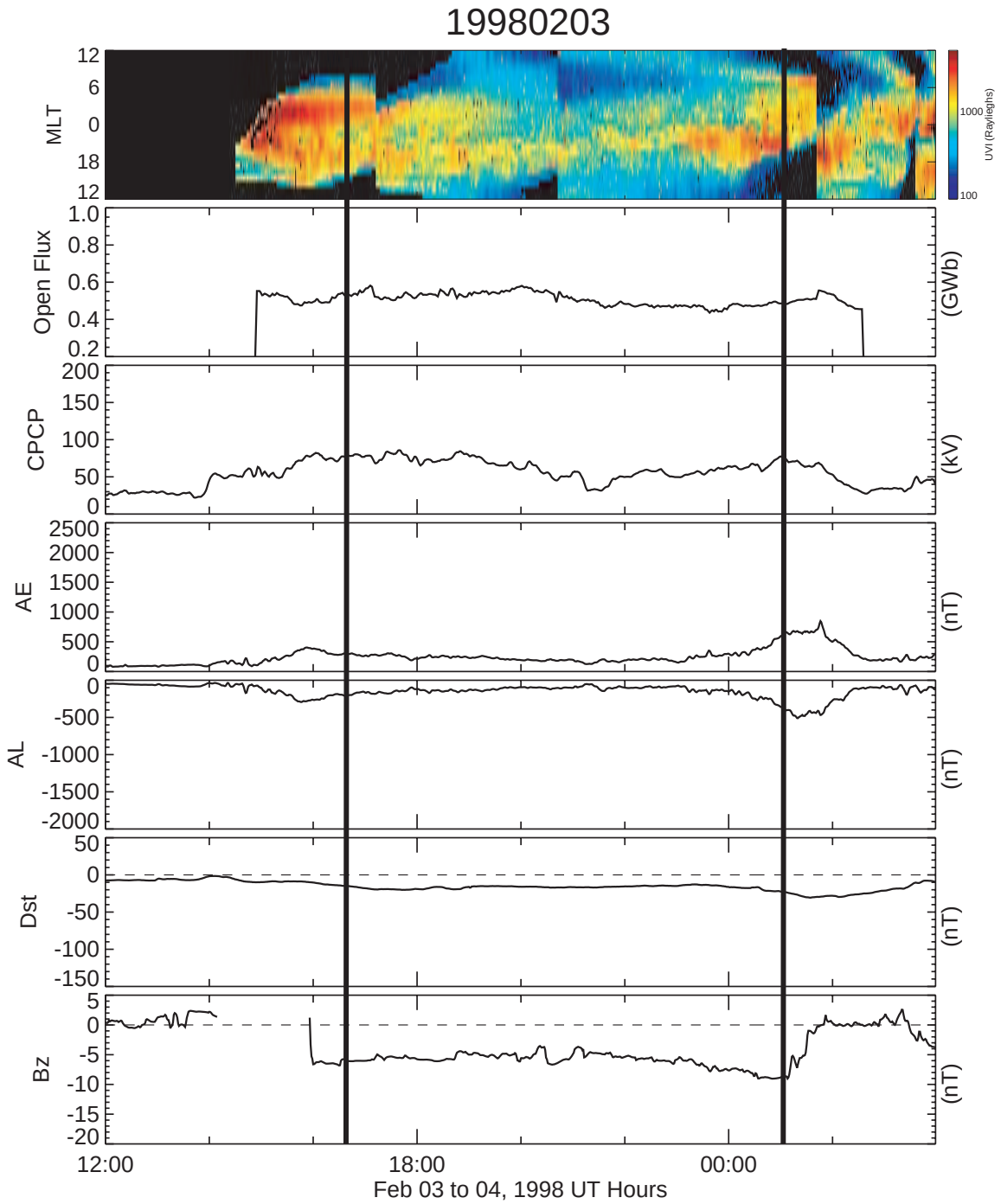

Figure 3.1: A stack plot of data for the BRI on Feb. 03, 1998 (Event 1). MLT-UT plot of the maxium brightness of the aurora (Rayleighs). Polar cap open magnetic flux (GWb). Cross polar cap potential as determined by AMIE (kV) AE as determined by AMIE (nT). AL as determined by AMIE (nT). D_{st} as determined by AMIE and the Hourly D_{st} (nT) over plotted in a dotted line. IMF B_z propagated using the Weimer method (nT). The vertical lines represent the beginning and ending of the BRI. The numbers on the sides are the averages in the data for the BRI time frame only.

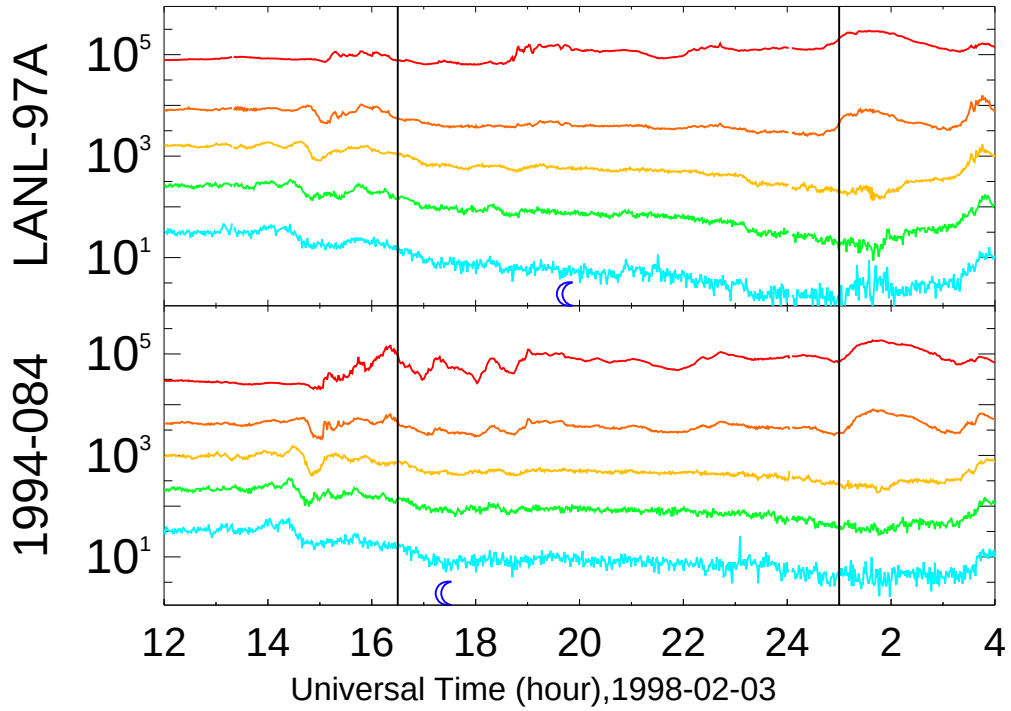

Figure 3.2: LANL SOPA Proton data for Event 1. Each color is a different energy channel with red as the lowest energy and blue as the highest. The blue moon represents when the satellite is at local midnight. Once again the vertical lines represent the beginning and the ending of the BRI.

the dayside reconnection causes the tail to unload via a substorm.

The two panels on Figure 3.2 are plots of Los Alamos National Lab (LANL) synchronous orbit particle analyzer (SOPA) proton data from two different satellites (1995-084 and LANL-97A). There are five different energy channels plotted with red as the least energetic and blue as the most. The moon on the plots indicates when the satellite is at local midnight. There are no particle injections that would indicate a substorms during this event [*Walker et al.*, 1976; *Erickson et al.*, 1979]. A small particle injection occurs at 01:00 UT on the 4^{th} that is associated with the expansion phase onset of the concluding substorm.

The solar wind/IMF data from the WIND satellite is displayed in Figure 3.3, propagated to Earth using *Weimer* [2004]. The IMF B_z during this BRI (SMC) is

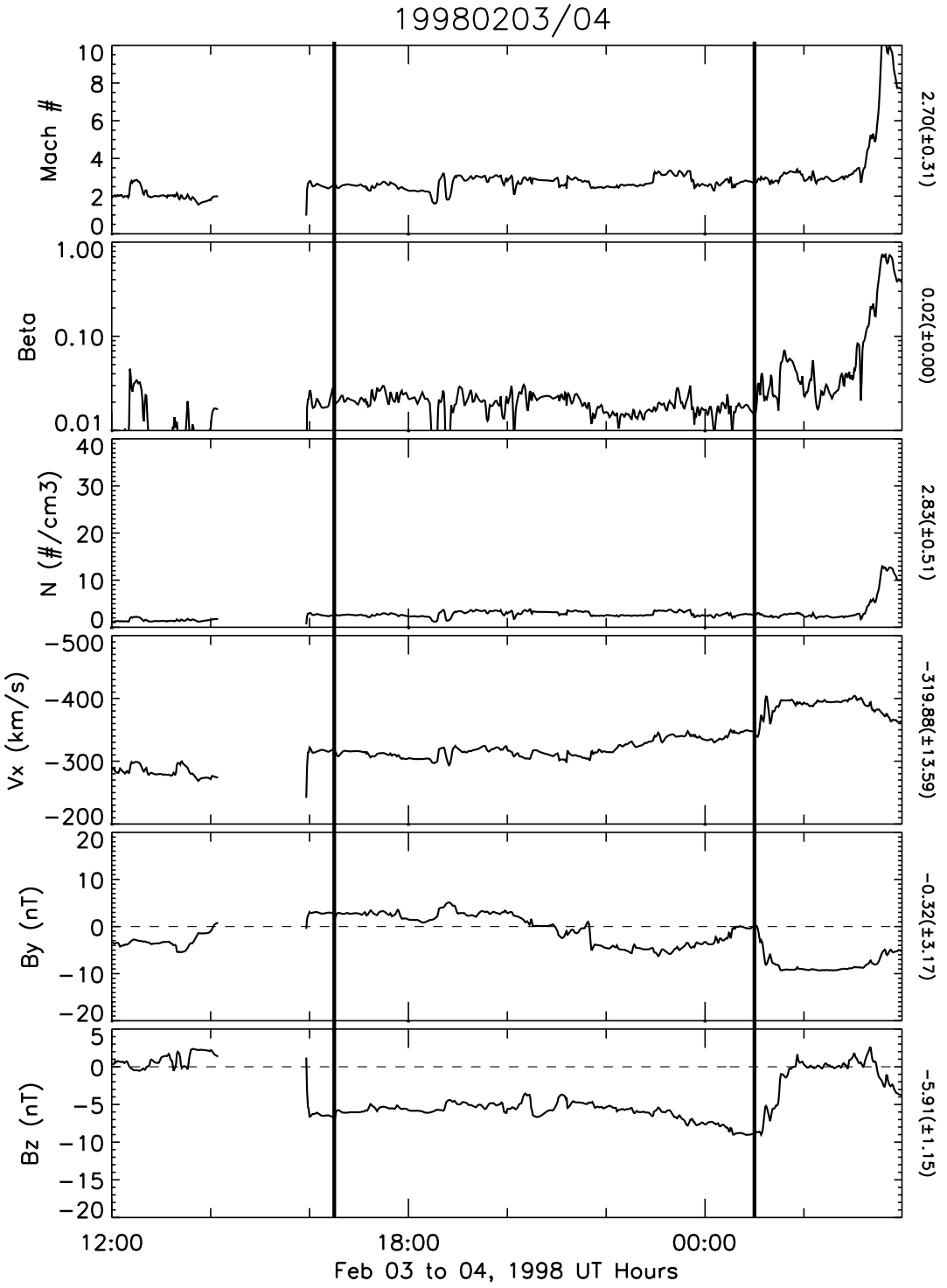

Figure 3.3: A stack plot of solar wind / IMF parameters from the WIND satellite propagated to the magnetopause using the Weimer method for Event 1. Solar wind Alfven Mach Number. Solar wind plasma Beta. Solar wind Dynamic Pressure (nPa). Solar wind Vx (km/s) IMF By (nT) IMF B_z (nT). Once again, the vertical lines represent the beginning and ending of the BRI. The numbers on the side are the averages and standard deviations for the BRI time frame only.

similar to that of other SMCs as measured by *O'Brien et al.* [2002] and *Tanskanen et al.* [2005]: negative, steady, and of moderate magnitude (- 5.9 ±1.15 nT). However, it is the very low Alfvenic Mach number that is intriguing. The Alfvenic Mach number for the solar wind is very low at 2.7 ±0.31. The solar wind number density is also low at 2.83 ±0.50 cm^{-3}.

3.1.2 Event 2: Driven Recovery Phase BRI (February 15, 1998)

The second BRI occurs on February 15, 1998 and lasts from 00:00 UT to 04:05 UT. While this event is considered a Balanced Reconnection Interval, since the F_{pc} remains steady at 0.42±0.02 for over 4 hours, it would probably be better described as a driven recovery phase. Figure 3.4 shows a substorm with an expansion phase onset at 22:40 UT, but after the hour long recovery phase the F_{pc} remains steady for 4.25 hours and the aurora remains bright. The CPCP, AL, and AE also show a higher level of activity in the auroral zone until 02:16 UT, when they begin to decay to quiet time levels (AE 735 to 200 nT, AL -464 to -75 nT, and CPCP 78 to 33 kV). The event ends when AE drops below 200 nT at 04:05 UT. The auroral activity declines as the IMF B_z slowly starts to turn northward at about 02:00 UT. The activity returns to quiet levels approximately half an hour after the IMF B_z has turned completely north. It is the extended southward IMF B_z and its slow northward turning that allows the magnetotail to slowly relax back to a quiet state without first unbalancing the reconnection rates. Thus, the recovery phase of the first substorm is still being driven by the IMF B_z southward until the magnetosphere relaxes.

Figure 3.5 shows the propagated solar wind /IMF data from the ACE satellite. The solar wind during this event appears to be at nominal levels. The Mach number

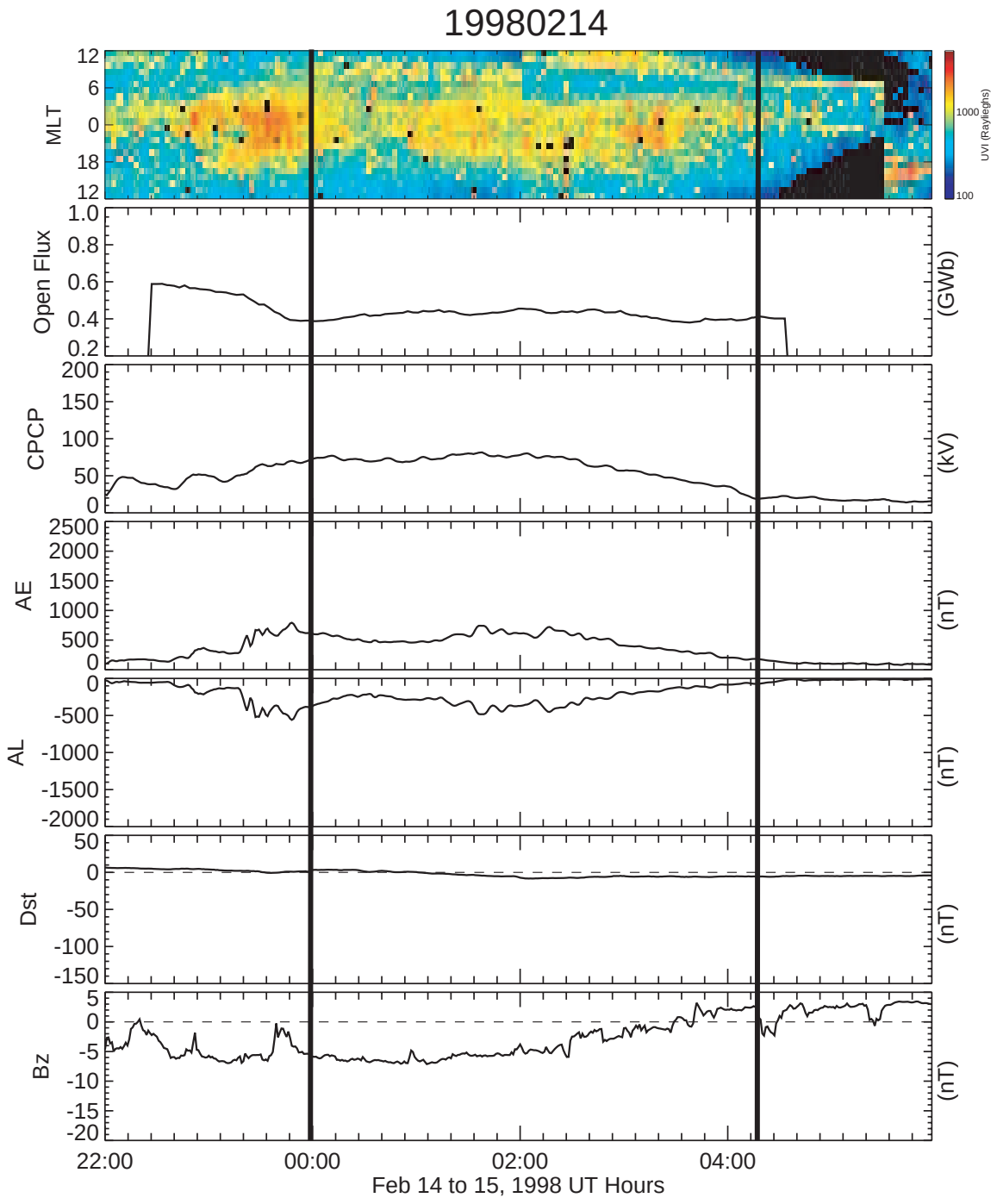

Figure 3.4: A stack plot of the data for the BRI on Feb. 14 and 15, 1998 (Event 2). The set up is the same as Figure 3.1.

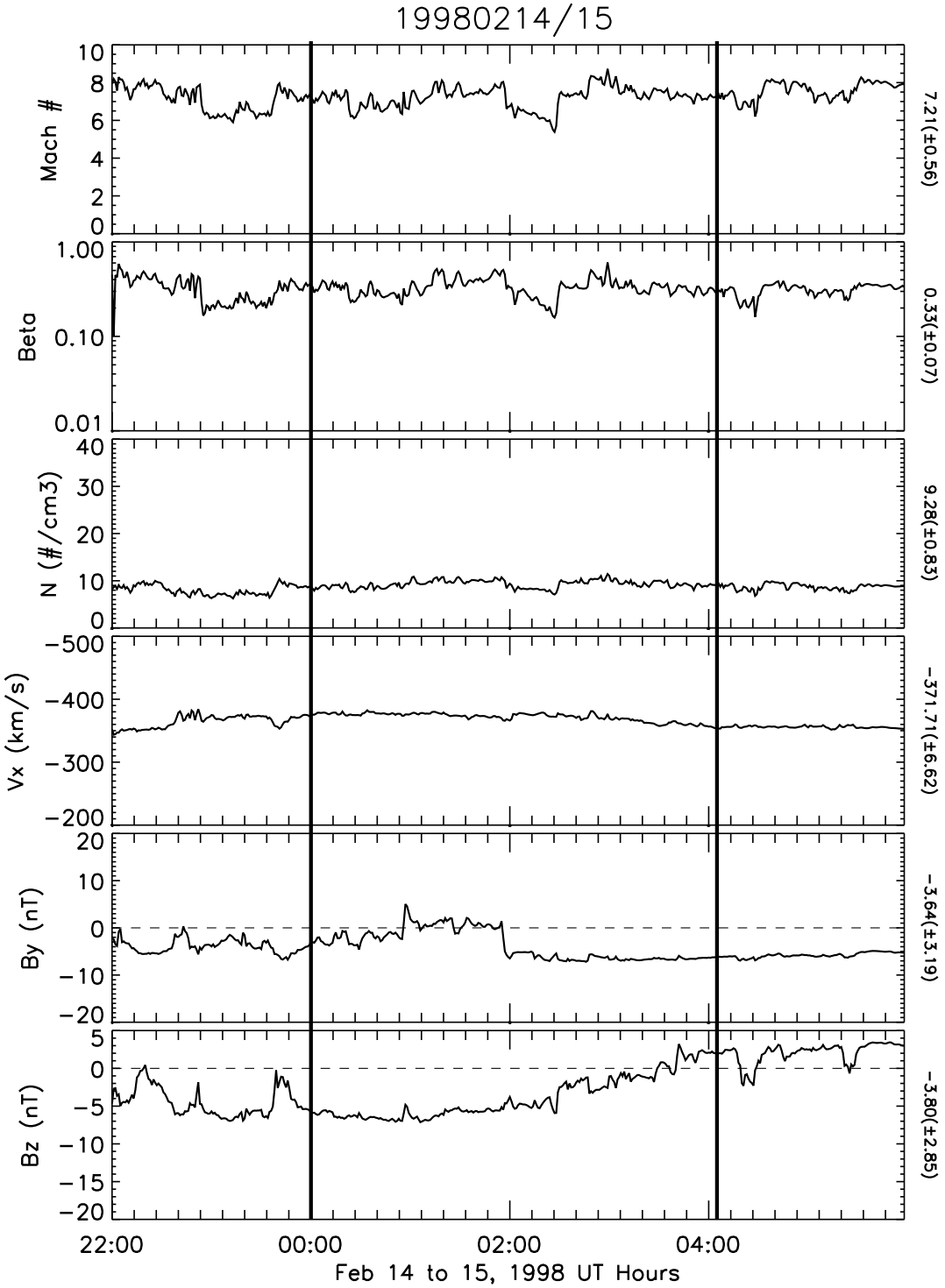

Figure 3.5: Propagated ACE data for the BRI on Feb. 14 and 15, 1998 (Event 2). The set up is the same as Figure 3.3.

is steady at about 7.2 ±0.56, while Beta (0.33 ±0.07) and number density (9.28 ±0.83 cm^{-3}) are also at "average" levels. The IMF/solar wind data remains fairly stead,y and B_z appears to be the only major driver during this event.

3.1.3 Event 3: No substorm to initiate BRI (December 22 & 23, 2000)

While the previous BRI started with a substorm and ended when the magnetosphere relaxed back to quiet levels, the BRI on December 22 and 23, 2000 starts when the magnetosphere slowly rises to active levels and ends with a substorm. This event is stronger and brighter than the last two examined. The BRI starts at 21:42 UT when AE becomes greater than 200 nT. AE then slowly rises to 946 nT. AL slowly drops (-134 to -541 nT) during this time, indicating a slow increase in magnetospheric activity. However, no disruptions that indicate a substorm expansion occurs during this time interval. The top panel of Figure 3.6 shows the aurora slowly becoming more active, but once again, there is no sign of a substorm expansion in the aurora or in other data. At 23:30 UT there is a large northward turning of the IMF B_z that one would expect to trigger an expansion phase of a substorm. There is a brightening in the aurora at this time close to dawn (18 MLT), but there is no response in AL, no westward traveling surge, and poleward expansion of the oval. Thus, it is considered to be a pseudo-breakup [*Koskinen et al.*, 1993; *Kullen and Karlsson*, 2004]. During the rest of the event, the F_{pc} remains steady at 0.76±0.05 GWb until the substorm at 04:49 UT. Once again it is difficult to separate the BRI and the growth phase of the concluding substorm, due to the F_{pc} remaining steady until the onset of the expansion phase. However, during this event the substorm expansion does not appear to be triggered by a northward turing of the IMF B_z. This is similar to the event investigated by *Yahnin et al.* [1994], where there appears

to be no trigger for the concluding substorm expansion of the SMC. The reason for the change in reconnection rates is unknown at this time but it is most likely due to an internal process in the magnetosphere.

The D^*_{st} derived from AMIE is relatively high (-12 nT), indicating that there is not a storm occurring in the magnetosphere at this time. However, the hourly D_{st} drops to -55 nT at 04:00 UT on the 23^{rd}, which implies that the BRI event happens during the main phase of a weak magnetic storm. The difference between these two measurements could indicate that there may be a lot of structure in the inner magnetosphere. When more magnetometers are used, as in D^*_{st}, they average out to zero, while when only 4 magnetometers are used, a more disturbed picture of the inner magnetosphere arises.

Figure 3.7 shows the Weimer propagated ACE data for this event. While there is not solar wind data for the entire event, what is shown remains unsteady. At the start of the BRI, the Alfvenic mach number is 6 and quickly moves up to 9.8. It then drops back down to 2.6 30 minutes later, rising back to 7 and falling to 2.5 45 minutes later. At 00:13 UT on the 23^{rd}, it remains low, at close to 3, until the data ends. The solar wind Beta and number density follow a similar pattern. By observing just solar wind density or dynamic pressure, one would expect to see a large increase in auroral activity during this event [*Chua et al.*, 2001; *Boudouridis et al.*, 2003, 2004] , yet there is not. One of the most interesting observations about this event is that the solar wind/IMF remains less steady than during the other events. There is a large spike in the IMF B_z at approximately 23:30 UT that does not appear to have a large geomagnetic impact. At the same time as the spike in B_z, the solar wind Vy drops from 0 to ∼-55 km/s and the Vz drops from 0 to ∼-80 km/s for approximately 30 minutes then they both return to zero. This may indicate that the short increase

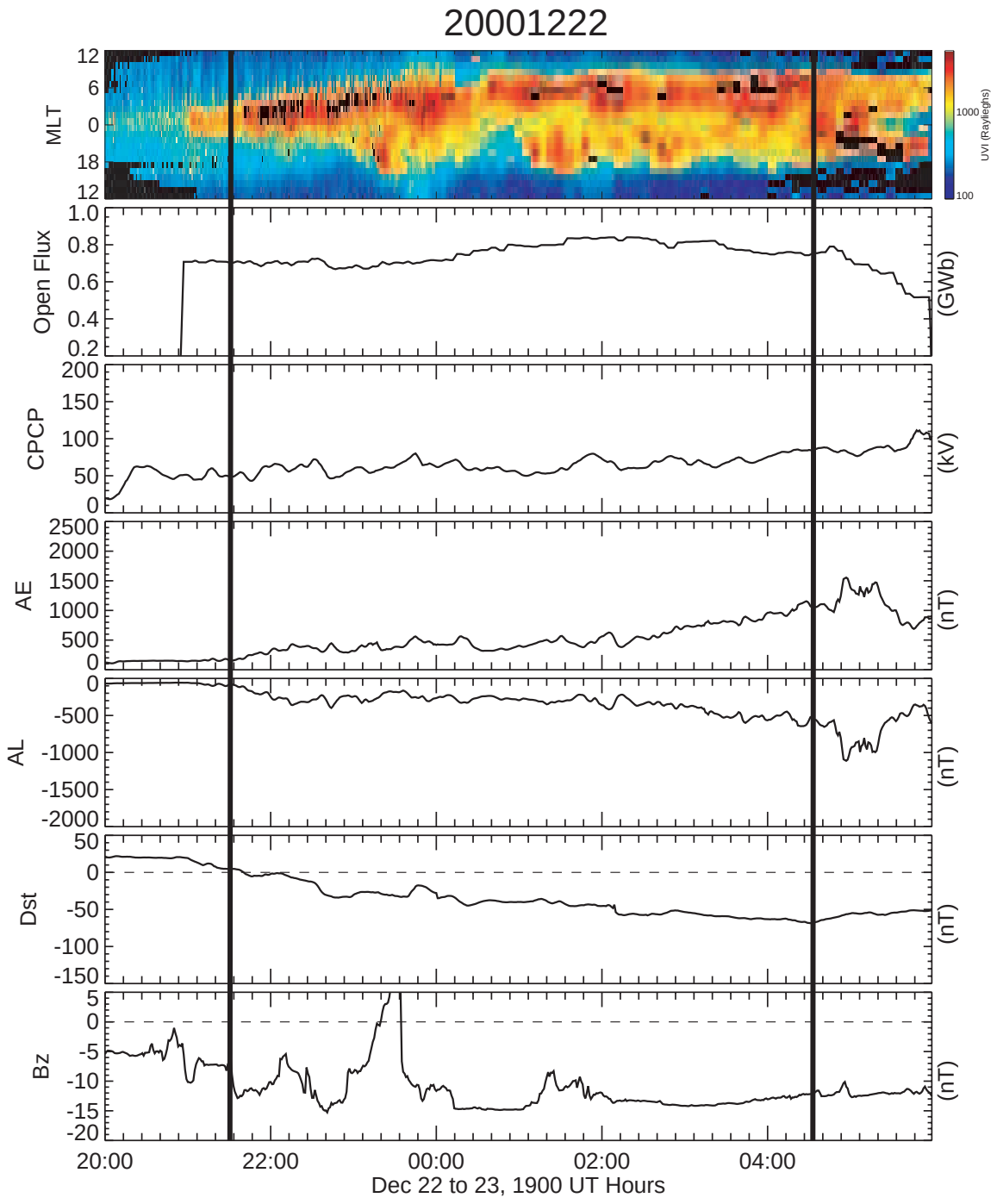

Figure 3.6: A stack plot of the data for the BRI Dec. 22 and 23, 2000 (Event 3). The set up is the same as Figures 3.1 and 3.4

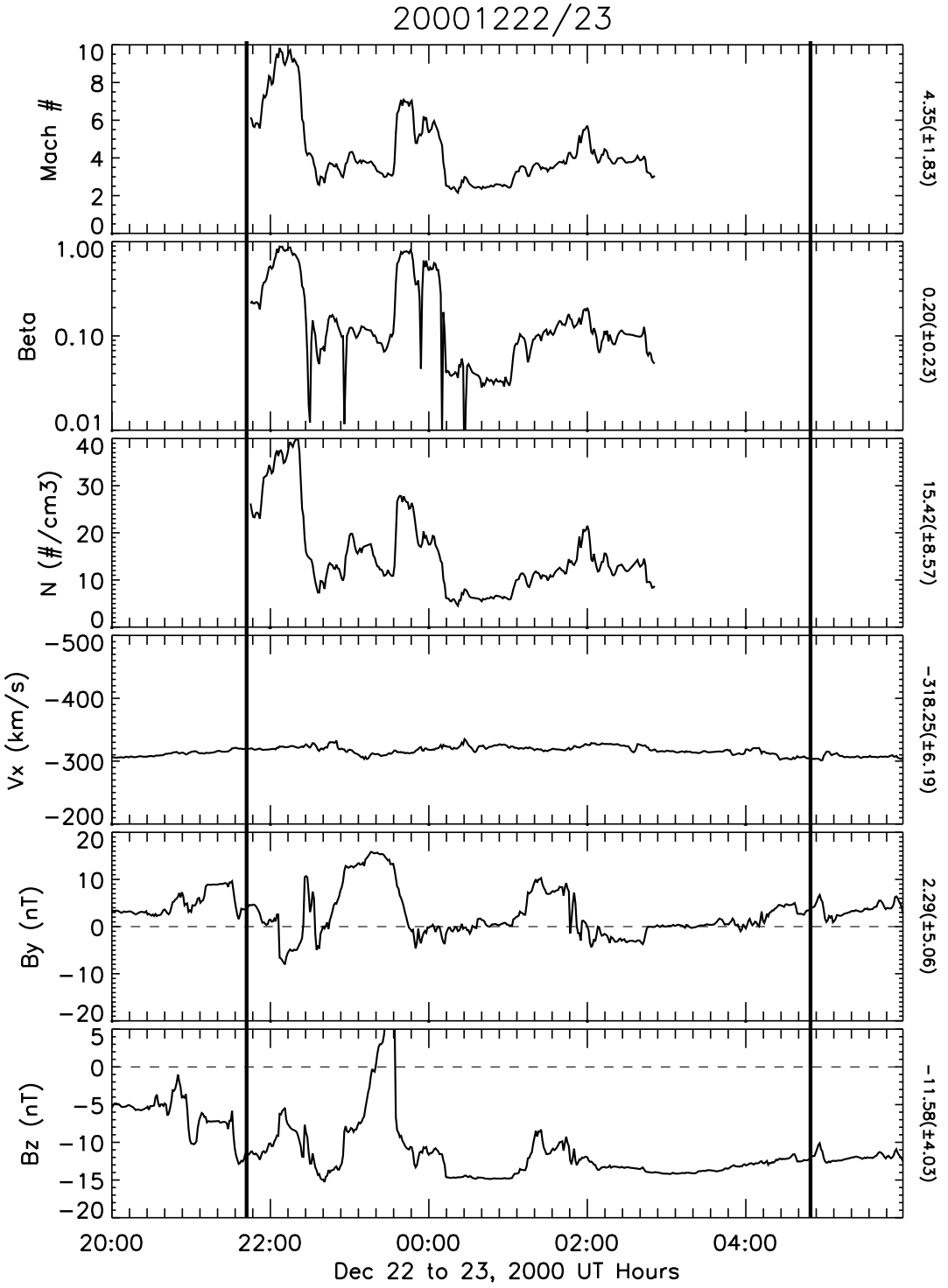

Figure 3.7: Propagated ACE data for the BRI on Dec. 22 and 23, 2000 (Event 3). The set up is the same as Figures 3.3 and 3.5.

in B_z does not hit the Earth's magnetosphere.

3.1.4 Event 4: Active slow growth BRI (February 17, 1998)

The last BRI to be investigated occures on February 17, 1998 and shows a slow growth in F_{pc} after a 5.67 hour period of steadiness. Figure 3.8 shows that there is a substorm expansion at 14:15 UT (determined by AL) that precedes the BRI starting at 15:45 UT when AL becomes steady. F_{pc} is not used to determine the start of the BRI, because the Polar UVI coverage does not start until 16:00 UT. While there are small perturbations in CPCP, AL, and AE, none of the variations are large enough or last long enough to constitute a substorm expansion. AE fluctuates between 585 and 1232 nT with an average of 834 nT, increasing to 1500 nT and remain there for half an hour before the second substorm occurs. AL fluctuates between -277 and -915 nT with an average of -538 nT. While these variations may seem large, compared to the substorms that begin and end the event they are small in size and time scale. Thus, they are not consistent with substorms expansions during this time interval. The event ends at 21:22 when the growth phase of the substorm starts. The two hour long growth phase is not considered part of the BRI, since the F_{pc} increases by more than 10% per hour during this time.

The substorm expansion at 23:19 UT is not observed in the F_{pc}, but is determined by the large decrease in AL. This is consistent with a more negative IMF B_z, which increases the merging rate on the dayside. Thus, even though there is a substorm, the F_{pc} continues to increase since the dayside merging rate is greater than nightside reconnection rate [*Milan et al.*, 2007]. *Milan et al.* [2007] investigates a similar nightside reconnection event and suggests that this only occurs when the F_{pc} becomes greater than 0.8 GWb. At the onset of the substorm at 23:19 UT, the F_{pc} measures

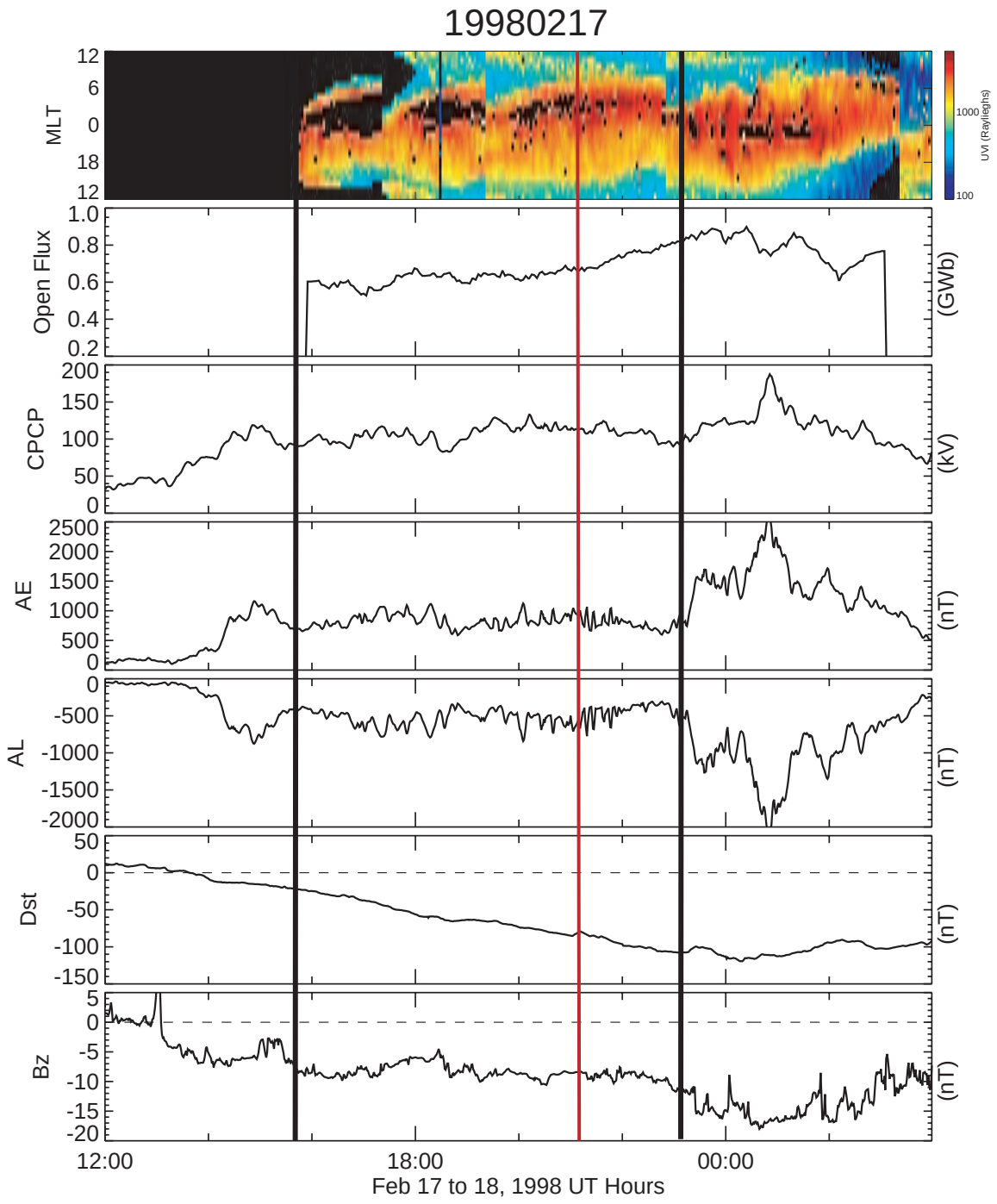

Figure 3.8: A stack plot of the data for the BRI on Feb. 17, 1998 (Event 4). The same set up as Figures 3.1, 3.4 and 3.6. The solid black vertical lines represent the beginning and ending of the BRI. The dotted line is the onset of the substorm at 23:19 UT.

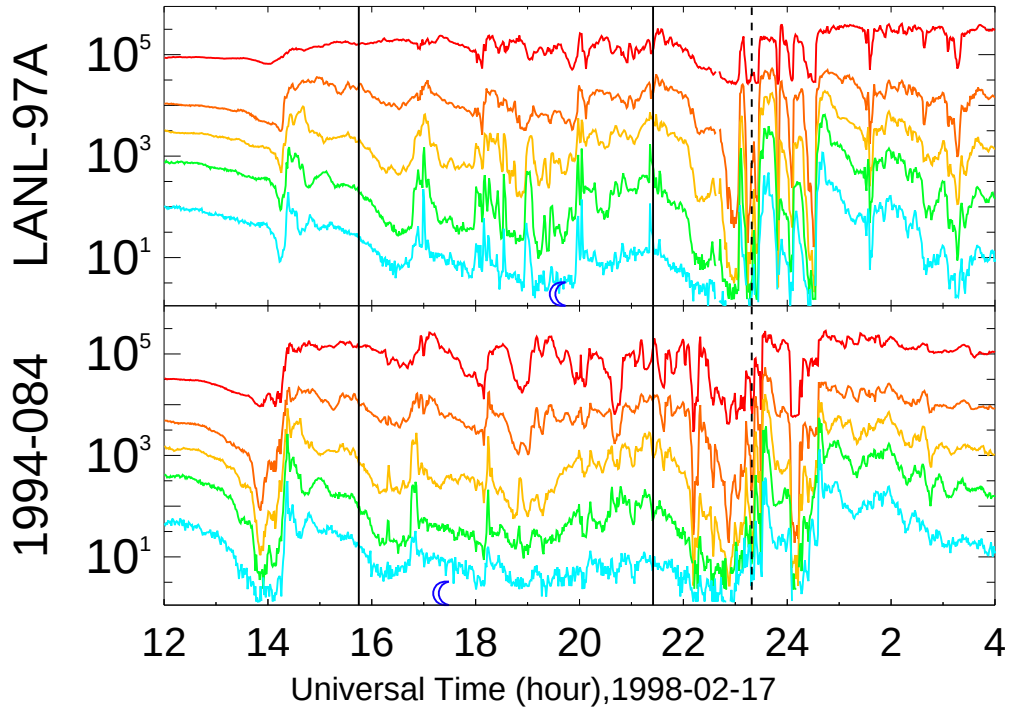

Figure 3.9: LANL SOPA Proton data for Event 4. Each color is a different energy channel with red as the lowest energy and blue as the highest. The blue moon represents when the satellite is at local midnight and the red star is local noon. Once again, the solid black vertical lines represent the beginning and the ending of the BRI and the dotted line is the substorm at 23:19 UT.

0.84 GWb and continues to increase to 0.9 GWb, before it starts to drop at 00:45 UT on the 18^{th}.

This event is moderately active with the CPCP of approximately 106 kV and AE at 834 nT. The D_{st} is dropping from -10 to -80 nT during this event, implying it takes place during the main phase a geomagnetic storm. The IMF B_z is strong and southward during this event: - 8 $\pm$1.15 nT, such that one might expect to see a periodic sawtooth oscillation [*Henderson et al.*, 2006a] instead of balanced reconnection. In order to show that it is not a sawtooth event, the LANL SOPA proton data is shown in Figure 3.9. While there are small perturbations in the data, there are no signatures of stretching or injections consistent with a substorm

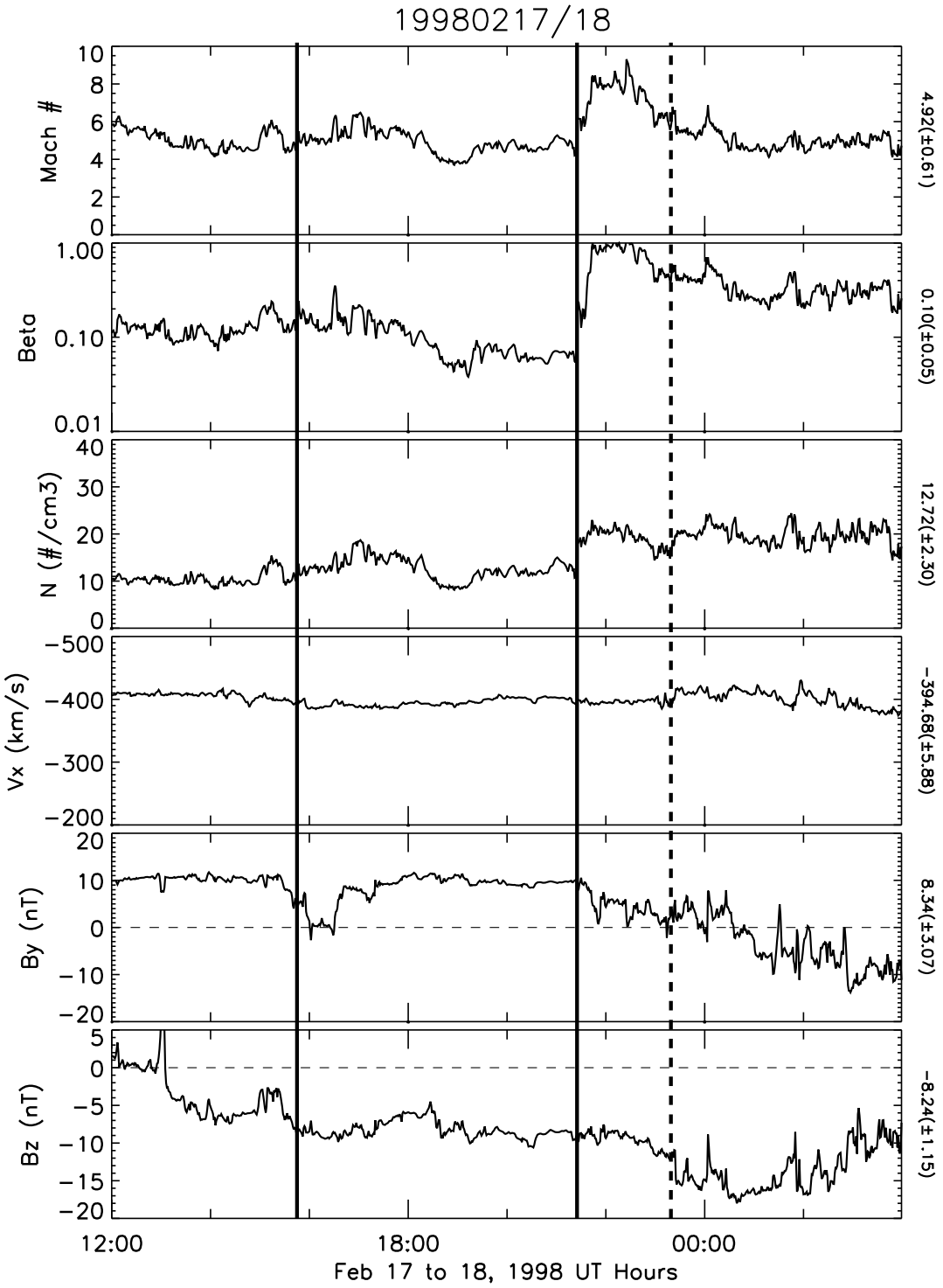

Figure 3.10: Propagated ACE data for the BRI on Feb. 17, 1998 (Event 4). The set up is the same as Figures 3.3, 3.5, and 3.7. Once again, the solid vertical lines represent the beginning and the ending of the BRI, and the dotted line is the substorm at 23:19 UT.

or a sawtooth oscillation. The small perturbations appear to be different than the substorms at 14:15 and 23:19 UT where the particle densities drop, as the magnetotail is stretched, and then inject back into the inner magnetosphere during dipolarization.

The solar wind and IMF are steady for the first 5.5 hours of the event as shown in Figure 3.10. At 21:25 UT, around the same that the F_{pc} starts to grow, the density increases from 11 to 20 cm^{-3} and remains close to 20 cm^{-3} for the next hour and a half. Since the solar wind velocity and IMF B_z both remain steady at this time, the increase in density causes both the Alfvenic Mach number and the solar wind Beta to increase. *Ober et al.* [2007] shows that an increase in the solar wind density of this type (with other parameters held constant) can cause the open flux in the polar cap to increase. Thus, it is most likely the 9 cm^{-3} increase in the density causes the F_{pc} to increase, initiating the growth phase.

3.2 Discussion

The fundamental question that is at issue in the study of SMCs or BRIs is: What allows reconnection rates to balance? According to *Sergeev et al.* [1996], the magnetosphere must first unload its tail flux in the form of a substorm expansion before the reconnection rates can balance. They propose that SMCs (BRIs) may occur when the plasma sheet is thick, as during the recovery phase, and while the B_z driver remains enhanced. Thus, the near-Earth tail develops a growth phase type configuration, while the mid-tail region persists in the expansive state. This magnetospheric configuration gives the minimum B_z they measured in the equatorial magnetic field near 12 R_E. Although this paper does not explore the tail region during these events, this explanation set forth by *Sergeev et al.* [1996] does not hold for all of the events studied, since Event 3 does not start with a substorm. It appears

that in Event 3 the magnetosphere is already in a state that allows the reconnection rates to balance without the need for the recovery and expansion phases discussed by *Sergeev et al.* [1996]. Thus, it seems that preconditioning of the magnetosphere may play a role in some BRI events.

This investigation shows that there are least three different processes that can cause the reconnection rates to become unbalanced: (1) the dayside reconnection reduces significantly (Events 1 and 2), (2) the dayside reconnection increases without an increase in the nightside rate (increased driving) (Event 4), (3) some internal process causes a substorm to occur (Event 3). Events 1 and 2 cease when the dayside reconnection is reduced. In Event 1 the IMF B_z turns northward suddenly, causing a new reconnection point to form, and a substorm ensues. During Event 2 the IMF B_z takes 2 hours to turn northward. This allows the reconnection on the nightside to maintain balance, but once the IMF B_z is fully northward and reconnection on the dayside is reduced significantly, the event ends. Event 3 appears to end without a trigger in the solar wind/IMF, suggesting a stochastic process causes a new reconnection point to form. *Milan et al.* [2007] find that 50% of their untriggered tail reconnection events occur when the $F_{pc} > 0.7$ GWb, leading them to conclude that these events happen spontaneously due to stresses in the tail. Event 3 has an average F_{pc} of 0.76 ($\pm$0.05) GWb and is the only untriggered event. Even though the events of *Milan et al.* [2007] are not preceded by a BRI, the physics appears to be the same. Finally, Event 4 ends with an increase in dayside reconnection, due to an increase in the number density in the solar wind, while the nightside reconnection presumably stays the same. This causes flux loading in the tail and a growth in the F_{pc}.

Another way to analyze the conclusion of these events is in terms of substorms.

Once again 3 different endings for the events were found: (1) substorm growth phase (Event 4), (2) substorm expansion phase (Events 1 and 3), and (3) no substorm (Event 2). Events 1 and 3 end abruptly with the appearance of a substorm expansion phase in the data. In Event 1 the dayside reconnection rate ceases, causing nightside reconnection to be larger than the dayside and the expansion phases ensues. However, in Event 3 there appears to be no turning off of the dayside reconnection. Event 4 ends when the F_{pc} begins to grow for 2 hours preceding the substorm. The growth in F_{pc} is caused by the build up of magnetic flux in the tail that occurs during the growth phase of a substorm.

The solar wind/IMF drivers for all four events are fairly steady. Thus, the notion that SMCs (BRIs) occur when the IMF B_z is negative and steady still holds for these events. There are some perturbations in the ACE data for Event 3 that do not appear to impact the BRI. The IMF B_z for all of the events is less than -5 nT. This differs from previous studies that state: steady magnetospheric convection usually occurs when 0 nT > $B_z \geq$ -5 nT [*Sergeev et al.*, 1996; *O'Brien et al.*, 2002; *Tanskanen et al.*, 2005]. Event 1 has a B_z close to -6 nT and Event 2 starts with a B_z of -5 nT before it starts to turn northward. Events 3 and 4 both have a larger magnitude of the IMF B_z (-12 and -8 nT, respectively) than expected for this type of event. Another interesting driver to note is the solar wind Beta and Alfvenic Mach number. With the exception of Event 2, they are all lower than the"average" solar wind beta and Mach number. The solar wind/IMF drivers will be studied in more detail in a future paper that includes a statistical analysis of 51 BRI events.

While the drivers during these events are considered relative constant, the magnetospheric data is not as steady. Once again, Events 1 and 2 are the most steady and most closely fall into the category of an SMC. Event 3 has a slow growth in the

AL, indicating that the activity in the auroral zone is increasing during this event. There is also an auroral brightening or pseudo-breakup during this event. Thus, the magnetosphere is not completely steady, yet the global reconnection rates are still relatively balanced in a global sense. Event 4 is by far the most "active" event. There are variations in AL, AE, and CPCP along with an active aurora. Also, D_{st} and LANL SOPA proton data indicate that the inner magnetosphere is still dynamic during this event. The variations in the data during Events 3 and 4 are what *Sergeev et al.* [1996] refer to as "mesoscale transient activations" and can occur during SMC events. However, Event 4 has more activity than any of the events studied by *Sergeev et al.* [1996]. It also has a larger CPCP (106.7±11 kV) than any event they studied, because they only selected events with a CPCP between 60 and 90 kV. Thus, Event 4 is stronger, and therefore, so are the "mesoscale transient activations." Although the last two events are not "steady", they are classified as BRIs because the global dayside and nightside reconnection rates balance and they lack signatures of large-scale tail reconfiguration [*Sergeev et al.*, 1996]. A further study will investigate statistically the steadiness in the solar wind drivers and auroral zone indices for more BRIs.

Events 3 and 4 also raise the notion of preconditioning in the magnetosphere. *Sergeev et al.* [1996] describe a steady magnetospheric configuration in the near-Earth tail region as stretched with a thin current sheet. They also state that the midtail region posses a thick plasma sheet and an enhanced equatorial magnetic field. Thus, in those events, the near-Earth magnetic field lines and current resemble those that occur during a substorm expansion phase. Meanwhile, the midtail region appears to have a configuration that is close to a substorm growth phase. This suggests that the magnetosphere should need to go through an expansion phase before the SMC

can begin, yet this is not what occurs during Event 3. This event begins with the magnetosphere slowly becoming more active without a substorm expansion. This implies that the inner magnetosphere may already have a thin current sheet before Event 3 begins. This type of preconditioning may also play a role in Event 4 when, according to the solar wind/IMF drivers, periodic sawtooth oscillations should occur. There may be some internal mechanism that causes the magnetotail to adopt this configuration instead of forming a new reconnection point. In order to determine the role of magnetospheric preconditioning on BRIs, a more in-depth investigation is needed, utilizing more data and possibly modeling efforts.

3.3 Conclusion

This investigation illustrates the diversity of BRIs (SMCs). In order to truly understand the physics behind balanced reconnection in the magnetosphere, we must broaden our studies of "SMCs" and redefine them physically as Balanced Reconnection Intervals (BRIs). Applying the term "steady" to a system as large and complex as the magnetosphere poses fundamental problems. Convection can remain quasi-steady on a global scale, while small scale perturbations are still occurring. Ultimately, the only way to achieve this large scale steadiness is through a balance of dayside and nightside reconnection rates. Thus, the new name of Balanced Reconnection Interval (BRI) better describes the physical state of the magnetosphere than Steady Magnetospheric Convection (SMC).

The measurement of open magnetic flux in the polar cap (F_{pc}) is a much better indicator of the balance between dayside and nightside reconnection rates than auroral indices, such as AL and CPCP. For example, if the reconnection rates stop balancing due to an increase in the dayside reconnection rates, as in Event 4, this

can be measured in the F_{pc}. However, this change in reconnection rates is difficult to observe in AL or CPCP. This new definition eliminates the need to estimate the concluding time of a BRI. Previous studies first determine the onset time of the expansion phase of the concluding substorm and then subtract the average growth phase length to determine the end time of the SMC. This technique may cause BRIs to appear shorter than they actually are. For instance, Events 1 and 3 do not show a growth phase in the F_{pc}, suggesting that the reconnection rates stay balanced until the onset of the concluding substorm expansion phase. Thus, the new definition of BRI allows for the inclusion of this time period, instead of simply stating that SMCs end with the growth phase.

In conclusion, the name balanced reconnection intervals allows for a more precise and physical description of these type of events, eliminating confusion over the term "steady". By using the F_{pc} to identify these events, a larger range of activity levels and more diverse events can be included in this classification. Furthermore, the F_{pc} measures the beginning and end times of event more accurately, allowing the entire event and only the event to be studied

CHAPTER IV

Aurora and open magnetic flux during isolated substorms, sawteeth and SMC events

This chapter will addresses the second question list in the introduction, "What are the similarities and differences in the F_{pc} and therefor the convection during different convection modes?" Thus, this chapter examines the similarities and differences in the auroral signatures and open magnetic flux in the polar cap, as determined using global auroral imaging, for these three classes of events.

The study in this chapter is broken up into two parts. The first part presents a case study for each type of event. For ease of comparison, only IMAGE Far Ultraviolet imager (FUV) data is used in this section. The events were chosen for good imaging coverage and limited dayglow. The second part presents a limited statistical study of the polar cap open flux (F_{pc}) for the different types of events. In order to maximize the amount of data, we use both IMAGE FUV and Polar Ultraviolet Imager (UVI). From FUV, we use the Wideband Imaging Camera (WIC) and from UVI we use Lyman-Birge-Hopfield long (LBHl). This part of the study includes events from all seasons, since we have methods of removing dayglow, based on *Immel et al.* [2000], that allow us to identify the dayside boundary during summer, spring, and fall events.

4.1 Case Studies

4.1.1 Isolated Substorm

In order too identify an event as a substorm, we require a clear mid-latitude positive bay, indicating a substorm current wedge, in mid-latitude magnetometer data [*Clauer and McPherron*, 1974]. The onset of the expansion phase occurs when the first magnetometer starts to see the positive bay. For better visualization, the magnetometer data has been used to create a Magnetic Local Time - Universal Time (MLT-UT) map [*Clauer and McPherron*, 1974]. Figure 4.1 illustrates an MLT-UT map for the substorm that occurred on January 4, 2001 at 06:47 UT. The red represents a positive change in the data where the blue is a decrease in the data. The local time disturbance measured at the onset set time has been subtracted from all subsequent profiles to provide a better characterization of the substorm and to enable better comparison with other events. While the magnetometer data shows the expansion phase onset at 06:47 UT, as represented by the large red structure that starts at 06:47 UT and spans 21 to 03 MLT, it does not appear in the FUV images until 06:52 UT. We find a similar shift of onset times in many of our substorms, so for consistency we use the ground magnetometer data alone to determine the onset times.

Figure 4.2 shows a stack plot of keograms with the F_{pc} plotted at the bottom. For reference, 4 images of the aurora throughout the period are shown on the left. Although others [*Brittnacher et al.*, 1999; *Milan et al.*, 2003] have examined substorms in this fashion, we feel it necessary to have a typical isolated substorm in this study for comparison. The keograms in Figure 4.2 go from approximately 1 hour before expansion phase onset to 2 hours after. The aurora is fairly quiescent before the onset and the onset is first seen at 22 MLT at 06:52 UT. The substorm then

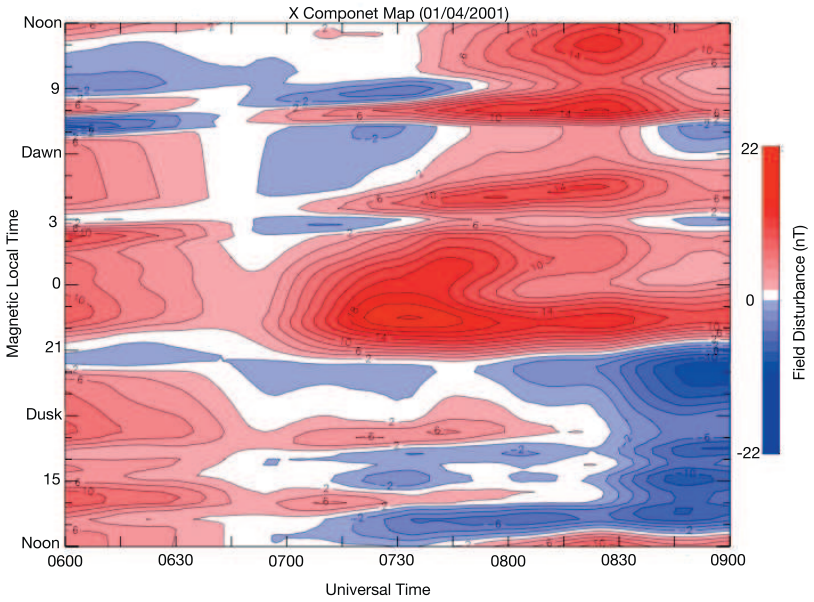

Figure 4.1: An MLT-UT map of mid-latitude magnetic perturbations for the isolated substorm on January 04, 2001

spreads out toward dawn and midnight. Although the substorm is stronger (more intense) on the dusk side, it extends over a greater MLT range on the dawn side. The intensity of the aurora reaches 6000 Rayleighs during the expansion phase and then weakens during the recovery phase. From the keograms, it can also be seen that the intensifications occur more poleward (top of the keogram) at 20, 22 and 00 MLT.

The amount of open polar cap flux in Giga-Webers is plotted on the bottom of Figure 4.2. The F_{pc} increases slightly as magnetic flux builds up in the tail, due to an increase in dayside merging, until it reaches a maximum of 0.72 GWb 10 minutes after onset of the expansion phase. Then, it decreases as magnetic flux is released from the tail during dipolarization, which is caused by an increase in the night side merging rate. The open flux continues to decrease until 07:47 UT when it reaches a minimum of 0.42 GWb after which it becomes steady. Thus, the total amount of flux

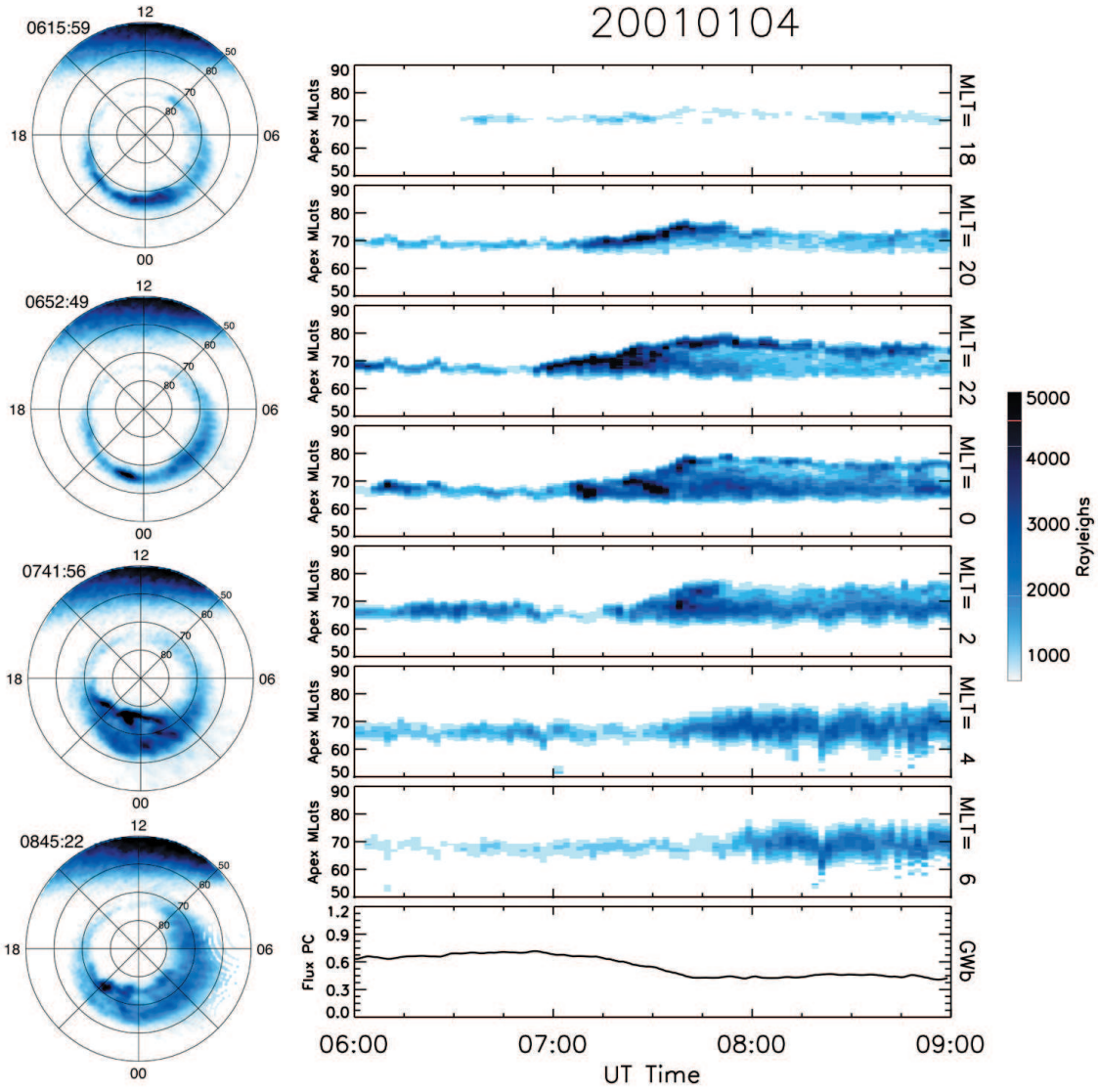

Figure 4.2: A stack plot of keograms for the isolated substorm on Jan. 04, 2001. The polar cap open magnetic flux is plotted at the bottom. For reference, there are images of the aurora through out the period shown. The color indicates intensity of the aurora in Raylieghs

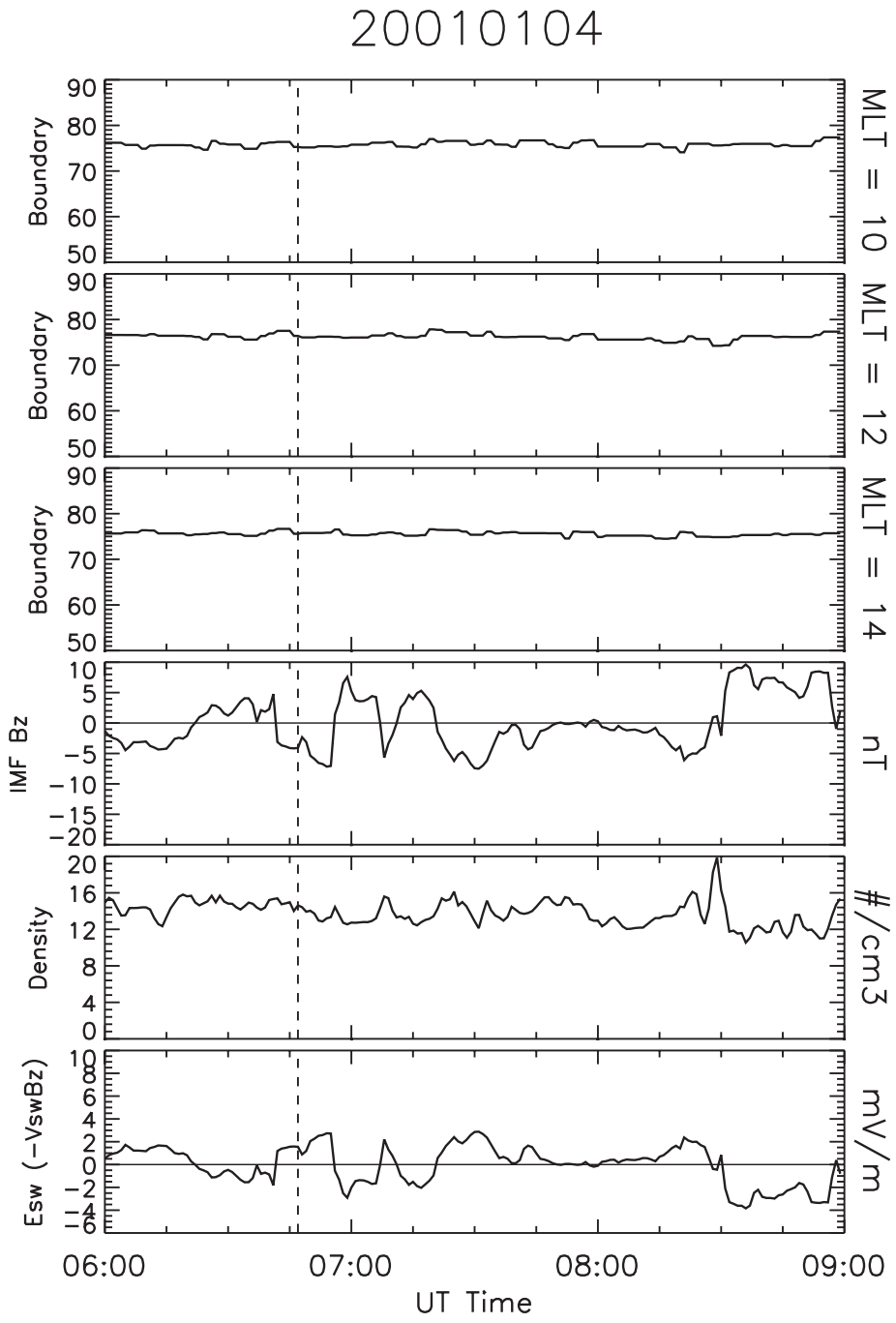

Figure 4.3: A stack plot of the dayside boundaries for the isolated substorm on Jan. 04, 2001. (a) The magnetic latitude of boundary at 10 MLT. (b) Magnetic latitude of the boundary at Noon. (c) Magnetic latitude of the boundary at 14 MLT. (d). IMF B_z (nT) (e) Solar wind proton density (number/cm^3) (f) The electric field (mV/m) of the solar wind calculated using the solar wind velocity and B_z. The vertical line represent the onset of the expansion phase of the substorm as seen in ground based magnetometer data.

released from the magnetosphere during this substorm is 0.30 GWb which is 42% of the maximum amount of flux.

Figure 4.3 is a stack plot of the magnetic latitude of the dayside boundary along with a few solar wind/IMF parameters, the vertical line is the onset time of the substorm from ground based magnetometer data. The purpose of showing only the boundary location and not the full keogram lies in our dayglow removal process. The dayside can be clearly seen in individual images of the auroral, but our dayglow removal creates a dark line across the terminator, thus when a keogram is created it is difficult to distinguish between the terminator and the dayside boundary. Since our other two cases studied here occur during October the dayside boundary and the terminator are coincident at many times. So for consistency we have chosen just to plot the dayside boundary. The interplanetary magnetic field (IMF) and solar wind parameters have been propagated to Earth using the *Weimer et al.* [2002]; *Weimer et al.* [2003]; *Weimer* [2004] psuedo-minimum variance technique. The propagation is accurate to approximate 6 minutes, thus onsets and triggers may not occur at the exact same time. The solar wind density and IMF B_z are plotted due to their role in as a possible trigger for a substorm onset. And E_{sw} is shown since it the major solar wind/IMF component for dayside reconnection [*Milan*, 2004; *Milan et al.*, 2006]. Note that when E_{sw} is positive there is dayside reconnection since B_z is negative. The solar wind/IMF parameters are not very steady and it is difficult to say if there is trigger for the onset of this substorm. However, we could be missing the exact trigger since the propagation time could be a little offset. It is interesting to note that even though the E_{sw} fluctuates from positive to negative during this time it seems to have little effect on the dayside boundary location.

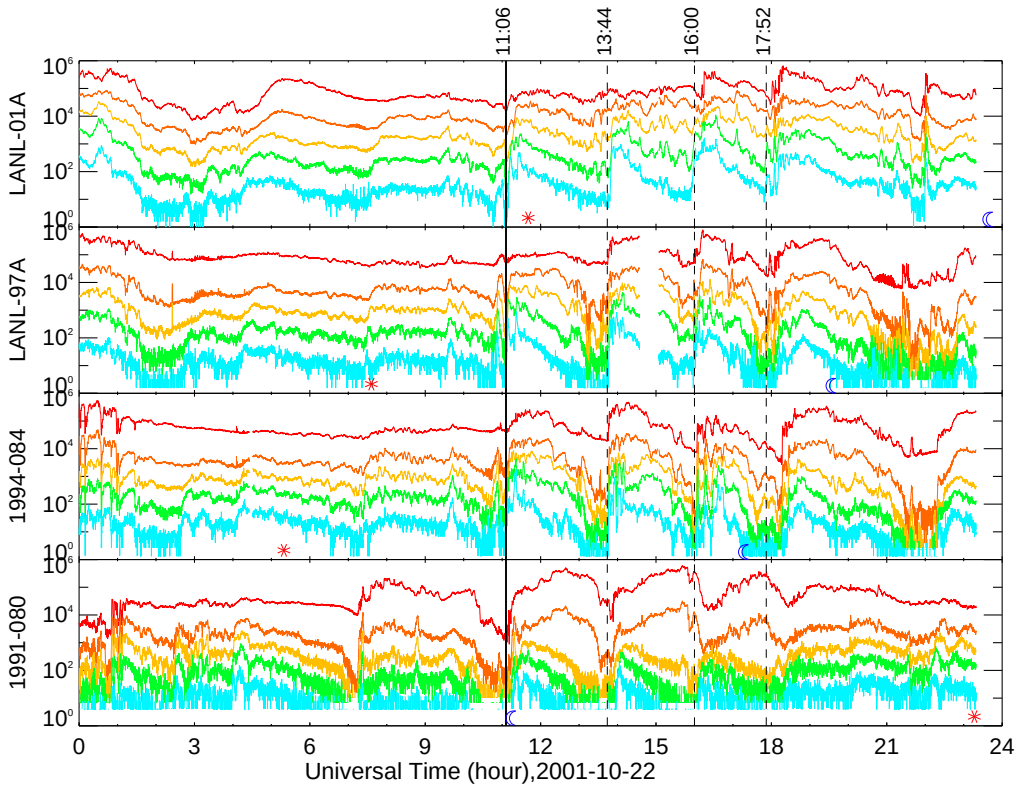

Figure 4.4: Plot of LANL SOPA proton data for the sawtooth event on October 22, 2001.The vertical lines illustrate the onset times of the individual teeth.

4.1.2 Individual Sawtooth

Sawtooth oscillations are so named because of their appearance in the Los Alamos National Laboratory (LANL) Synchronous Orbit Particle Analyzer (SOPA) proton particle flux data. The particle injections, which have a sawtooth like shape, are seen globally and have a periodicity of 2-4 hours.

Sawtooth oscillations are so named because of their appearance in the Los Alamos National Laboratory (LANL) Synchronous Orbit Particle Analyzer (SOPA) proton particle flux data. The particle injections, which have a sawtooth like shape, are seen globally and have a periodicity of 2-4 hours.

Although most studies of sawtooth oscillations have included the entire event, which covers many injections, we will concentrate on only one injection as part of

our single event analysis. We use the injection at 11:06 UT on October 22, 2001. The sawtooth event is shown in its entirety in Figure 4.4, which is a plot of the LANL SOPA proton data at geosynchronous orbit. It is the first injection in this series, and was chosen because the aurora imaging data covers the entire injection and there is little dayglow.

The onsets for all of the injections are determined by LANL geosynchronous SOPA proton data. We define the onset with the same criteria in *Cai et al.* [2006a]. Due to the auroral activity before the each injection, it is difficult to see an exact onset in the auroral data. Thus, it is hard to quantify any time delay in the onsets.

Figure 4.5 uses the same format as Figure 4.2. The images on the left of the figure do not have dayglow removed so that the night side aurora can be better seen. There is also no dayglow removal for the keograms, as they are all night side MLTs. The lack of dayglow removal also allows for a better comparison between the intensities of the events. However, dayglow had to be remove in order to measure the dayside boundary to obtain the polar cap flux (F_{pc}).

In comparing Figures 4.5 and 4.2 we can see that the sawtooth is much more intense than the isolated substorm. There is also more auroral activity before the onset. One of the major differences is the extent of the auroral movement in MLT. The isolated substorm studied here is concentrated on the dawn side, whereas the sawtooth extends to 06 and 18 MLT and beyond. In general isolated substorms are more localized in magnetic local time than individual sawteeth. The maximum intensity of the aurora for the sawtooth is about 15,000 Rayleighs (15kR) – more than 2 times as intense as the substorm. The intensifications also appear to be more equatorward in 22-06 MLT keograms, with some brightening poleward in 18 and 20 MLT keograms. This appears to be part of the double oval discussed in the

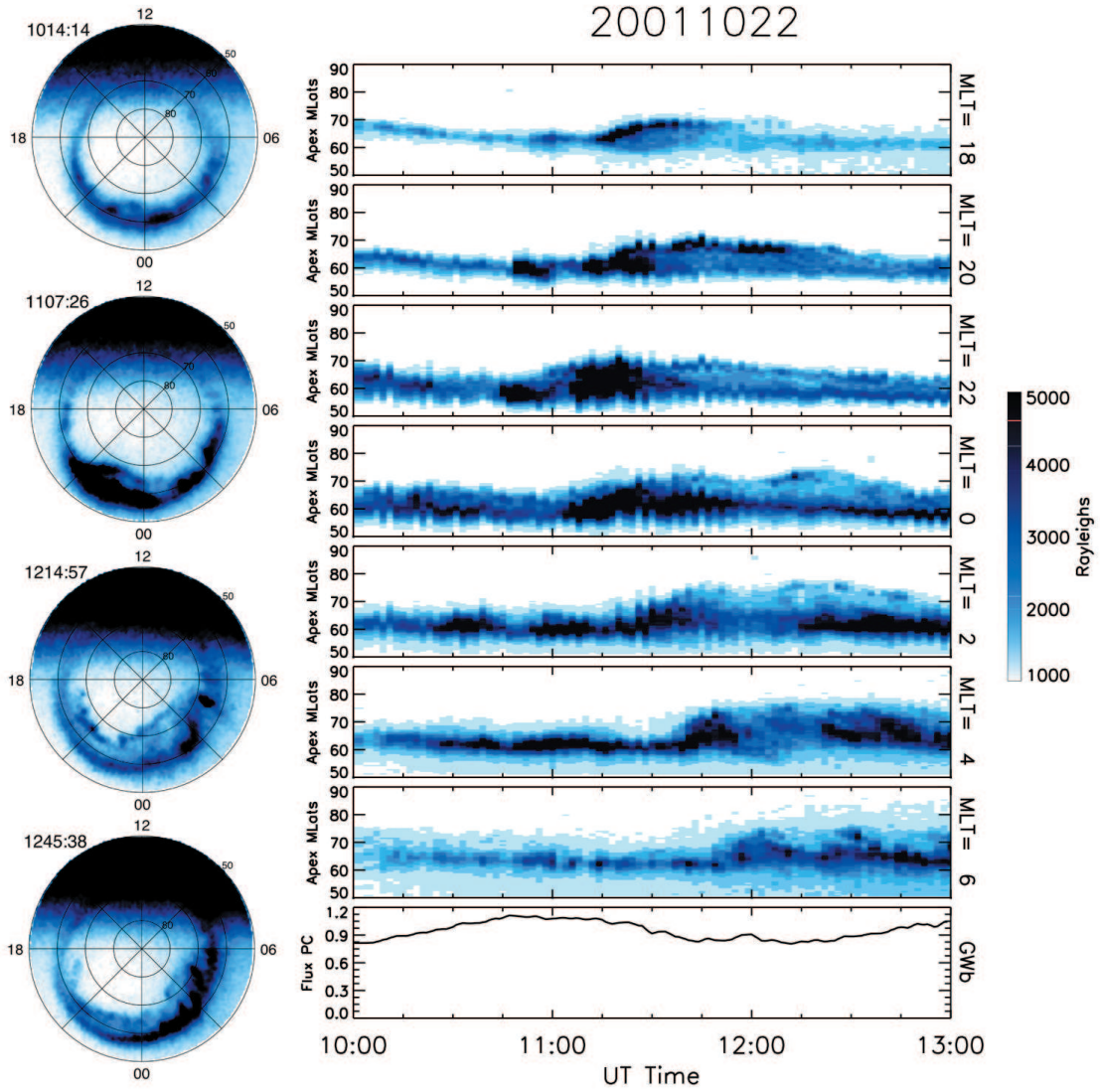

Figure 4.5: A stack plot of keograms for the individual sawtooth at 11:06 on October 22, 2001. The set up is the same as Figure 4.3.

Henderson et al. [2006a] study of the event on April 18th 2002. Also, the sawtooth aurora extends more equatorward than the substorm. The substorm goes no lower than 65 magnetic latitude, whereas the sawtooth extends to 55 magnetic latitude. We found similar intensification patterns and low-latitude boundaries for most of the sawtooth events. This may indicate that sawtooth oscillations may move further into the inner magnetosphere than isolated substorms.

The F_{pc} in Figure 4.5 has the same y-axis scale as Figure 4.2, making it easier to see that the sawtooth stores and releases much more magnetic flux than the isolated substorm. Also, the growth phase or stretching phase is more prevalent as the amount of open flux grows from 0.78 to 1.115 GWb. After the onset, the flux is released just as in the isolated substorm. The minimum amount of F_{pc} is 0.82 GWb which reached approximately 50 minutes after onset. Thus, 0.29 GWb are released from the tail which is 26% of the maximum flux stored during the event. The sawtooth shows somewhat more recovery of the F_{pc} than the isolated substorm, however it is more complex since the recovery phase and the growth phase of the following oscillation, onset of 13:44 UT, develop simultaneously. This is where it becomes difficult to compare isolated substorms and sawtooth oscillations. In the future, it may be better to look at substorms that occur during a magnetic storm. However, these are harder to determine due to the large levels of activity in the data.

The dayside boundary of the sawtooth is plotted on Figure 4.6, which is set up just like Figure 4.3. Unlike the isolated substorm the dayside contributes to the storage of open flux in the magnetosphere for this sawtooth. This represented by the equatorward movement of the boundary during the "growth" phase of the sawtooth. The solar wind/IMF data show that the onset was probably triggered by the northward turning that peaks just before onset. Also the E_{sw} reaches a minimum

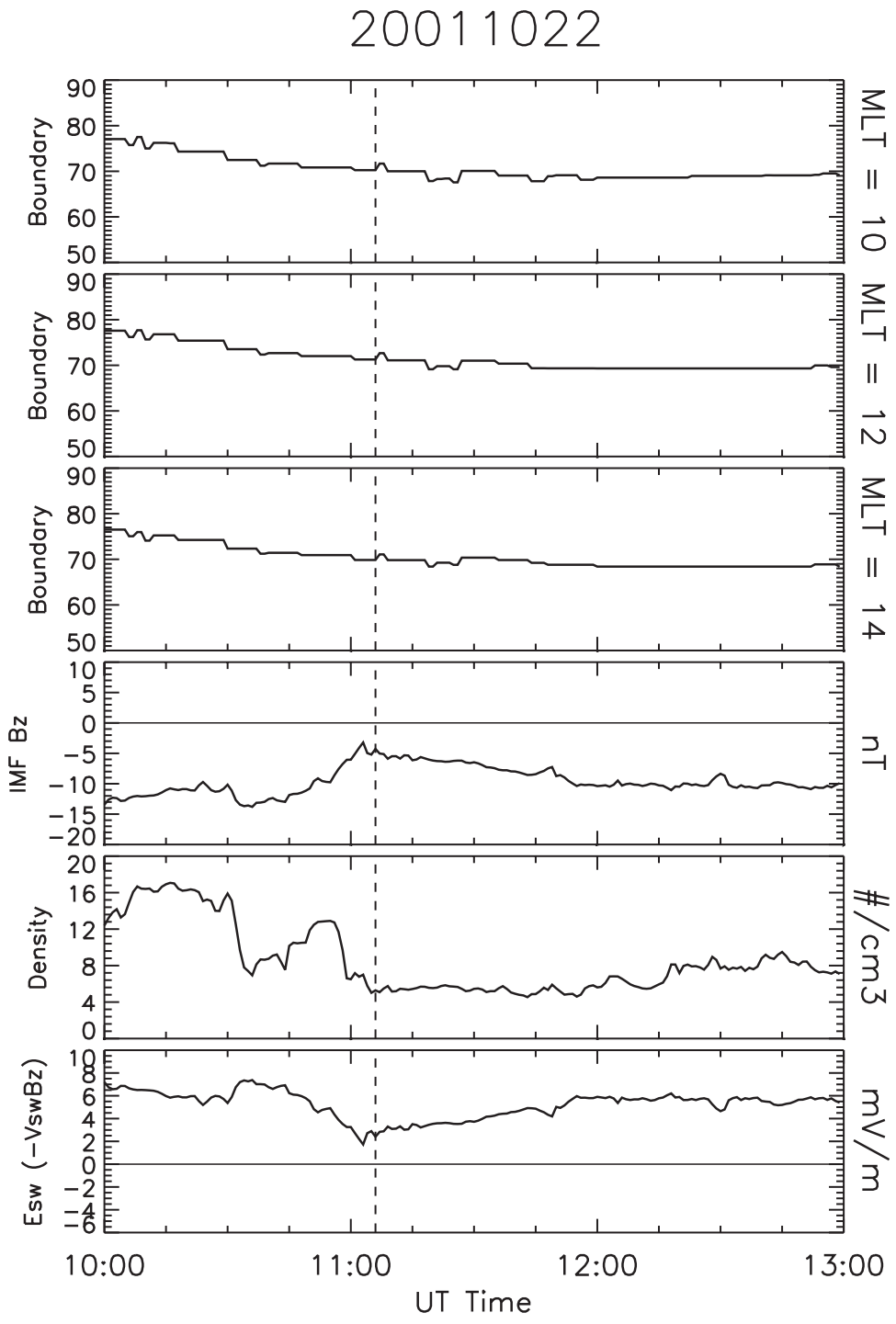

Figure 4.6: A stack plot of the dayside boundaries for the individual sawtooth on October, 22 2001. The set up is the same as Figure 3.4. The vertical line shows the onset of the injection as measured from geosynchronous satellites.

at this point which may have caused a small enough reconnection line on the dayside that nightside responded by reconnecting and triggering the onset.

4.1.3 Steady Magnetospheric Convection Event

For comparison we included steady magnetospheric convection events that appear to have pseudo breakups in the auroral signatures. All SMCs are determined using the methodology set forth in *DeJong and Clauer* [2005], which states that the PC area must be steady for at least 3 hours, AE must be greater than 200 nT, and there are no substorm signatures in other data (AE, AL, LANL SOPA, and magnetometer). Because most SMCs start with a substorm [*DeJong and Clauer*, 2005] and we do not include recovery phases, onset is chosen to be when the PC area becomes steady or at least 1 hour after the initial substorm expansion phase onset. Figure 4.7 shows the first 3 hours of the SMC that occurs on October 26, 2000. Only 3 hours are used in this study since we used 3 hours for the substorm and sawtooth studies. Also, the minimum time requirement for our SMCs is 3 hours.

During SMCs the dayside and nightside reconnection rates should balance [*DeJong and Clauer*, 2005]. If this holds then the aurora and amount of open flux in the magnetosphere should remain fairly steady. This can be seen in Figure 4.7 (same format as Figures 4.2 and 4.5) in that the F_{pc} and the extent of the aurora, both poleward and equatorward, are nearly constant. However, there are fluctuations in the brightness of the aurora. At about 05:15 UT, there appears to be a brightening at 22 MLT which seems to move toward dawn. However, there is no poleward movement in the boundary associated with the brightening, and it only lasts for about 20 minutes. Thus, we consider this to a pseudo breakup not a substorm [*Koshkinen et al.*, 1993; *Fillingim et al.*, 2000]. We see pseudo breakups in many of our SMCs,

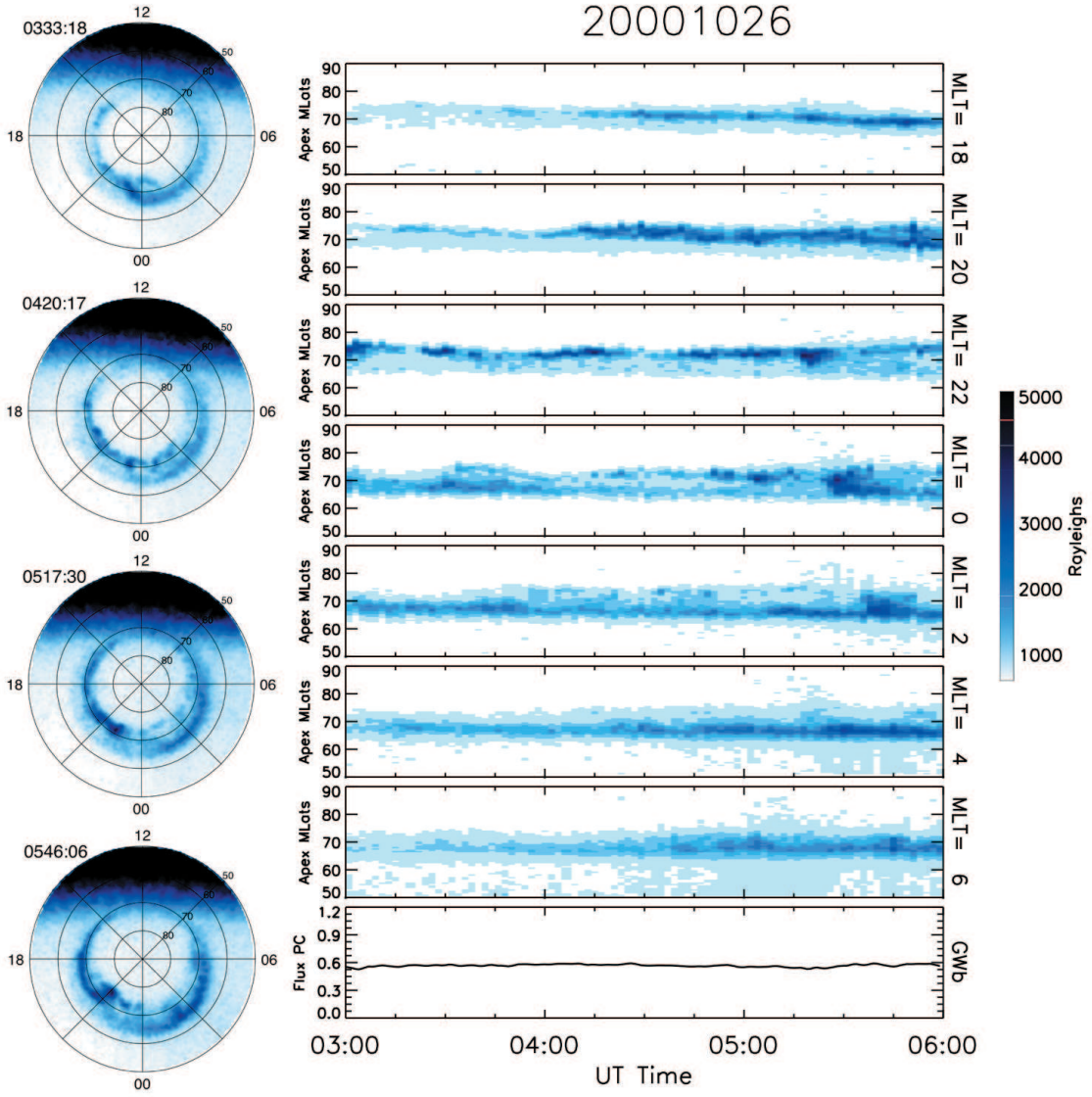

Figure 4.7: A stack plot of keograms for the SMC on October 26, 2000. Set up is the same as Figure 4.3.

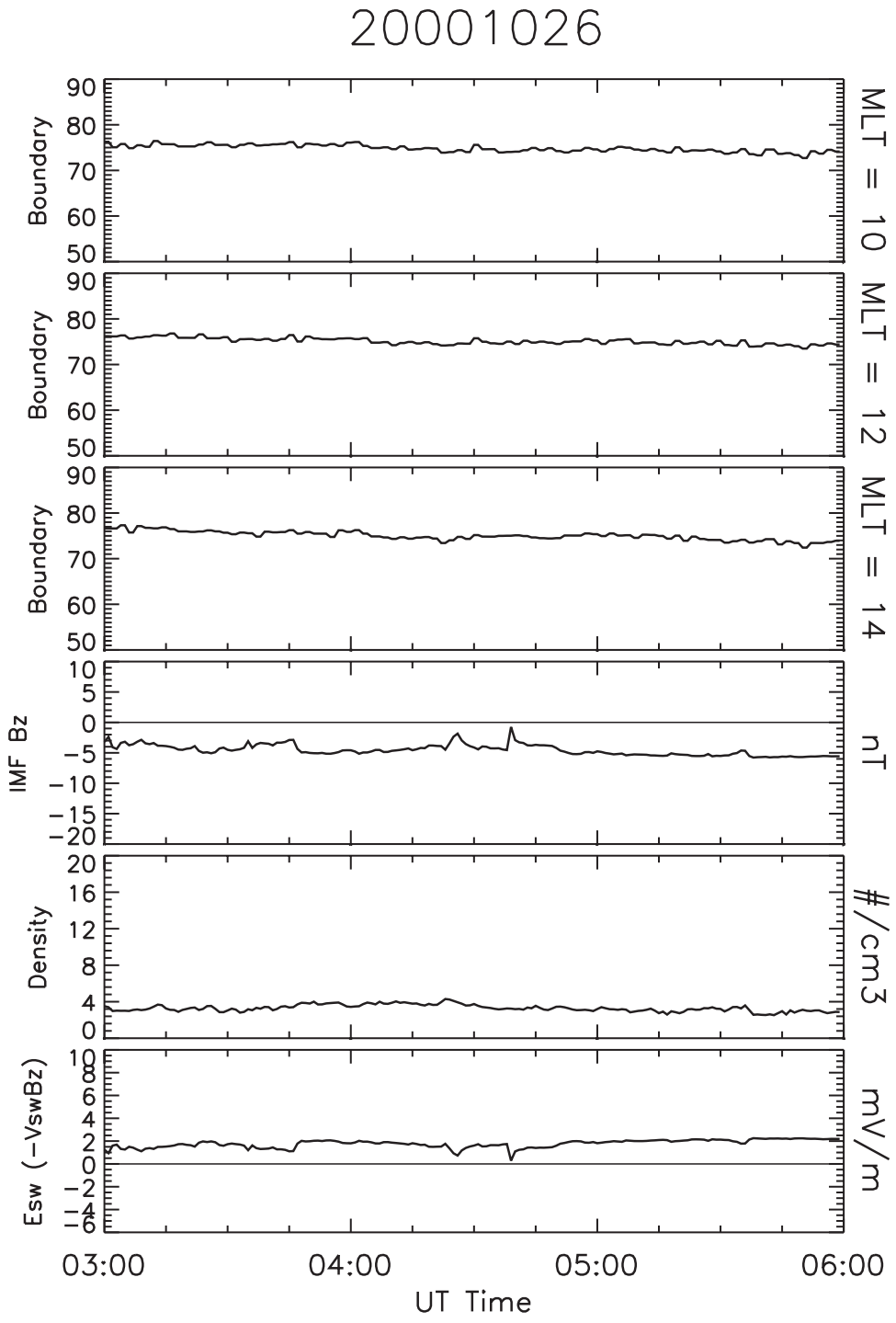

Figure 4.8: A stack plot of the dayside boundaries for the SMC on October, 26 2006. The set up is the same as Figure 4.4

as did *Sergeev et al.* [1996]; *Yahnin et al.* [1994], although they did not call them as such. This indicates that the magnetosphere may be considered steady on a large scale but not as steady on a smaller scale.

The dayside boundary and solar wind/IMF parameters (as seen in Figure 4.8) are what one would expect during an SMC [*O'Brien et al.*, 2002]. The dayside boundary is steady the entire 3 hour interval and IMF B_z, solar wind density and E_{sw} are all moderate yet steady.

4.1.4 Discussion of Case Studies

With respect to the auroral intensity and extent in magnetic latitude (65 mag. lat.) the isolated substorm's expansion phase more closely resembles the SMCs. But this is where the similarities end, during the SMC the dayside and night side merging rates are balanced, this is not the case for the substorm. The F_{pc} trends for the substorm follows the same pattern as the sawtooth. They both have a loading and unloading of the F_{pc} thus both start with a larger dayside reconnection rate which then transitions to a larger night side reconnection rate after onset. Although the F_{pc} variations during the substorm are smaller than during the sawtooth, the amount of flux released from the tail is approximately 0.30 GWb for both. However, if we look at the percentage of the total this represents, then the substorm releases 42% of the stored flux whereas the sawtooth releases only 26%.

4.2 Statistical Study

In order to better characterize the classes of events described above and to determine the amount of open flux variations during the storage (loading) and release (unloading) portions of the the events, we have conducted a statistical investigation of the F_{pc}. In this portion of the study we used 29 individual sawteeth, 31 isolated

substorms, and 45 SMCs (See Appendix for a full lists of events) . As stated previously both IMAGE FUV WIC and Polar UVI LBHl data were used in the analysis for all types of events. The top three plots of Figure 4.9 are superposed epochs of all the F_{pc} for SMCs (green), individual sawteeth (blue), isolated substorms (red), with the averages over plotted in black. The averages are then replotted at the bottom for a better comparison. Substorms and sawteeth events are plotted from exactly 1 hour before onset, so onset of the event is at 60 minutes.

The left plot on Figure 4.9 is a superposed epoch of the actual values of the F_{pc}. As expected, the SMCs are very steady, while the substorms and sawteeth show growth, expansion and recovery phases. It can be seen that the average of sawteeth F_{pc} is much larger than that of isolated substorms. It appears that on average sawtooth oscillations have a F_{pc} that is 150% as large as isolated substorms, yet the patterns of loading and unloading with respect on the onset time (60 minutes) are very similar. In order to study the loading and unloading processes more closesly the fluxes have been normalized and plotted on the right of Figure 4.9. The normalization process was done by dividing by the largest F_{pc} for each event. The SMC patterns are very steady with the smallest F_{pc} at least 80% of the maximum. The isolated substorms and sawteeth reach their maximum F_{pc} close to onset, as expected. They also both have approximately the same temporal evolution. There appears to be slightly more of a growth phase, or storing of flux, before onset and a little more recovery phase after onset during the individual sawteeth. Since most sawtooth injections occur in a series the recovery phase of one and the growth phase of the next must occur simultaneously and we see that superposition of the two effects.

For a more quantitative approach, we looked at the maximum and minimum fluxes of each type event and measured both the amount of change and the rate of

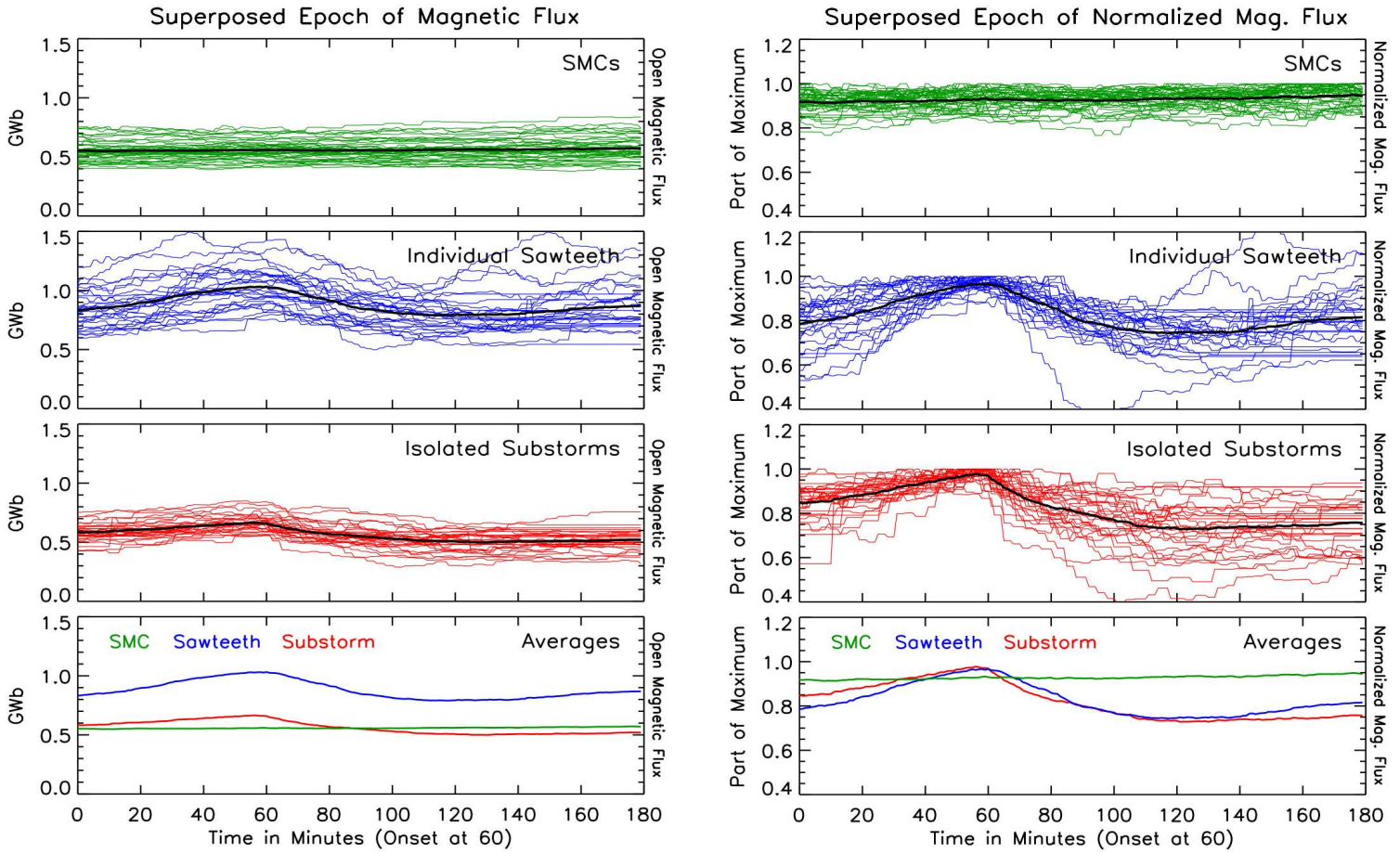

Figure 4.9: Superposed epochs of the polar cap open flux for SMCs, isolated substorms and individual sawteeth. The average of are replotted on the bottom. Left is the actual F_{pc} in gigawebers and right is the F_{pc} normalized by the maximum area for the time interval.

Table 4.1: Average polar cap open magnetic flux statistics for substorms and sawteeth

Open Magnetic Flux in the Polar Cap(Average)

	Substorms	Sawteeth
Maximum (GWb)	0.68	1.07
Minimum (GWb)	0.47	0.74
Decrease (GWb)	0.21	0.33
% Decrease	30.8	30.4
Time for decrease (Hours)	0.91	1.01
Rate of decrease (GWb/hour)	0.23	0.33

Table 4.2: The % of open flux released from the tail after onset for substorms and sawteeth

% of open magnetic flux released (Average)

Minutes after onset	Substorms	Sawteeth
15	12.4	8.8
30	17.2	17.7
45	21.3	22.0
60	24.0	23.1

change. The average released flux for isolated substorms is 0.21 GWb in an average of 54 minutes. For sawteeth there was an average decrease of 0.33 GWb in an average of 60 minutes. Giving the isolated substorms a rate of flux release is 0.0039 GWb /min and sawteeth 0.0055 GWb/min. However, if we look at the percent change from maximum to minimum, both individual sawteeth and isolated substorms drop by 30%. These measurements are listed in greater detail in Table 1.

The second approach uses the onset determined by LANL or magnetometer data. We look at the percent change in F_{pc} for 15, 30, 45, and 60 minutes past the onset. The results are shown in Table 2. As can be seen, there is very little difference between the two types of events. However, one of the problems with the method is the mismatch of onset times with the auroral onset.

For this portion of the study we have left out the dayside boundary examined

in the case studies. This is because for many of the events, especially when using UVI, the dayside boundary is not seen and has to be interpolated. This process is fine for measuring the overall polar cap area and flux but not quite exact enough for an in-depth study. Because the IMF/solar wind parameters can be quite variable for sawtooth events [*Huang et al.*, 2004], there was no real general pattern to be found in the data when placed into a superposed epoch and compared to substorms and SMCs. The only statement that can be made is that the drivers appear to be stronger for sawteeth then substorms or SMCs, thus most likely causing a larger dayside merging rate for sawteeth than substorms. This is consistent with what is described above.

4.3 Discussion

It appears that there are many similarities and differences when comparing these three types of events. The isolated substorms and SMCs studied here are similar in auroral intensity, extent of aurora in magnetic latitude, and amount of open magnetic flux. Whereas the individual sawtooth is larger in most respects than both the substorms and SMCs. Due to the on going debates about sawtooth injections and substorms [*Cai et al.*, 2006a, b; *Henderson et al.*, 2006a] and since we are only looking at one aspect of the events, we cannot yet say if an individual sawtooth is just a large substorm or something completely different. However, we can say that the amount of open magnetic flux released is larger for individual teeth, but the percentage released is the same as that of isolated substorms. It also appears that the auroral oval, during the individual teeth, extends further into the inner magnetosphere than isolated substorms or SMCs, based on the auroral equatorward edge. In order to more fully explore the differences of these events, more data will need to be studied

and more events will need to be investigated in the IMAGE FUV and Polar UVI data.

CHAPTER V

Statistical Study of SMCs, isolated substorms and sawteeth

The question that this chapter will address is "How important are the steadiness and the magnitude of in determining which convection mode the magnetosphere will enter, and what are the implications of the these drivers on the balance or imbalance of reconnection rates?" Thus, this chapter is a statistical analysis that investigates the differences and similarities in the solar wind and IMF drivers for individual sawtooth injections, isolated substorms, and BRIs.

5.1 Data

There are a total of 210 individual sawtooth injections, 212 isolated substorms, and 51 balanced reconnection intervals in this analysis. The data for the isolated substorms and the sawtooth injections is taken from one hour before to one after the onset of the expansion phase or injection. The onset time for the substorm expansions is determined using mid-latitude magnetometer data. The injection time for the individual sawteeth is determined by LANL SOPA proton data. For more information on how these are determined, the reader is referred to *Cai et al.* [2006a]. All BRI time intervals are determined using the methodology set forth in chapter 2,

in which a steady open polar cap magnetic flux is used to identify BRIs. The BRI data spans the entire event interval ranging from 3 to 15 hours. All solar wind, IMF, D_{st}, and AE data are averaged to one minute. The total amount of data used is 327 hours for the BRIs, 420 hours for the sawteeth, and 424 hours for the substorms. All of the events occur between January 1997 and December 2002. Thus, this 6 year interval is used as the background data.

All plots shown in this study are histograms, with the left axis being the percentage of the total number of data points that fall into a bin. The bottom axis is the range of data that is being binned. In each figure the data is of the same type going across the row and each column contains the same convection mode. Thus, the first column is the data for individual sawtooth injections, the second is BRIs , and the last column is isolated substorms. The gray histogram in each plot is 6 years of data (1997-2002), thus it is the same in each convection mode histogram. Plotting the background data allows for a comparison of each convection mode to "average" conditions. At the top of each histogram are arrows that indicate the mean (M) and the peak (P) for the convection mode in black and the 6 years of data in gray. The peak represents the most common data point and the mean is the average of the data. If the data is spread evenly around a peak then the mean and the peak will be the same, for example, the IMF B_z for the background data.

Also on each plot is the p value calculated using the chi-squared test. The chi-squared test compares an expected probability, the background data, to an observed outcome, the convection mode. The p value represent the probability of a more extreme outcome than the one observed, thus if the p value is 0.95 there is a 95% change of getting an outcome that deviates more from the expected value. If a p value is less than 0.05 then it is considered to be statistically significant in its difference

from the expected value. If the p value is large, close to 1, then can be said that observed data is close a random sample of the expected value. So, for our purposes here if the χ^2 p value, printed in the top right of each histogram, is larger than 0.05 then it cannot be said that the data for that convection mode is significantly different from the background data statistically speaking. In order to ease any confusion, if the χ^2 p value appears in black then that data is statistically significant, if it appears in gray it is not.

5.1.1 Histograms

The first part of this study is a statistical analysis of data that occurs during the time frame around onsets of expansion phase of isolated substorms, around the injection time of individual sawteeth, during the entire interval of the BRIs, and during the 6 years in which these events occur. The mean, peak and standard deviation (STD) for each histogram are listed in table 5.1.

The histograms in Figure 5.1 are created using magnetospheric (D_{st}) and ionospheric (Cross polar cap potential, or CPCP, and AL) data calculated by AMIE. The D_{st}, plotted in the first row, represents the storm time activity during these events. Not only do the individual sawteeth injections occur during stronger storms, more negative D_{st}, they also have a larger range of D_{st} over which they occur. This large range can be noted visually in the histogram, and numerically by the large standard deviation of the histogram. BRIs and substorms peak very close to each other and have a similar structure in the histogram. However, the tail on the BRI histogram reaches only -100 nT while the isolated substorm histogram tail goes to -150 nT.

The CPCP and AL are both indications of the activity in the ionosphere's auroral zone. As expected, the auroral zone is the most active during sawtooth injections.

The range of potentials and AL are also the greatest for the individual sawteeth. The CPCP for the BRIs and substorms are very similar, but the BRIs' CPCP has a much smaller range. The AL for the BRIs has a larger peak at a lesser value when compared to the substorms. Once again the BRIs have the smallest AL data range with very few data points below -600 nT.

The rest of the figures for this section are histograms of solar wind/IMF parameters during the various convection modes. The histograms along the top row of Figure 5.2 show that the IMF B_z is larger in magnitude during sawtooth injections than during substorms and BRIs. The sawteeth injections also have a wide range of B_z over which they can occur. The histograms of the IMF B_z for the BRIs and substorms have a similar shape and peak, yet they both differ from the background data. The temperatures during the the sawtooth injections peak at a very low of 0.10 x 10^5 K and have a long thick tail. This indicates that even though a low temperature is the most common for sawtooth injections, they also occur during high temperatures. The solar wind temperatures for the BRIs peak at a similar value to the background data. However, there are very few data points above 2 x 10^5 K. Thus, BRIs do not tend to occur when the solar wind temperature is high. The isolated substorms occur when the solar wind temperature is statistically the same as background levels. The densities histograms for all three convection modes are not statistically significant in their differences from the background data.

The top row of histograms in Figure 5.3 consists of the solar wind total velocity (V_T) drivers for each convection mode. The first peak in the sawtooth data occurs at approximately 400 km/s and the second one at approximately 600 km/s. The substorm V_T also peaks at about 400 km/s and has a large large tail that reaches approximately 650 km/s. The BRI V_T peaks close to the same velocity as the back-

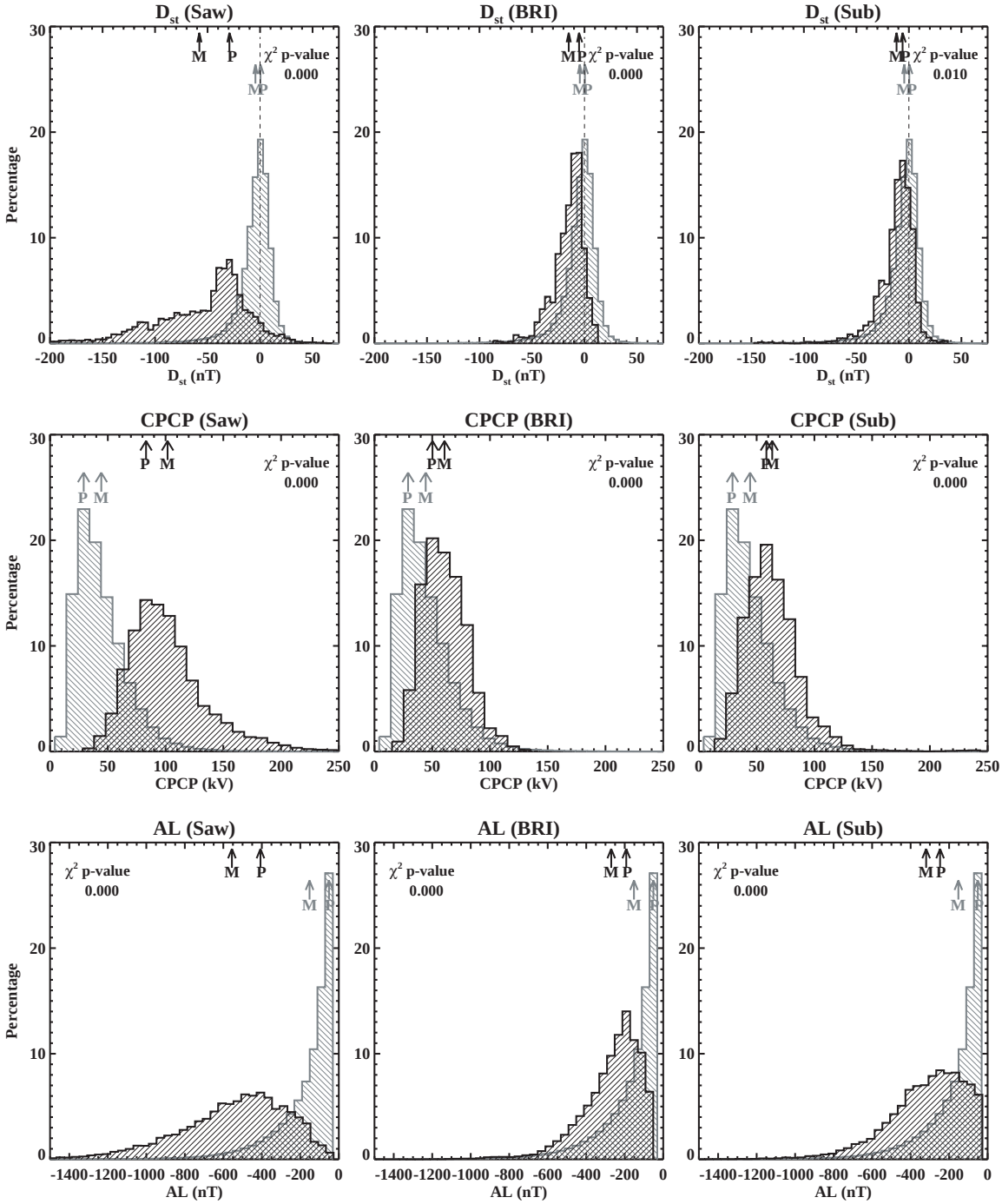

Figure 5.1: Histograms of D_{st}, CPCP, and AL (all determined by AMIE) for individual sawtooth injections, BRIs and substorms. The data for the individual sawteeth injections and isolated substorms is taken 1 hour before to 1 hour after the injection or onset. The gray histogram in the back of each plot is all the data for the 6 years in which the events occur (1997-2002). The M is the mean of the histogram and the P is the peak of the histogram.

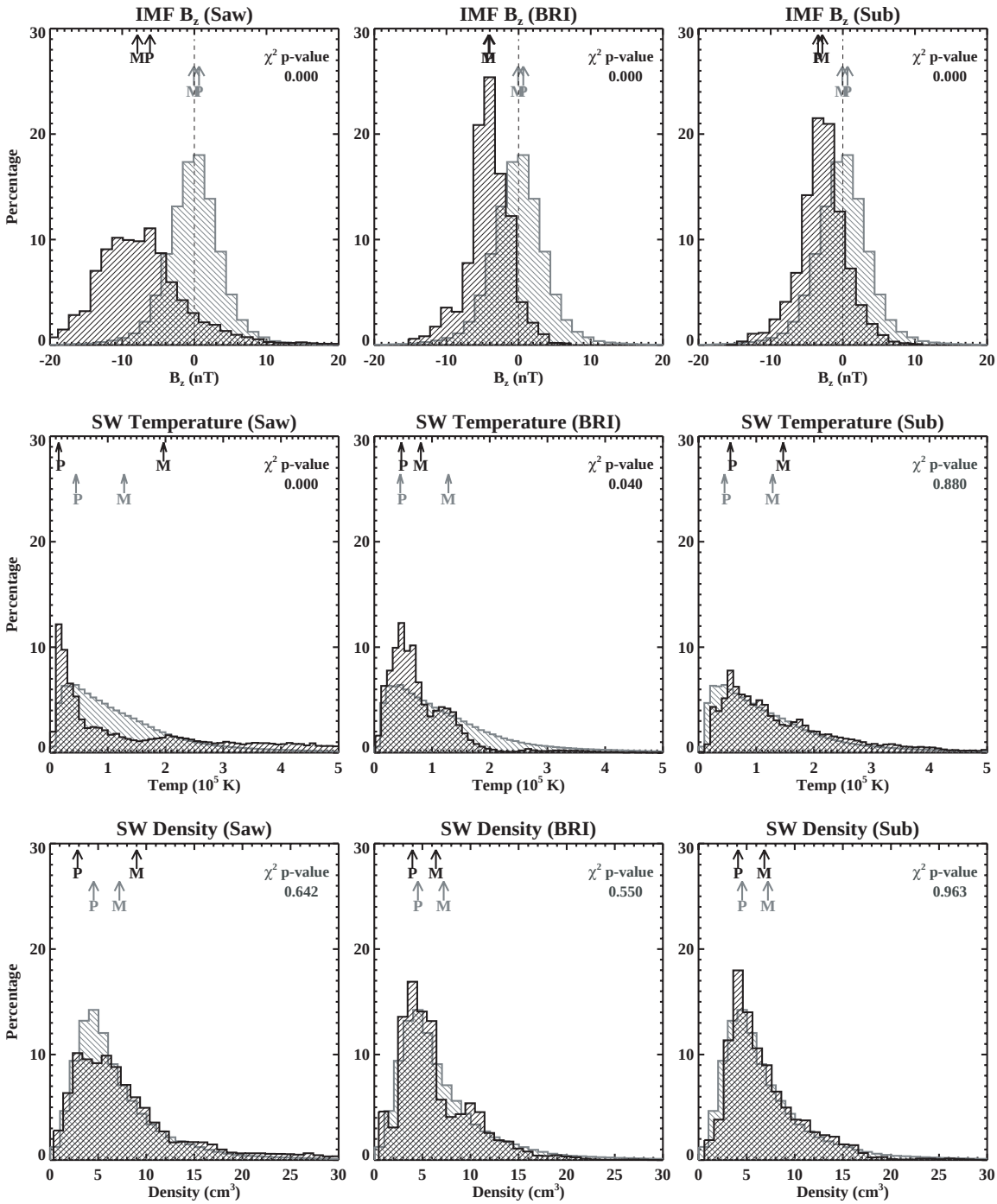

Figure 5.2: Histograms of IMF B_z, solar wind Temperature, and solar wind number density for individual sawtooth injections, BRIs and substorms. The configuration is the same as Figure 5.1.

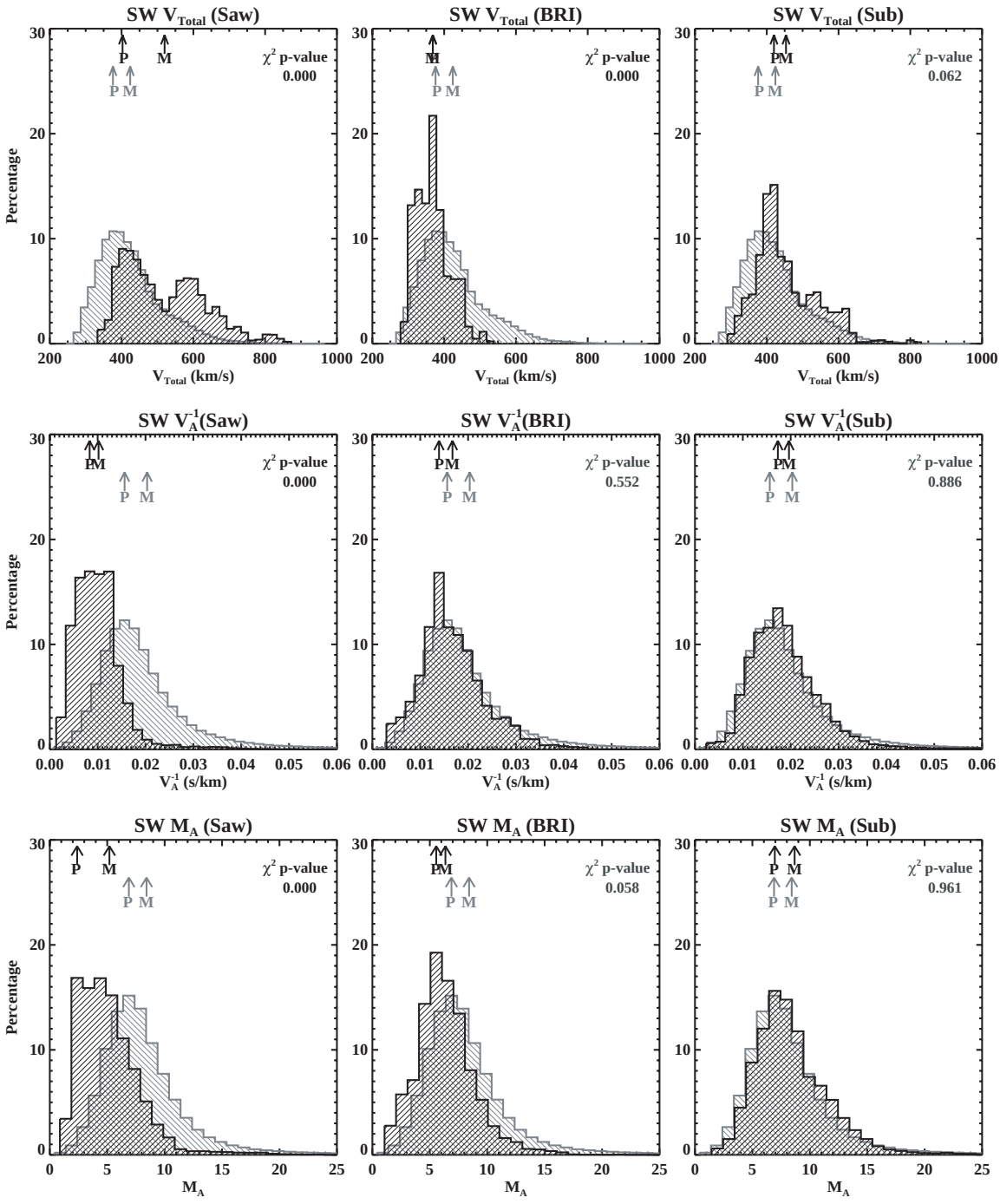

Figure 5.3: Histograms of the solar wind total velocity, SW inverse Aflven velocity and the Alfvenic Mach number for individual sawtooth injections, BRIs and substorms. The configuration is the same a figures 5.1 and 5.2.

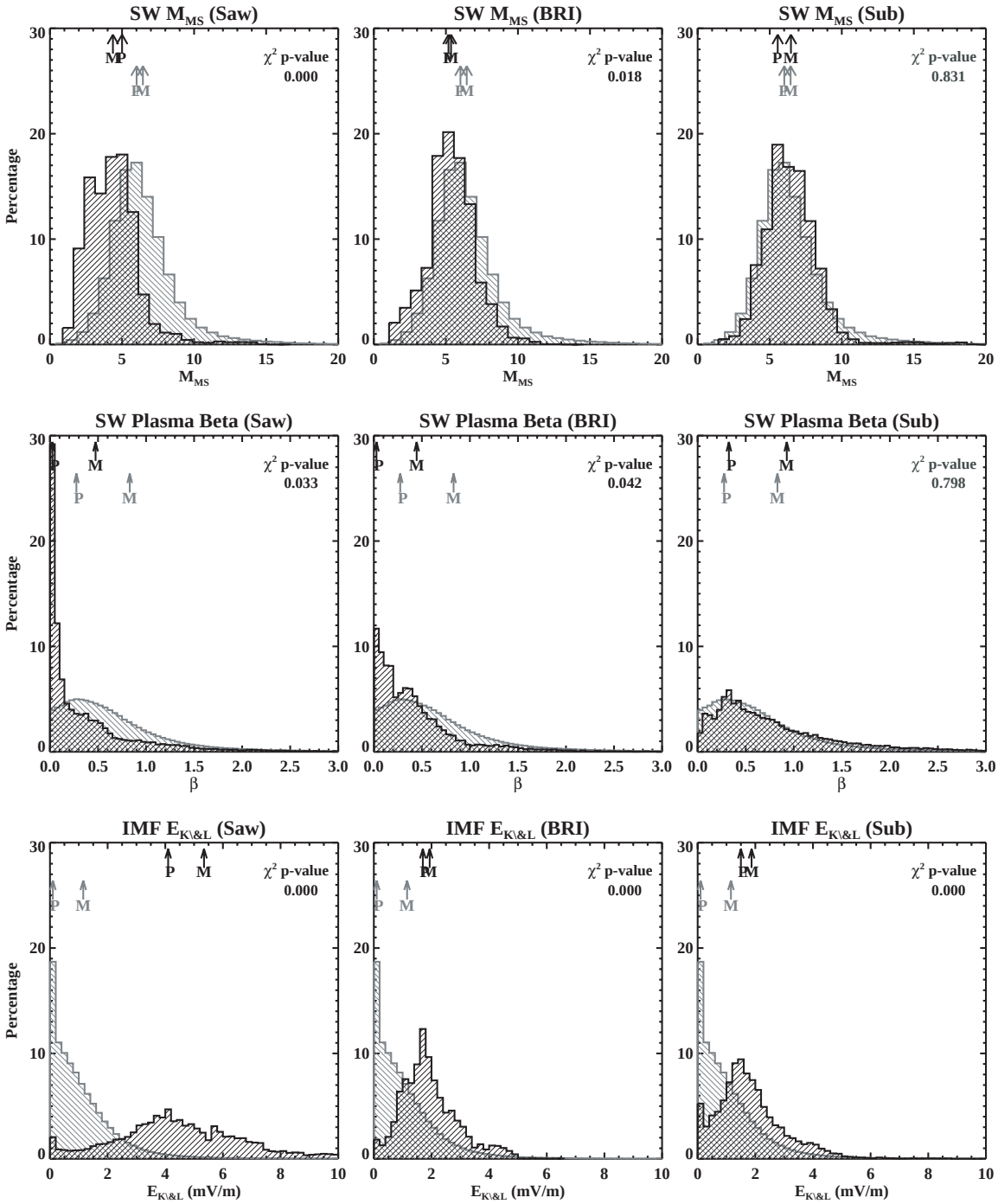

Figure 5.4: Histograms of solar wind magnetosonic mach number, solar wind plasma beta, β, and the Kan and Lee electric field for individual sawtooth injections, BRIs and substorms. The configuration is the same a Figures 5.1, 5.2, and 5.3

Table 5.1: Peak, Mean and standard deviation for the histograms in Figures 5.1, 5.2, 5.3, and 5.4

	Sawtooth			BRI			Substorm			Background		
Measurement	Mean	Peak	STD	Mean	Peak	STD	Mean	Peak	STD	Mean	Peak	STD
D_{st} (nT)	-57.8	-31.2	52.1	-15.0	-7.1	14.8	-11.7	-8.0	17.9	-4.4	-1.6	19.9
CPCP (kV)	101.7	78.1	34.6	60.6	45.2	18.8	63.5	53.5	24.9	44.4	24.1	108.1
AL (nT)	-555	-427	296	-270	-212	161	-319	-267	209	-152	-71	163
IMF B_z (nT)	-7.8	-6.9	7.1	-4.2	-4.7	3.0	-2.8	-4.2	3.4	-0.06	-0.10	4.04
SW Temp (10^5 K)	1.96	0.10	2.11	0.81	0.42	0.62	1.47	0.50	1.10	1.21	0.40	1.08
SW n (cm^{-3})	9.0	2.4	8.6	6.4	3.5	4.1	6.8	3.6	4.1	7.2	4.1	5.9
SW V_T (km/s)	519.8	392.8	112.5	368.3	358.4	46.4	453.6	410.0	86.8	424.1	366.0	89.3
SW V_A^{-1} (10^{-3}s/km)	10.2	7.3	6.0	16.7	12.9	7.0	19.6	16.3	11.3	20.3	14.6	15.0
SW M_A	5.19	1.88	3.08	6.36	5.06	2.57	8.68	6.45	4.39	8.42	6.38	5.41
SW M_{MS}	16.55	7.28	27.04	13.76	9.13	5.35	11.99	9.48	5.11	12.92	9.38	11.34
SW β	0.47	0.0	2.82	0.45	0.0	0.53	0.93	0.32	1.78	0.83	0.25	4.97
$E_{K\&L}$ (mV/m)	5.34	4.00	3.57	1.94	1.60	0.98	1.87	1.40	1.32	1.15	0.0	1.31

ground data, but the peak is much larger at 22 % verses the 11 % for the background. Also the V_T for the BRIs has a very small range relative to the background data and the data for the other convection modes. The V_T rarely goes above 450 km/s during a BRI.

The inverse of the Alfven velocity (V_A^{-1}) histograms are plotted in the second row of Figure 5.3. The V_A^{-1} during both BRIs and isolated substorms is statistically comparable to the background data. The sawteeth have a high V_A, causing the V_A^{-1} to be low. The V_A^{-1} for the sawteeth injections has a very tight range. There are few data points above 0.02 s/km. The third row of Figure 5.3 contains histograms of the Alfvenic Mach number ($M_A = V_T/V_A$). Thus, it is a combination of rows 1 and 2. As discussed above, the sawteeth occur during large solar wind V_T and large V_A, yet the Alfvenic Mach number is low compared to the background data. This indicates that the V_A dominates the M_A during sawtooth injections. The BRIs also occur during a lower Alfvenic Mach number than the background, but in this case the low solar wind V_T determines the Alfvenic Mach number. The substorms tend to occur when Alfvenic mach number the same as average values.

The final figure for this part of the analysis, Figure 5.4, consists of the solar wind fast magnetosonic Mach number ($M_{MS}^2 = V_T^2/(V_S^2 + V_A^2)$), solar wind plasma beta, and the Kan and Lee electric field ($E_{K\&L}$) [*Kan and Lee*, 1979]. During substorms, the magnetosonic mach number is comparable to the average solar wind values. While the histogram of the M_{MS} looks the similar to the background data, it is shifted to a lower value that makes it statistically significant. During individual sawteeth injection, the M_{MS} peaks at a lower value than the background data. The shape of M_{MS} histogram for all three convection modes is similar to the M_A histograms.

Along the second row of Figure 5.4 are the histograms for the solar wind plasma

Beta (β), which is the ratio of plasma pressure to the magnetic pressure. The β is a combination of the solar wind density, temperature, and IMF B_T. During sawtooth injections the solar wind β tends to be much less than the background data. The histogram for the the sawtooth β drops off quickly but has a long tail. This indicates that, while the β in the solar wind is usually small during sawtooth injections, they can also occur when the solar wind β is large, similar to the temperature. The solar wind β for the BRIs also has a vary low peak, but this peak only reaches 12% as opposed to 29% for the sawtooth injections. Furthermore, the β histogram does not drop off as sharply during the BRIs and the data also has secondary peak near 0.4. The solar wind β for the substorms is statistically comparable to the background data. The differences in the solar wind beta histograms indicate that it may play a role in the which type of event occurs in the magnetosphere.

The last solar wind parameter evaluated is the Kan and Lee electric field ($E_{K\&L}$) where

$$E_{K\&L} = V_x B_{zy} \sin^2(\theta/2) \tag{5.1}$$

and V_x is the solar wind velocity in the x-direction, B_{zy} is IMF in z-y plane and θ is the angle between B_y and B_z. If it is assumed that V_x dominates the V_T and B_z dominates B_{zy} then $E_{K\&L}$ becomes a combination of the first row in Figures 5.2 and 5.3. Because the $E_{K\&L}$ is related to the IMF merging efficiency, it is the geoeffective electric field. Thus, it should be higher during stronger events and lower during weaker events. This is what occurs in the histograms. The $E_{K\&L}$ has a large magnitude and spread during the sawtooth injections, while the BRIs and substorms are very similar to each other.

In summary:

- D_{st} is the most negative and has the largest range during the individual saw-

tooth injections.

- CPCP is the largest during the sawteeth, while the BRIs and substorms have comparable CPCP.
- AL is the largest for sawteeth and the smallest during BRIs.
- Solar wind densities differences during each convection mode are statistically insignificant. During BRIs the V_A is comparable to the background data. The isolated substorm drivers, with the exception of IMF B_z, V_T, and $E_{K\&L}$, are statistically comparable to the 6 years of background data.
- IMF B_z and $E_{K\&L}$ are the strongest during sawtooth injections, while the isolated substorm and BRIs are very similar to each other.
- The solar wind temperature and plasma β are the lowest during sawteeth and somewhat lower than average during BRIs.
- The solar wind V_T is bimodal and high during the sawteeth, and low with a small range ($\sim$ 300 - 450 km/s) during the BRIs.
- V_A is large during sawtooth injections, due to the strong magnetic field.
- The solar wind M_A and M_{MS} are the lowest during the individual sawteeth, lower than average during the BRIs, and average during the isolated substorms.

5.1.2 Discussion of Data

The magnetospheric and ionospheric data for the three convection modes indicates that the magnetosphere and the auroral zone are most active during sawtooth events. While substorms and BRIs are very similar in CPCP and D_{st}, the AL is

larger for the isolated substorms. This supports the idea that the westward electrojet should be stable during BRIs. The range in activity levels also varies among the different convection modes. Individual sawteeth injections have a wind range of activity over which they occur. This is indicated by the large standard deviations and the large difference between the peak and the mean of the histograms. By contrast, the BRIs occur over a very small data range. This implies that BRIs occur only during specific activity levels in the magnetosphere. The D_{st} during these events indicates that BRIs do not tend to occur during strong storms (< -100 nT). The sawtooth injections are spread out fairly evenly over the 0 to -150 nT range, while -150 nT is the lowest D_{st} reached during the isolated substorms. This indicates that during strong storms (< -100 nT), the magnetosphere is more likely to enter a sawtooth oscillation mode tha BRI or substorm mode. The CPCP findings are similar to those in *Cai et al.* [2006a], in that the sawteeth have a wider range in the data and the isolated substorms peak at a lower CPCP. While the events used in this study are the same as in *Cai et al.* [2006a, b], the CPCP values are different. This is because *Cai et al.* [2006a] subtracted the background potential that occurs during onset of the event and they also only plotted data for 30 minutes after the onset.

The solar wind/IMF drivers during the isolated substorms are very close to the background data, with the exception of IMF B_z and $E_{K\&L}$. The main reason for the differences in B_z and $E_{K\&L}$ is that substorms almost always occur when the IMF B_z is southward (negative). Thus, the data is biased this way. The background data is spread evenly over the IMF B_z, causing $E_{K\&L}$ to peak at zero due to the θ term. Thus, with the exception of IMF B_z, the solar wind/IMF parameters for isolated substorms are virtually indistinguishable from the background data. This implies that the IMF B_z is the most important component in the solar wind when

determining if a substorm is likely to occur.

During the BRIs, there is more deviation from the average of the solar wind/IMF drivers than during the isolated substorms. However, there are parameters that overlap with the background data, such as solar wind density and Alfven velocity. The IMF B_z and $E_{K\&L}$ during the BRIs differ from the average data, but are similar to the isolated substorm data. This indicates that magnitude of these four drivers may have little impact on the differences of magnetospheric dynamics during these two convection modes. Conversely, the solar wind Temperature, total velocity, Alfvenic mach number, magnetosonic mach number, and plasma Beta differ from the average solar wind data and the substorm data. While the peak of the temperature histogram is the same value as the background data, the histograms have different shapes, during BRIs the temperature in the solar wind tends to be lower than average. Similarly, the solar wind velocity during this mode peaks close the average data, but shifted slightly lower, and has a very small range ($\sim$ 300- 450 km/s). Hence, there appears to be a very specific V_T in which BRIs occur. Since Alfven velocity of the solar wind during BRIs is at values close to background data, the total velocity is the dominate term when calculating the the Alfvenic mach number ($M_A = V_T/V_A$). This causes a shift in the histogram to slightly lower values than the background data. The solar wind plasma beta, $\beta = nkT/2\mu_o B^2$, represent the plasma thermal pressure to magnetic pressure ratio. During BRI events this ratio is almost always lower than 1, and usually less than 0.5. This means that the magnetic pressure is higher than the thermal pressure during these events. Since the IMF B_z and density (Figure 5.2) during BRIs are similar to the values during substorms, it appears that the temperature is dominate term when calculating the BRI beta. This implies that the pressure ratio is due to a low thermal pressure not necessarily

a high magnetic pressure. However, the reason for the different peak heights during individual sawteeth and BRIs is most likely due to the lower B_T of the BRIs.

The individual sawtooth injections occur during the most extreme solar wind/IMF drivers. The only parameter that has values that are insignificant when compared to the background data is the solar wind density. The IMF B_z is stronger during the sawteeth (-8 nT) compared to BRI and substorm data (-3 nT). While the IMF B_z during the BRI and substorm intervals has very few data points less than -10 nT, during the sawtooth intervals it can reach as low as -20 nT. Thus, there is a much larger range of IMF B_z that can occur during sawtooth intervals than during BRIs or isolated substorms. The solar wind temperature during sawtooth intervals is very low (0.10 x 10^5 K) compared to the background data (0.4 x10^5 K). However, there is a long thick tail on the histogram indicating that, even though most events occur during low temperatures, they can also happen when the temperature is high. The total velocity of the solar wind during the individual sawteeth is much higher than the background data. There is a double peak in the histogram, one at $\sim$ 400 km/s and a second at 600 k/ms. It is also interesting to note that there are very few data points below 350 km/s during the sawtooth intervals. Thus, a sawtooth event is most likely associated with high solar wind speeds and low temperatures, as seen during coronal mass ejections (CMEs) [*Borovsky and Denton*, 2006]. The Alfven velocity, plotted as the inverse, is also high during these events, creating a small V_A^{-1}. The Alfvenic Mach number (V_T/V_A) is very low when compared to average solar wind data. Despite there large V_T, the M_A is low due to the large V_A. The solar wind plasma beta is also very low during these events. This is not unexpected after noting a low temperature and high IMF B, since $\beta = nkT/2\mu_o B^2$ and n is comparable to the background. Approximately 50% of the data points for solar wind beta

fall below 0.25, which is the peak of the average solar wind β, during the sawteeth intervals. Thus, the magnetic pressure is much greater than the thermal pressure in the solar wind during the events. Finally, the IMF $E_{K\&L}$ is much larger (4 mV/m) for these events than the other events ($\sim$ 1.5 mV/m). This is not surprising since $E_{K\&L} \propto B \times V$ and both V_T and B are large.

5.2 Steadiness

5.2.1 Histograms

It is not only the magnitude of the solar wind/IMF drivers that can effect the magnetosphere, but the changes in these drivers can also have an impact. Therefor, this portion of the investigation analyzes the steadiness of the parameters during individual sawtooth injections, BRIs, and isolated substorms. The steadiness of each parameter is defined as the standard deviation divided by the mean for a 30 minute interval. The exception to this is being D_{st} for which the steadiness is defined as the slope (nT/min) for a 30 minute period. For each event the steadiness is calculated for a 30 minute period spaced five minutes apart through out the event. For example, if a substorm has an onset time of 02:00 UT, then the over all period used is 01:00 UT to 03:00 UT, the steadiness is calculated from 01:00 to 01:30, then from 01:05 to 01:35 and so on, with the last segment going from 02:30 to 03:00 UT. So, over the two hour period there are 18 measurements of steadiness. The mean, peak, and standard deviation for each steadiness histogram are listed in table 5.2.

Figure 5.5 shows histograms of the magnetospheric and ionospheric parameters during the different convection modes. The first row contains histograms of the slope of the D_{st} over a 30 minute period. A positive slope represent an increase in D_{st} (recovery phase of a storm) and a negative slope is a decrease in D_{st} (storm

main phase). The slope of D_{st} during sawtooth injections has both large positive and large negative values. Conversely, during the BRI intervals the slope of the D_{st} is small. The substorm D_{st} slopes are not statistically significant when compared to the background. The histograms along the second row of Figure 5.5 show the steadiness of the CPCP. The BRIs have the steadiest CPCP with a peak at 0.04 and very little spread. The CPCP for isolated substorms and individual sawteeth are comparable to the background data. The last row consists of the AL steadiness histograms. Once again the BRIs are the most steady with the least spread of data points. The AL steadiness during sawteeth is statistically very close to the background data. While the histograms of the AL steadiness during isolated substorms looks very similar to background plot, the shift to lower values make it statistically significant.

Figure 5.6 is comprised of the steadiness of some solar wind/IMF parameters. The first row of histograms shows the absolute value of the steadiness of B_z. Using the absolute values allows for a better comparison to the background data, since the positive and negative values are binned together. During sawtooth injections and BRIs the IMF B_z is very steady. The substorm statistically the same as the background data. The histograms along the second row of Figure 5.6 plot the steadiness of the solar wind density, which show that during the interval around individual sawtooth injections (1 hour before to 1 hour after), the density in the solar is not as steady as during average times. However, BRI and substorm intervals have solar wind density that is no more or less steady than during the background time. During all convection modes the differences in the steadiness of M_A compared to the background data is statistically insignificant.

Figure 5.7 shows the steadiness for solar wind magnetosonic mach number, β, and the IMF $E_{K\&L}$. The steadiness of M_{MS} for both BRIs and substorms is not

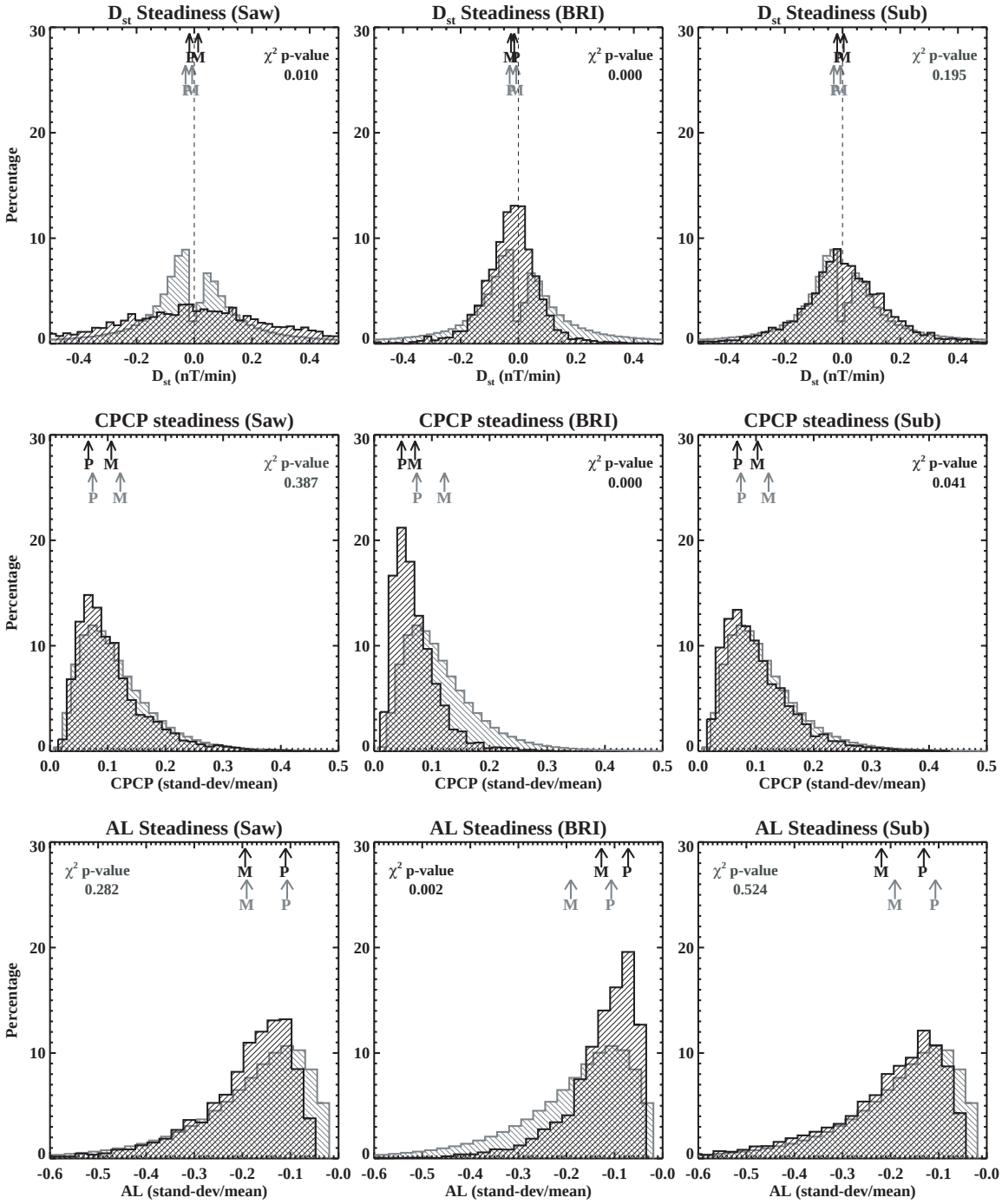

Figure 5.5: Histograms of the steadiness (standard deviation divide by the mean or slope/mean for D_{st}) of D_{st}, CPCP and AL (all calculated using AMIE) for individual sawtooth injections, BRIs and substorms. The data for the individual sawteeth injections and isolated substorms it taken 1 hour before to 1 hour after the injection or onset. The gray histogram in the back of each plot is the all the data for the 5 years in which the events occur (1997-2001). The M is the mean of the histogram and the P is the peak of the histogram.

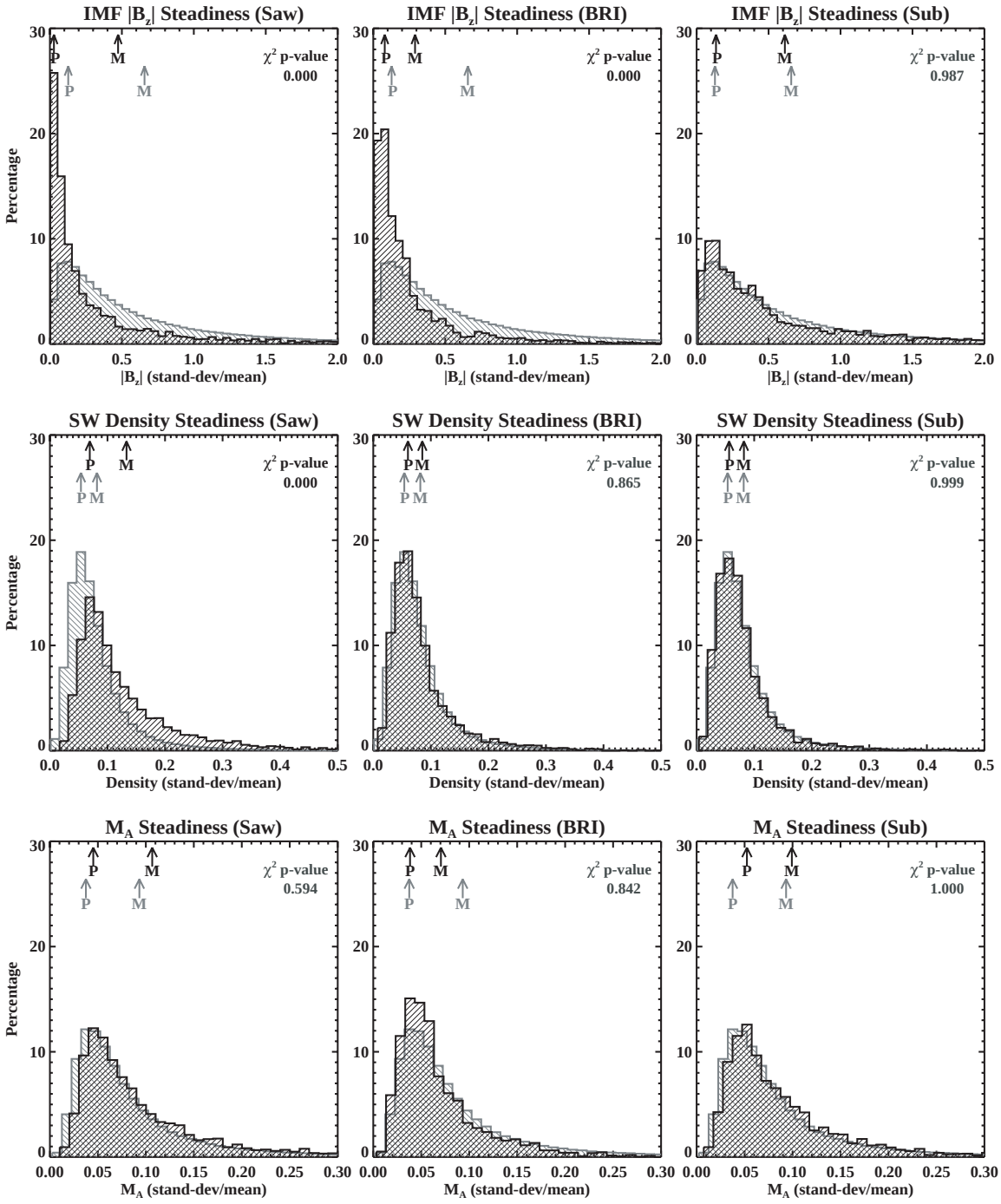

Figure 5.6: Histograms of the steadiness of IMF $|B_z|$, solar wind density and solar wind Alfvenic mach number for sndividual sawtooth injections, BRIs and substorms. The configuration is the same as Figure 5.5.

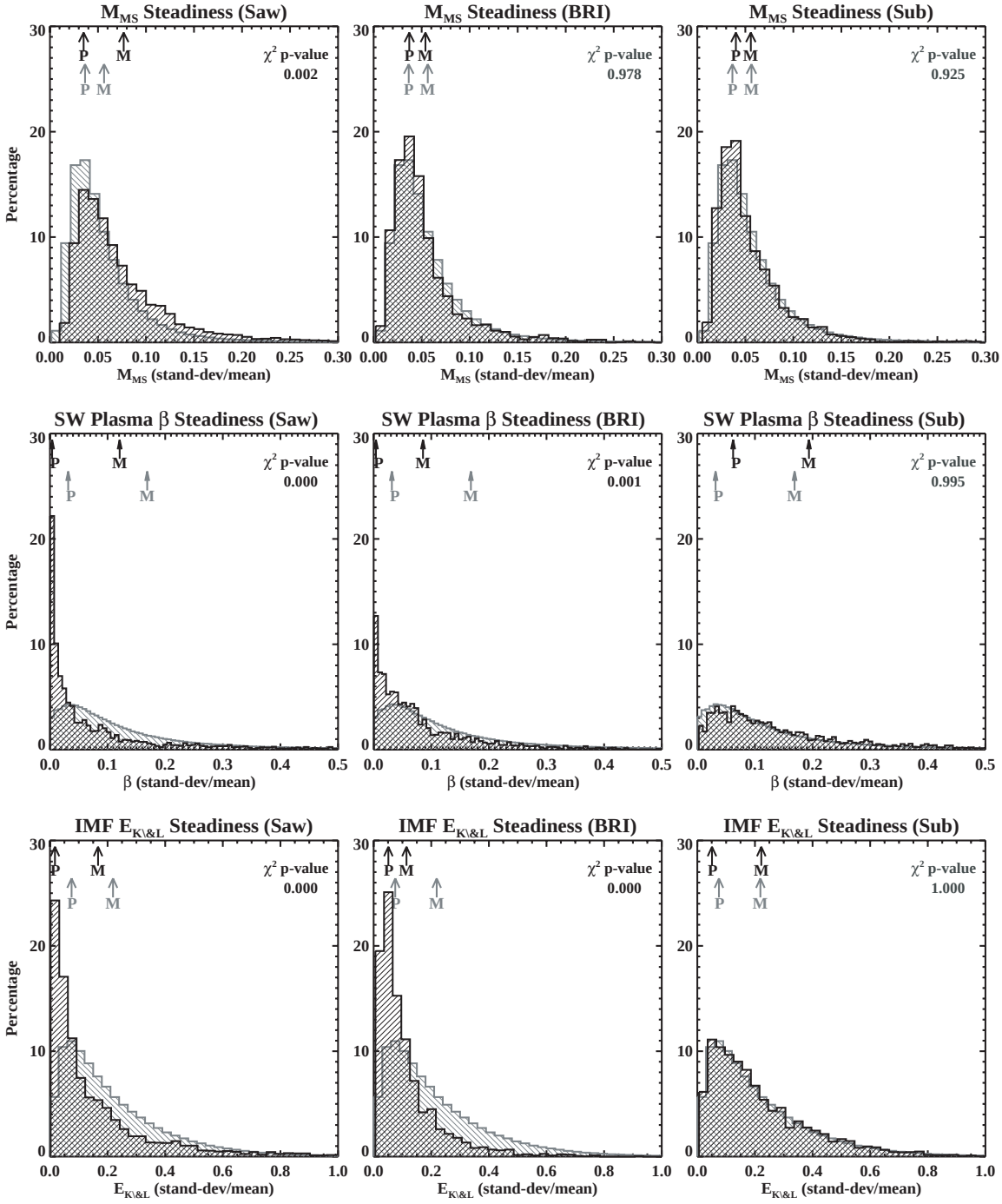

Figure 5.7: Histograms of the steadiness of solar wind magnetosonic mach number, solar wind plasma beta, and the Kan and Lee electric field for Individual sawtooth injections, BRIs and Substorms. The configuration is the same as Figures 5.5 and 5.6.

Table 5.2: Peak, Mean and standard deviation for the histograms in Figures 5.5, 5.6, and 5.7.

	Sawtooth Steadiness (10^{-2})			BRI Steadiness (10^{-2})			Substorm Steadiness (10^{-2})			Background Steadiness (10^{-2})		
	Mean	Peak	STD	Mean	Peak	STD	Mean	Peak	STD	Mean	Peak	STD
D_{st}	1.35	-2.94	49.28	-2.56	-2.69	11.11	0.39	-3.11	18.0	-0.74	-4.27	49.12
CPCP	10.63	5.89	6.17	7.09	3.99	3.96	10.28	5.99	6.02	12.19	6.63	13.30
AL	-19.41	-12.26	10.26	-12.74	-8.42	7.96	-21.90	-14.34	14.55	-19.10	-11.93	14.16
IMF $\mid B_z \mid$	47.38	0.30	95.49	29.03	5.47	44.55	61.32	10.97	76.07	65.75	10.24	74.36
SW V_T	1.27	0.61	0.91	-13.78	-9.15	51.36	-22.06	-9.48	95.19	-0.47	-12.85	96.53
SW n	13.31	6.18	10.20	8.52	5.27	6.31	8.21	4.90	6.26	8.18	4.64	6.17
SW M_A	10.67	4.02	10.97	7.05	3.33	5.32	9.93	4.74	10.56	9.32	3.25	10.26
SW M_{MS}	11.15	3.95	18.8	7.92	3.44	9.10	8.17	2.74	15.26	8.02	3.28	13.94
SW β	12.10	0.02	26.66	8.57	0.05	10.33	19.38	5.86	29.05	17.21	2.82	27.93
$E_{K\&L}$	16.70	0.23	21.84	11.40	3.61	11.34	22.21	3.60	18.42	21.89	6.00	18.47

statistically meaningful when compared to the steadiness of the background data. The sawteeth, however, occur when the M_{MS} is slightly less steady than average. The solar wind β and $E_{K\&L}$ are very steady during BRIs and sawtooth intervals, whereas the substorms occur when the solar wind β and $E_{K\&L}$ are no more or less steady than during average periods.

In summary:

- With the exception of AL, the steadiness of all parameters during the isolated substorms is statistically comparable to the steadiness of the background data.
- The slope of the D_{st} is the greatest (both positive and negative) for the sawteeth and smallest for the BRIs.
- CPCP is more steady for the BRI intervals, than other intervals.
- AL is least steady during the sawteeth and the most steady during the BRIs. While during substorms, the AL steadiness is only slightly higher than the background AL steadiness.
- The IMF B_z is much more steady than the background data, during both sawteeth and BRI intervals. The IMF B_z tends to be more steady during the sawteeth than during the BRIs, but the tail on the histogram indicates that sawteeth can also occur when the IMF B_z is not very steady.
- The steadiness of the solar wind density is statistically comparable to the background steadiness, during both BRIs and isolated substorms. The density is less steady during the individual sawteeth injections than during the background data or the other events.

- Both Mach numbers (M_A and M_{MS}) have a steadiness for substorms and BRIs that is statistically insignificant in their difference from the background data. However, during sawteeth the M_{MS} is significantly shifts to a less steady measurement.

- The solar wind β and $E_{K\&L}$ are both the most steady during the sawtooth intervals and slightly less steady during the BRIs. However, there is a longer tail on the sawtooth histograms indicating that β and $E_{K\&L}$ can also have large variations during these intervals.

5.2.2 Discussion of steadiness

The magnetospheric and ionospheric parameters are as steady or unsteady as anticipated during these events. The large spread of the histograms for the slope of D_{st} during individual sawteeth shows that global sawtooth oscillations tend to occur during storm times. There appears to be no preference for a positive or negative slope, indicating that they occur during both storm time main phases and recovery phases. The BRIs have a very narrow spread around zero for the D_{st} slope, implying that the ring current is more stable during these types of events. The D_{st} may increase or decrease during BRI events but this change is most likely slow. The isolated substorms show no preference for fast or slow changes of the ring current when compared to the background data. This indicates that substorms are just as likely to occur during storm times and non-storm times.

The CPCP and AL are much more steady during BRIs than any other time. The AL index, which is a measure of the westward electrojet in the auroral zone, is much more steady for BRIs than substorms or sawteeth. This is due to the increase in the current traveling westward during the onset of the substorm expansion phase and

the onset of the sawtooth injection. Because there is little or no increase in electrojet during BRIs, the AL remains steady. The tail on the end of the BRI histograms of AL can be attributed to pseudo-breakups during the BRIs, Chapter 3. The CPCP for the sawtooth injections and isolated substorms is comparable to the background data. This most likely occurs because the increase in CPCP during the onset of these two convection modes takes place in less than 30 minutes [*Cai et al.*, 2006a]. Thus, the steadiness calculated in this study does not easily measure this change.

During the isolated substorms used in this investigation, there appears to be no real difference between the steadiness of the solar wind/IMF drivers and the steadiness of the drivers during the background period. Thus, these substorm expansions are most likely triggered by an internal magnetospheric process or a northward turning of the IMF B_z that is to rapid to be detected using this methodology.

The BRI events occur when IMF B_z is very steady. The steadiness in B_z also creates a steadiness in the solar wind plasma β and the $E_{K\&L}$. The other data shown is comparable to the steadiness of the background intervals. This strongly supports to the theory that a steady IMF B_z is an important component of the driving during BRI events.

The time intervals studied for the individual sawtooth injections, 1 hour before and 1 hour after, show that the IMF B_z is very steady during this time, possibly even more steady than during BRIs. However, unlike the BRIs, the density is not very steady during these intervals. These perturbations in the density also create an unsteadiness in the magnetosonic Mach number. The V_T does not play a role in the M_{MS} steadiness because it is a factor of 10 steadier than other parameters shown in this paper. The less steady nature of the density implies that some of the sawtooth injections presented here could have been pressure triggered. A superposed epoch of

the data would elucidate this statement, but is beyond the scope of this paper.

It appears that BRIs and sawtooth oscillations both occur when the IMF B_z driver is steady, creating a steady $E_{K\&L}$ and β, but the changes in solar wind density may be a factor in why the magnetosphere enters a sawtooth mode instead of a BRI mode. Exactly how steady or unsteady the IMF B_z and solar wind density need to be to create these different convection modes is unknown and requires further investigation.

5.3 Discussion of results

5.3.1 Solar wind/IMF drivers

This investigation shows that there are different drivers, both in magnitude and steadiness, for individual sawtooth injections, BRIs, and isolated substorms. The IMF B_z is comparable in magnitude for the BRIs and isolated substorms, and comparable in steadiness for the BRIs and individual sawteeth. Thus, if the IMF B_z is moderate (-4 nT) and not very steady, then a substorm is most likely to occur. If it moderate and steady, then a BRI is most likely to occur. Finally, if it is strong (-10 nT) and steady, a sawtooth oscillation is most probable. Because most of the histograms for the substorms are very similar to the 6 years of background data, it appears that the IMF B_z, and therefore $E_{K\&L}$, is the most important driver during isolated substorms. However, this does not seem to be the case for the BRIs and sawtooth oscillations.

The magnitude of the solar wind velocity and temperature, and their effects on the solar wind Beta, Alfvenic Mach number and $E_{K\&L}$, appear to play a role in the driving of BRIs and sawtooth oscillations. Both the solar wind Beta and Mach numbers (M_A and M_{MS}) are lower than the average data for both the BRI and

sawtooth intervals, where the later events deviate to the lower end of the spectrum. The M_A for the sawteeth appears to be dominated by the large V_A which is dominated by the large magnitude of the IMF B_z. The BRI M_A seems to be influenced mostly by the low V_T. *Lopez et al.* [2004] state that when the M_A is small the compression ratio of the bow shock is low. Causing less solar wind kinetic energy to be converted to magnetic energy in the magnetosheath. However, if the density during this time is high, then the compression ratio increases along with the energy conversion. Thus, both the magnitude and steadiness of the solar wind density most likely play a larger role in the driving of sawtooth oscillations. The histograms show that the density is nominal during sawtooth injections and that it is less stable during these events. This supports the idea that some of the individual teeth maybe triggered by pressure changes in the solar wind [*Huang et al.*, 2005; *Lopez et al.*, 2004].

The solar wind temperature during sawtooth injections is low the majority of the time, but can reach higher temperatures. This along with the low M_{MS} supports the idea that global sawtooth oscillations are most likely to occur during CMEs [*Borovsky and Denton*, 2006]. Whether or not they occur because of the low temperatures and Mach numbers, or if the data is biased this way because they mostly occur during CMEs is not yet known.

5.3.2 Solar wind velocity and its implications on balanced reconnection rates

The low V_T during the BRI intervals is accompanied by a very small range of velocities, indicating BRIs are highly unlikely to occur when the solar wind is fast. The V_T for the sawtooth intervals appears to be bimodal and is larger than the background data. Table 5.3 lists the the percentage of events that have a V_T larger than a certain velocity. It is interesting to note that 50% solar wind velocity data

is greater than 500 km/s during sawteeth, while only 1% of the BRIs data points are greater than 500 km/s. These low solar wind velocities during BRIs agree with *O'Brien et al.* [2002], who found that most BRIs happen when the solar wind velocity is below 450 km/s. Also 35% of the V_T data points during BRIs are less than 350 km/s while very few isolated substorms or sawteeth occur at this slow of a speed.

Due to a similar steadiness in the IMF B_z during both BRIs and individual sawtooth injections, it appears that the solar wind velocity may play a role in whether or not dayside and nightside reconnection rates will balance. To investigate this further we must first look at how the amount of open magnetic flux in the polar cap relates to reconnection rates. *Siscoe and Huang* [1985] state the following formulation of Faraday's Law:

$$\frac{dF_{pc}(t)}{dt} = \Phi_D(t) - \Phi_N(t) \tag{5.2}$$

where F_{pc} is the amount of open flux in the polar cap, Φ_D and Φ_N are the dayside and nightside reconnection rates, respectively. Hence, the temporal evolution of the F_{pc} can indicate a balance or imbalance of reconnection rates [*Siscoe and Huang*, 1985; *Cowley and Lockwood*, 1992]. During BRIs the dayside and nightside reconnection rates are balanced [*Sergeev et al.*, 1996]. In Chapter 4 I investigated the F_{PC} of 41 BRIs and 29 sawtooth injections and found that the F_{PC} is indeed steady during BRIs with an average F_{PC} of 0.6 GWb. While the F_{PC} for the individual sawteeth becomes larger before the injection and lose about 30% of its open flux after the injection. Thus, indicating that the dayside reconnection rate is larger before the injection, and after the injection, the nightside reconnection rate is larger - similar to a substorm.

Table 5.3: The percentage of events that have a solar wind velocity (V_T) greater than 300, 350, 400, 450, 500 and 600 km/s.

	$V_T > 350$ km/s	$V_T > 400$ km/s	$V_T > 450$ km/s	$V_T > 500$ km/s	$V_T > 600$ km/s
Sawtooth injections	99 %	86 %	64 %	50 %	25 %
Isolated Substorms	92 %	73 %	41 %	27%	8 %
BRIs	65 %	21 %	6 %	1 %	0 %
Background data	80 %	54 %	30 %	17 %	5 %

If the formulation for the dayside reconnection rate is [*Holzer et al.*, 1986; *Milan et al.*, 2006]:

$$\Phi_D = \begin{cases} L_{eff} V_{sw} B_z, & B_z < 0 \\ 0, & B_z > 0 \end{cases} \tag{5.3}$$

where L_{eff} is the effective length of the equatorial reconnection line and $V_{sw}B_z = E_y$ is the y-componet of the IMF electric field. If it is assumed that L_{eff} remains steady during the reconnection event [*Milan et al.*, 2007] and that $E_y \simeq E_{K\&L}$, then for both individual sawteeth and BRIs it can be stated that Φ_D remains steady. This strongly indicates that the solar wind velocity plays a large role in the balance of reconnection rates. An example of an event where this occurs is the February 17, 1998 BRI event. During the 5 hour event the V_x averages -394 $\pm$5.8 km/s and the IMF B_z is -8.24 $\pm$ 1.15 nT. While the V_x is close to other BRI velocities, the IMF B_z is more of what is expected for sawtooth injections. So, the magnetosphere enters a BRI mode instead of a sawtooth mode, most likely due to the lower V_x. This event and the statistical data presented here support the idea that if Φ_D is steady and the solar wind velocity is low ($\leq\sim$450 km/s), then magnetosphere can reach a steady state. If the solar wind velocity is large, then internal processes in the magnetosphere do not allow the reconnection rates to balance, periodically loading and unloading the tail. What exactly these internal magnetospheric processes are and how they are controlled by the solar wind velocity is as yet unknown. A detailed study of the inner magnetosphere and tail lobes during these two convection modes might help identify these processes.

Others have also studied the importance of the solar wind velocity on the steadiness of the magnetosphere. Using the Lyon-Fedder-Mobary (LFM) model, *Pulkkinen*

et al. [2007] found that the driving of the magnetosphere is not only dependent on the driving electric field but also depends on its constituents. They state that, under relatively steady driving conditions, higher solar wind speeds lead to a more dynamic magnetosphere. Our statistical data supports these statements, in that the steadiness of our B_z is comparable for the sawteeth and substorms, yet the V_T is much larger for sawtooth injections. It also appears that if the V_T becomes too large than magnetosphere can not stay stable and steady magnetospheric convection will not occur.

5.4 Conclusion

With the exception of IMF Bz, and therefor $E_{K\&L}$, isolated substorms have drivers that are comparable with average solar wind and IMF data in both steadiness and magnitude. This supports the idea of internal magnetospheric processes dominating substorms [*McPherron et al.*, 1986].

It also appears that BRIs are very particular about their solar wind drivers. The ranges on the data for these events is much lower than during either isolated substorms or individual sawteeth. Thus, it appears that when the dayside reconnection rate is stable the nightside reconnection rate is more likely to be able to match it when the solar wind is below $\sim$ 450 km/s. This indicates that there is an internal mechanism in the magnetosphere that will allow for this balance only when the velocity is low. Whether it is the velocity, $E_{K\&L}$ or the magnitude of the dayside reconnection that is the most important is unknown at this time and needs further investigation.

Unlike BRIs, sawtooth oscillations can occur over a wide range of drivers and activity levels. The most predominate drivers appear to be a strong steady IMF B_Z,

low solar wind temperature, high solar wind V_T, and low solar wind Mach numbers. All of these parameters are found during coronal mass ejections (CMEs). It may be difficult therefor to determine which drivers are most important and which drivers are exist because sawtooth oscillations occur mostly during CMEs.

The situation of driving these different types of events is not as simple as, moderate driving creates a substorm, moderate steady driving creates a BRI and strong steady driving creates a global sawtooth oscillation. It appears that magnitude of the solar wind velocity along with magnitude and steadiness of the IMF B_z are the most import factors in determining what type of mode the magnetosphere will enter. However, other drivers, such as steadiness of the solar wind density and magnitude of the Mach numbers could also play a role in sawtooth oscillations.

CHAPTER VI

Discussion

6.1 Review of Results

The first part of this thesis poses to rename steady magnetospheric convection (SMC) to Balanced reconnection intervals (BRI). This new name allows for a more precise and physical description of this mode of convection, eliminating confusion over the term "steady". The hope is that a new name will change the fields perception of these events and allow for a better understand how convection can be steady. This part of the dissertation also focus on answering the first question listed in Chapter 1 section 5: *"How diverse are BRIs and how do the reconnection rates begin to balance and become unbalanced?"*

In order to explore balanced reconnection better, four BRIs are investigated in Chapter 3. In three of the events, steady convection is initiated after a substorm expansion phase. One of the events, however, starts as the magnetosphere slowly builds up activity. Thus, as the dayside reconnection rates increases, the nightside reconnection increases along with it. This part of the thesis alludes to the idea of preconditioning in the magnetosphere before a BRI can occur. Since most BRIs are preceded by a substorm, it appears that the configuration of the magnetosphere during the recovery phase of a substorm might be the most common form of precon-

ditioning for a BRI. However, since one event is not proceeded by a substorm, it does not appear that a substorm is a necessity in order to precondition the magnetosphere for an BRI.

There are three ways the reconnection rates became unbalanced. Two events become unbalanced when the expansion phase of the concluding substorm initiates. Thus, the nighside reconnection rate stays balanced with the dayside, until a new reconnection line forms without loading of the tail lobes. One event ends with loading of the tail lobes in the growth of a concluding substorm. There is also an event that does not have a concluding substorm. The magnetosphere slowly returns to quiet levels as the IMF B_z slowly turns northward.

This chapter also shows the large diversity of the activity levels in the magnetosphere that can occur during BRIs. While the Feb. 3-4 1998 event is active the, activity level is fairly low. The event on February 17, 1998 shows much more mesoscale activity, such as perturbations in the LANL SOPA data, AL, and CPCP. The Dec. 22-23, 2000 event while less active than the Feb. 17 event, is still active and has a pseudo-breakup during the event. This different activity levels imply that reconnection can balance during more activity periods while the magnetosphere maybe less "steady" than needed for an SMC. Thus, the new name BRI allows a larger range of activity levels and more diverse events can be included in this classification.

Along with the focus on BRIs and their new name, this thesis compares the three main modes of convection in the magnetosphere: (1) BRIs, (2) isolated substorms, and (3) sawtooth injections. First, the changes in the open magnetic flux are compared in order to answer the second question in Chapter 1: *"What are the similarities and differences of the F_{pc} and therefor the convection during different convection modes?"*

Chapter 4 studies the balance and unbalance of reconnection rates through the changes in the amount of open magnetic flux in the polar cap (F_{pc}). While it cannot be assumed that all of the flux released during the unloading process comes from the magnetotail lobes, the change in F_{pc} can be used a proxy for the tail unloading. It is found that, on average, both isolated substorms and individual sawteeth release approximately 30% of the stored flux during unloading. However, the individual sawtooth injections store about 150% of the amount of open flux as the isolated substorms. The time from the maximum F_{pc} to the minimum F_{pc} is approximately 1 hour for both events. Thus, the unloading process for sawteeth is stronger and faster than during isolated substorms. While the process of unloading F_{pc} is similar for the sawteeth and isolated substorms, the magnitude of the F_{pc} is comparable for the isolated substorms and BRIs. This indicates that the driving (IMF B_Z and $E_{K\&L}$) for these two events should be close, and according Chapter 5, they are.

Finally, the solar wind and IMF drivers are compared for the three different convection modes. A large statistical analysis is performed in order to address the remaining question from Chapter 1: *" How important are the steadiness and the magnitude of the solar wind/IMF drivers in determining which convection mode the magnetosphere will enter and what are the implications of the these drivers on the balance or imbalance of reconnection rates?"*

The final study investigate the solar wind/IMF drivers that allow the reconnection balance or not balance. While global sawtooth oscillations and BRIs are similar in their steadiness of the IMF B_z and $E_{K\&L}$, but their V_Ts are very different. While most of the sawteeth occur when the V_T above 400 km/s, most of the BRIs occur when is below 400 km/s. Thus, it appears that when the dayside reconnection rate is stable, the nightside reconnection rate is more likely to match it when the solar wind is below

$\sim$ 450 km/s. This indicates that an internal mechanism in the magnetosphere allows for this balance only when the velocity, and therefore the $E_{K\&L}$, is low. Whether it is the velocity, $E_{K\&L}$, or the magnitude of the dayside reconnection that is the most important remains unknown at this time and needs further investigation. The statistic also support the concept that isolated substorms occur during "average" solar wind conditions as long as the IMF B_z is negative.

Chapter 4 and 5 also support the idea that global sawtooth oscillations occur during more active times. They also show that substorms and SMCs both have approximately the same magnitude in activity level, but they differ in the stability of their drivers.

6.2 Future Work

Currently, IMAGE FUV and Polar UVI data are used to determine if an event is an SMC. While this the best way to measure a balance of reconnection rates it cannot be used for events after 2006. This is because the Polar and IMAGE satellites are no longer in service and there is no current missions on the books to replace them. Thus, a new identification method is needed. By using the SMC event list from this thesis a new steadiness parameter could be calculated. It would most likely be something similar to *O'Brien et al.* [2002] but with consideration of the activity level included.

There is still much work that needs to be done before we can truly understand how and why reconnection rates balance. Once more events are found using the steadiness parameter, Cluster and Geotail satellite data could be used for a more in-depth analysis of the magnetotail lobes and plasma sheet. The inner magnetosphere should also be included to help determine the magnetospheric configuration during

these events. The configuration of the magnetosphere during these event may lead to a better understanding of the preconditioning needed for these events.

Finally, modeling efforts should be included. This would allow for study of the different solar wind and IMF drivers. With the ability to control which driver is altered, the importance of the magnitude and steadiness of each driver can be analyzed.

APPENDICES

APPENDIX A

List of Events

Table A.1: A List of SMCs used in the statistical study. Events were determined using the methodology set forth in DeJong and Clauer (2005). Start times are approximate and err on the side of cation, in that reconnection rates are balanced by the start time.

Steady Magnetospheric Convection Events		
Date (yyyymmdd)	Start time (UT)	Duration (hours)
19970210	1300	5.00
19970223	0200	5.00
19970505	0900	5.75
19970525	0000	4.25
19970619	0700	15.00
19970710	1450	9.00
19971109	2330	6.50
19971115	0530	4.50
19971210	2230	8.25
19980203	1600	9.00
19980214	2345	4.25
19980217	1445	8.50
19980219	2030	4.75
19980414	0800	4.50
19980420	0900	4.75
19980603	2100	3.75
19980614	0500	11.00
19980924	0500	4.00
19981104	1700	4.50
19990113	0200	9.00
19990428	0300	6.00
19990712	1100	7.00
19990808	0915	10.75
19990813	1430	5.50
19990823	0800	3.50
19991113	0130	3.50
19991114	1000	4.00
19991114	1430	3.50
19991123	0930	11.50
20000124	1600	4.25
20000310	1300	10.00
20000510	0300	17.00
20000821	1130	8.50
20000912	1330	6.00
20000930	0200	3.75
20001002	1000	5.00
20001026	0300	4.00
20001120	0730	7.00
20001120	1600	4.50
20001222	2200	6.75
20010108	1700	3.50
20010115	1230	7.50
20010120	1600	3.00
20010121	0930	7.50
20010126	0400	3.50
20010319	0500	4.00
20010512	0700	4.00
20011021	0730	10.50
20011113	1800	3.50
20011116	0330	10.50
20020117	1200	3.00

Table A.2: A List of isolated substorms the statistical studies. The highlighted events had good enough auroral data to use in the F_{pc} study (chapter 3). Onset times are determined by mid-latitude magnetometer data (Cai et al. 2006a)

Date (yyyymmdd)	Onset (UT)	Date (yyyymmdd)	Onset (UT)	Date (yyyymmdd)	Onset (UT)	Date (yyyymmdd)	Onset (UT)
19970313	0120	19980311	1302	19981211	1512	20000406	0302
19970313	1549	19980311	1556	19981216	0725	20000607	0752
19970313	1918	19980311	2252	19981216	1638	20040608	0631
19970314	2350	19980312	1327	19981228	2041	20000608	2134
19970316	1552	19980312	1808	19981229	2012	20000615	1924
19970317	1915	19980312	2200	19990309	0817	20000622	0002
19970318	0223	19980313	0643	19990309	1229	20000622	1957
19970318	2152	19880314	1158	19990309	1800	20000629	0028
19970322	1221	19980314	1517	19990317	1658	20000629	0611
19970324	2203	19980315	0145	19990318	1716	20000629	2223
19970325	0703	19980315	0552	19990325	2121	20000912	2049
19970325	1339	19980316	1501	19990327	2224	20000924	2027
19970327	1938	19980321	1902	19990331	2005	20000925	1632
19970328	1506	19980322	1643	19990401	0207	20000928	0327
19970329	2201	19980322	1918	19990403	1842	20000930	0532
19970330	0427	19980324	2041	19990403	2343	20000930	1350
19970330	1142	19980326	1629	19990404	2300	20001002	1534
19970405	2016	19980327	0811	19990405	0629	20001003	1235
19970405	2314	19980327	1558	19990407	0127	20001207	2152
19970406	1611	19980328	0301	19990407	0442	20001209	2106
19970406	2255	19980328	1008	19990407	1915	20001218	1607
19970407	0108	19980328	2317	19990612	0214	20001223	0427
19970407	1729	19980609	0801	19990912	1930	20001226	2053
19970407	2136	19980614	0411	19990913	0312	20001227	1532
19970407	2148	19980620	2317	19990913	1659	20010318	0151
19970619	2225	19980621	0935	19990913	1922	20010318	2122
19970627	1959	19980626	0451	19990914	0009	20010323	0059
19970628	0444	19980702	0019	19990915	0209	20010323	0409
19970629	0211	19980704	0513	19990915	0944	20010323	2008
19970909	0635	19980705	1840	19990926	1633	20010324	1234
19970909	1929	19980911	2220	19990926	2111	20010401	1747
19970909	2330	19980912	0638	19990927	0059	20010402	1604
19970910	1735	19980912	2224	19990927	0556	20010402	1814
19970910	2235	19980914	2110	19990927	1321	20010610	0118
19970912	0142	19980915	0640	19990927	1602	20010611	0214
19970912	1152	19980918	1809	19990927	2034	20010613	0258
19970912	1958	19980918	2314	19990928	0007	20010614	0012
19970913	0232	19980919	2318	19990928	2132	20010705	0614
19970913	0726	19980921	1223	19990929	0037	20010705	2234
19970913	2305	19980922	0610	19990930	1426	20010912	2208
19970914	0910	19980923	0554	19990930	2006	20010923	0556
19970915	1644	19980923	2207	19991001	1353	20010929	2202
19970918	0509	19980924	0320	19991001	1940	20011212	2141
19970918	1341	19980924	2111	19991207	0141	20011218	0023
19970920	0656	19980925	0607	19991207	0548	20011219	0129
19970923	2114	19980926	1956	19991207	1815	20011219	1019
19970927	1917	19980926	2254	19991213	0024	20011225	2117
19970929	0559	19980928	2037	20000310	2301	20011231	1929
19971215	1640	19981002	1923	20000323	1525	20011221	2145
19980101	0803	19981002	2158	20000401	1647	20020101	1801
19980311	0446	19981209	1505	20000404	0215	20020102	1624
19980311	0812	19981211	1308	20000404	2312	20020102	1942

Table A.3: A List of individual sawteeth used in the statistical studies. Once again the highlighted events had good enough auroral imaging for the F_{pc} study (Chapter 3). Onsets are determined using LANL SOPA data (Cai et al. 2006a)

Date (yyyymmdd)	Onset (UT)	Date (yyyymmdd)	Onset (UT)	Date (yyyymmdd)	Onset (UT)	Date (yyyymmdd)	Onset (UT)
19980626	0135	19990218	0703	20001106	1546	20020418	0756
19980626	0448	19990218	0923	20001106	1811	20020418	1131
19980723	0319	19990218	1243	20001106	2223	20020418	1406
19980723	0548	19990218	1431	20001107	0139	20020418	1631
19980723	0730	19990218	1814	20001107	0320	20020418	2104
19980723	0909	19990218	2021	20001129	0056	20020419	0834
19980723	1014	19990218	2300	20001129	0412	20020419	1205
19980723	1309	19990219	0130	20001129	0805	20020419	1446
19980723	1508	19990219	0935	20001129	1033	20020419	1824
19980723	1912	19990219	1223	20001129	1401	20020420	0145
19980826	1044	19990219	1455	20010320	0057	20020420	0340
19980826	1256	19990219	1619	20010320	0326	20020420	0615
19980826	1741	19990912	1901	20010320	0527	20020420	0926
19980826	2110	19990912	2138	20010320	0849	20020802	0030
19980826	2333	19990913	0109	20010320	1317	20020802	0211
19980827	0040	19990913	0322	20010320	1534	20020820	2036
19980827	0337	19990913	0639	20010320	1753	20020820	2227
19980827	0646	19990913	1013	20010331	1107	20020821	0142
19980918	1236	19990913	1253	20010331	1246	20020821	0317
19980918	1455	19990913	1651	20010331	1534	20020821	0640
19980918	1801	19990913	1923	20010331	1706	20020821	2227
19980925	0144	19990916	0501	20010331	1922	20020904	0523
19980925	0421	19990916	0701	20010331	2159	20020904	0901
19980925	0610	19990916	0909	20010411	1545	20020904	1151
19980925	0819	19990916	1100	20010411	1753	20020904	1511
19980925	1005	20000810	2300	20010411	2129	20020904	1736
19980925	1216	20000811	0043	20010412	0000	20021002	0026
19980925	1408	20000811	0155	20010412	0239	20021002	0414
19980925	1558	20000811	0415	20010412	0619	20021003	1412
19981019	0200	20000811	0637	20010412	0842	20021003	1606
19981019	0617	20000811	0817	20010508	1808	20021003	1922
19981019	0931	20000811	1032	20010508	2140	20021003	2222
19981019	1326	20000811	1334	20010509	0035	20021004	0140
19981019	1651	20000811	1846	20010509	0245	20021004	0633
19981019	1922	20000812	0303	20010509	0430	20021004	0839
19981109	0927	20000812	0547	20010512	1034	20021004	1045
19981109	1241	20000812	0757	20010512	1234	20021004	1252
19981109	1543	20000812	1021	20010512	1519	20021004	1800
19981109	1853	20000930	0840	20010512	1905	20021007	1555
19981113	0221	20000930	1050	20010817	1300	20021007	1906
19981113	0658	20000930	1639	20010817	1616	20021007	2228
19981113	1020	20000930	2004	20010817	1837	20021008	0409
19981113	1436	20001004	0609	20010817	2111	20021008	0957
19981113	1904	20001004	0934	20011021	1648	20021008	1402
19981113	2200	20001004	1150	20011021	1836	20021103	0609
19981211	0614	20001004	1400	20011021	2030	20021103	0810
19981211	0814	20001004	1706	20011021	2311	20021103	1214
19981211	1310	20001004	2001	20011022	1106	20021103	1727
19981211	1509	20001004	2128	20011022	1344	20021120	1712
19981211	1753	20001014	0656	20011022	1600	20021120	2014
19990113	1652	20001014	0955	20011022	1752	20021121	0356
19990113	2157	20001106	0948	20020418	0237	20021121	0719
19990218	0454	20001106	1302	20020418	0527	20021121	1111

APPENDIX B

List of Acronyms

ACE - Advanced Composition Explorer

AMIE - Assimilative Mapping of Ionospheric Electrodynamics

AE - Auroral Electrojet

AL - Auroral Lower

AU - Auroral Upper

BRI - Balanced Reconnection Interval

CME - Coronal Mass Ejection

CPCP - Cross Polar Cap Potential

FAC - Field Aligned Currents

FUV - Far Ultraviolet Imager

IMAGE - Imager for Magnetospheric-to-Aurora Global Exploration

IMF - Interplanetary Magnetic Field

LANL - Los Alamos National Lab

LBHl - Lyman Birge Hopfield long

LBHs - Lyman Birge Hopfield short

LFM - Lyon-Fedder-Mobarry

MHD - Magneto-Hydro-Dynamics

MLT - Magnetic Local Time

NENL - Near Earth Neutral Line

SMC - Steady Magnetospheric Convection

SOPA - Synchronous Orbit Particle Analyzer

UT - Universal Time

UVI - Ultraviolet Imager

WIC - Wideband Imaging Camera

BIBLIOGRAPHY

BIBLIOGRAPHY

Akasofu, S.-I., The development of the auroral substorm, *Planet. Space Sci.*, *101*, 273, 1964.

Axford, W., and C. Hines, A unifying theory of high-latitude geophysical phenomena and gemagnetic storms, *Can. J. Phys.*, *39*, 1433, 1961.

Axford, W. I., Viscous interaction between the solar wind and the earth's magnetosphere, *Planetary Space Science*, *12*, 45–53, 1964.

Baker, J., C. Clauer, A. Ridley, V. Papitashvili, M. Brittnacher, and P. Newell, The nightside polarward boundary of the auroral oval as seen by dmsp and the ultraviolet imager, *J. Geophys. Res.*, *105*, 21,267–23,280, 2000.

Belian, R. D., T. E. Cayton, and G. D. Reeves, Quasi-periodic global substorm-generated variations observed at geosynchronous orbit, in Space Plasmas: Coupling Between Small and Medium Scale Processes, Geophys. Monogr. Ser., vol. 86, *edited by M. Ashour-Abdalla and T. Chang and P. Dusenburg, p. 143*, AGU, Washington, D. C., 1995.

Borovsky, J. E., and M. H. Denton, Differences between CME-driven storms and CIR-driven storms, *Journal of Geophysical Research (Space Physics)*, *111*, 7–+, doi:10.1029/2005JA011447, 2006.

Boudouridis, A., E. Zesta, R. Lyons, P. C. Anderson, and D. Lummerzheim, Effect of solar wind pressure pulses on the size and strength of the auroral oval, *J.Geophys. Res.*, *108*, 8012–+, doi:10.1029/2002JA009373, 2003.

Boudouridis, A., E. Zesta, L. Lyons, P. Anderson, and D. Lummerzheim, Magnetospheric reconnection driven by solar wind pressure fronts, *Annales Geophysicae*, *22*, 1367–1378, 2004.

Brittnacher, M., M. Fillingim, G. Parks, G. Germany, and J. Spann, Polar cap area and boundary motion during substorms, *J. Geophys. Res.*, *104*, 12,251, 1999.

Burton, R., R. L. McPherron, and C. T. Russell, An empirical relationship between interplanetary conditions and Dst, *J. Geophys. Res.*, *80*, 4204, 1975.

Cai, X., C. Clauer, and A. Ridley, Statistical analysis of ionospheric potential patterns for isolated substorms and sawtooth events, *Ann. Geophysicae*, *24*, 1977–1991, 2006a.

Cai, X., M. Henderson, and C. Clauer, A statistical study of magnetic dipolarization for sawtooth events and isolated substorms at geosynchronous orbit with goes data, *Ann. Geophysicae*, *24*, 3481–3490, 2006b.

Carlson, H., and A. Egeland, The aurora and the auroral ionosphere *edited by M.G. Kivelson and C.T. Russell, p. 459-500*, Cambridge University Press, 1995.

Chamberlain, J. W., *Physics of the aurora and airglow*, International Geophysics Series, New York: Academic Press, 1961, 1961.

Chua, D., G. Parks, M. Brittnacher, W. Peria, G. Germany, J. Spann, and C. Carlson, Energy characteristics of auroral electron precipitation: A comparison of substorms and pressure pulse related auroral activity, *J. Geophys. Res.*, *106*, 5945–5956, doi:10.1029/2000JA003027, 2001.

Clauer, C., and R. McPherron, Mapping the local time-universal time development of magnetospheric substorms using mid-latitude magnetic observations, *J. Geophys. Res.*, *79*, 2811–2820, 1974.

Clauer, C. R., X. Cai, D. Welling, and A. DeJong, Characterizing the april 18, 2002 storm-time sawtooth events using ground magnetic data, *J. Geophys. Res.*, *111*, doi:10.1029/2005JA011099, 2006.

Cowley, S., Magnetic Reconnection, in Solar System Magnetic Fields *edited by R.E. Priest, p. 121*, Dodrecht:Reidel, 1986.

Cowley, S., and M. Lockwood, Excitation and decay of solar wind-driven flow in the magnetophere-ionosphere system, *Ann. Geophysicae*, *10*, 103–115, 1992.

Cummings, W. D., J. N. Barfield, and P. J. C. Jr., Magnetospheric substorms observed at the synchronous orbit, *J. Geophys. Res.*, *73(21)*, 6687–6698, 1968.

DeJong, A., and C. Clauer, Polar uvi images to study steady magnetospheric convection events: Initial results, *Geophys. Res. Lett.*, *32*, 24,101, doi:10.1029/2005GL024498, 2005.

Dungey, J., Interplanetary magnetic field and the auroral zones, *Phys. Rev. Lett.*, *93*, 47, 1961.

Erickson, K. N., R. L. Swanson, R. J. Walker, and J. R. Winckler, A study of magnetosphere dynamics during auroral electrojet events by observations of energetic electron intensity changes at synchronous orbit, *J. Geophys. Res.*, *84*, 931–942, 1979.

Fillingim, M., G. Parks, L. J. Chen, M. Brittenacher, G. A. Germany, J. F. Spann, D. Larson, and R. Lin, Coincident polar/uvi and wind observations of pseudobreakups, *Geophys. Res. Lett.*, *27*, 2000.

Goodrich, C. C., T. I. Pulkkinen, J. G. Lyon, and V. G. Merkin, Magnetospheric convection during intermediate driving: Sawtooth events and steady convection intervals as seen in Lyon-Fedder-Mobarry global MHD simulations, *J. Geophys. Res.*, *112*, 8201–+, doi:10.1029/2006JA012155, 2007.

Hargreaves, J. K., *The solar-terrestrial environment. an introduction to geospace - the science of the terrestrial upper atmosphere, ionosphere and magnetosphere*, Cambridge atmospheric and space science series, Cambridge: Cambridge University Press, —c1992, 1992.

Henderson, M. G., The may 2-3, 1986 cdaw-9c interval: A sawtooth event, *Geophys. Res. Lett.*, *31(11)*, doi:10.1029/2004GL019941, 2004.

Henderson, M. G., G. D. Reeves, R. M. Skoug, M. F. Thomsen, M. H. Denton, S. B. Mende, T. J. Immel, P. C. Brandt, and H. J. Singer, Magnetospheric and auroral activity during the april 18, 2002 sawtooth event, *J. Geophys.Res.*, *111(A1)*, doi:10.1029/2005JA011111, 2006a.

Henderson, M. G., et al., Substorms during the 1011 august 2000 sawtooth event, *J. Geophys. Res.*, *111*, doi:A06206, doi:10.1029/2005JA011366, 2006b.

Hill, T., Magnetic merging in a collisionless plasma, *J. Geophys. Res.*, *80*, 4689–4699, 1975.

Holzer, R. E., R. L. McPherron, and D. A. Hardy, A quantitative empirical model of the magnetospheric flux transfer process, *J. Geophys. Res.*, *91*, 3287–3293, 1986.

Huang, C.-S., G. D. Reeves, J. E. Borovsky, R. M. Skoug, Z. Y. Pu, and G. Le, Periodic magnetospheric substorms and their relationship with solar wind variations, *J. Geophys. Res.*, *108(A6)*, doi:10.1029/2002JA009704, 2003.

Huang, C.-S., G. Le, and G. Reeves, Periodic magnetospheric substorms during fluctuating interplanetary magnetic field b_z, *Geophy. Res. Lett.*, *31*, doi:L14801, doi:10.1029/2004GL020180, 2004.

Huang, C.-S., G. D. Reeves, G. Le, and K. Yumoto, Are sawtooth oscillations of energetic plasma particle fluxes caused by periodic substorms or driven by solar wind pressure enhancements?, *J. Geophys. Res.*, *110*, doi:10.1029/2005JA011018, 2005.

Hughes, J. M., and W. A. Bristow, SuperDARN observations of the Harang discontinuity during steady magnetospheric convection, *J. Geophys. Res.*, *108*, 1185–+, doi:10.1029/2002JA009681, 2003.

Hughes, W. J., The mangetopause, magnetotail, magnetic reconnection, in Introduction to Space Physics *edited by M.G. Kivelson and C.T. Russell, p. 227-285*, Cambridge University Press, 1995.

Immel, T., J. Craven, and A. Nicholas, An empirical model of the OI FUC dayglow from DE-1 images, *J. Atm. Solar Terr. Phys.*, *62*, 47, 2000.

Jacobs, J. A., Geomagnetic micropulsations., *Physics and Chemistry in Space*, *1*, 1970.

Johnson, C., Ion and neutral composition of the ionosphere, *Annals of the IQSY*, *5*, 197–213, 1969.

Jones, A. V., *Aurora*, D. Reidel, Dordrecht, The Netherlands, 1974.

Joselyn, J. A., and B. T. Tsurutani, Geomagnetic sudden impulses and storm sudden commencements, *Eos*, *71*, 1808, 1990.

Kan, J. R., and L. C. Lee, Energy coupling function and solar wind-magnetosphere dynamo, *Geophys. Res. Let.*, *6*, 577–580, 1979.

Kan, J. R., L. Zhu, and S.-I. Akasofu, A theory of substorms - Onset and subsidence, *J. Geophys. Res.*, *93*, 5624–5640, 1988.

Kelley, M., *The Earth's Ionosphere*, Academic Press, Inc., San Diego, 1989.

Kokubun, S., and R. L. McPherron, Substorm signatures at synchronous altitude, *J. Geophys. Res.*, *86*, 11,265–11,277, 1981.

Koshkinen, H. E. J., R. Lopes, R. Pellinen, T. I. Pulkkinen, D. N. Baker, and T. Bosinger, Pseudobreakup and substorm growth phase in the ionosphere and magnetosphere, *J. Geophys. Res*, *98*, 5801–5813, 1993.

Koskinen, H. E. J., R. E. Lopez, R. J. Pellinen, T. I. Pulkkinen, D. N. Baker, and T. Bosinger, Pseudobreakup and substorm growth phase in the ionosphere and magnetosphere, *J. Geophys. Res.*, *98*, 5801–5813, 1993.

Kullen, A., and T. Karlsson, On the relation between solar wind, pseudobreakups, and substorms, *J. Geophys. Res.*, *109*, 12,218–+, doi: 10.1029/2004JA010488, 2004.

Lopez, R., M. Wiltberger, S. Hernandez, and J. Lyon, Solar wind density control of energy transfer to the magnetopause, *Geophys. Res. Lett.*, in Press, 2004.

Lui, A. T. Y., A synthesis of magnetospheric substorm models, *J. Geophys. Res.*, *96*, 1849–1856, 1991.

Lui, A. T. Y., A. Mankofsky, C.-L. Chang, K. Papadopoulos, and C. S. Wu, A current disruption mechanism in the neutral sheet - A possible trigger for substorm expansions, *Geophys. Res. Lett.*, *17*, 745–748, 1990.

McPherron, R. L., Physical Processes Producing Magnetospheric Substorms and Magnetic Storms, in *Geomagnetism,* edited by J. Jacobs*, pp. 593-739*, Academic Press, London, 1991.

McPherron, R. L., C. T. Russell, and M. P. Aubry, Satellite studies of the magnetospheric substorms on august 16, 1968, 9, phenomenological model for substorms, *J. Geophys. Res*, *78*, 3131–3149, 1973.

McPherron, R. L., T. Teresawa, and A. Nishida, Solar wind triggering of substorm expansion onset, *Journal of Geomagnetism and Geoelectricity*, *38*, 1089–1108, 1986.

McPherron, R. L., J. M. Weygand, and T.-S. Hsu, Response of the Earth's magnetosphere to changes in the solar wind, *Journal of Atmospheric and Terrestrial Physics*, *70*, 303–315, doi:10.1016/j.jastp.2007.08.040, 2008.

Meier, R. R., R. R. Conway, P. D. Feldman, D. J. Strickland, and E. P. Gentieu, Analysis of nitrogen and oxygen far ultraviolet auroral emissions, *J. Geophys. Res.*, *87*, 2444–2452, 1982.

Mende, S. B., et al., Far ultraviolet imaging from the IMAGE spacecraft. 2. Wideband FUV imaging, *Space Science Reviews*, *91*, 271–285, 2000.

Milan, S., A simple model of the flux content of the distant magnetotail., *J. Geophys. Res.*, *109*, A07,210, doi:10.1029/2004JA010397, 2004.

Milan, S., M. Lester, S. Cowley, K. Oksavik, R. Brittnacker, M. andGreenwald, G. Sofko, and J. Villain, Variations in the polar cap area during two substorm cycles, *Ann. Geophysicae*, *21*, 1121 –1140, 2003.

Milan, S., J. Wild, A. Grocott, and N. Draper, Space- and ground-based investigations of solar wind-magntosphere-ionosphere coupling, *Ad. Space Res.*, *38*, 1671–1677, 2006.

Milan, S., G. Provan, and B. Hubert, Mangetic flux transport in the dungey cycle: A servey of dayside and nightside reconnection rates, *J. Geophys. Res.*, *112*, doi:10:1029/2006JA011642, 2007.

Ober, D. M., G. R. Wilson, W. J. Burke, N. C. Maynard, and K. D. Siebert, Magnetohydrodynamic simulations of transient transpolar potential responses to solar wind density changes, *J. Geophys. Res.*, *112*, 10,212–+, doi: 10.1029/2006JA012169, 2007.

O'Brien, T., S. Thompson, and R. McPherron, Steady magnetospheric convection: Statistical signatures in the solar wind and ae, *Geophys. Res. Lett.*, *29*, 18,843, doi:10:1029/2001GL019113, 2002.

Olson, J. V., Pi2 pulsations and substorm onsets: A review, *J. Geophys. Res.*, *104*, 17,499–17,520, doi:10.1029/1999JA900086, 1999.

Parker, E. N., Dynamics of the interplanetary gas and magnetic fields, *Astrophysical Journal*, *128*, 664, 1958.

Parker, E. N., The magnetohydrodynamic treatment of the expanding corona, *Astrophysical Journal*, *132*, 175, 1960.

Perreault, P., and S.-I. Akasofu, A study of geomagnetic storms., *Geophys. J. R. Astron. Soc., Vol. 54, p. 547 - 573*, *54*, 547–573, 1978.

Pulkkinen, T. I., C. C. Goodrich, and J. G. Lyon, Solar wind electric field driving of magnetospheric activity: Is it velocity or magnetic field?, *Geophys. Res. Let.*, *34*, 21,101–+, doi:10.1029/2007GL031011, 2007.

Pytte, T., R. L. McPherron, E. W. Hones, Jr., and H. I. West, Jr., Multiple-satellite studies of magnetospheric substorms - Distinction between polar magnetic substorms and convection-driven negative bays, *J. Geophys. Res.*, *83*, 663–679, 1978.

Reeves, G. D., M. G. Henderson, P. S. McLachlan, and R. D. Belian, *Radial propagation of substorm injections, in Proceedings of the Third International Conference on Substorms*, ESA SP-339, 579-584 pp., Eur. Space Agency Spec. Publ., 1996.

Reeves, G. D., M. F. Thomsen, M. G. Henderson, R. M. Skoug, J. E. Borovsky, J.-M. Jahn, C. J. Pollock, D. G. Brandt, and S. B. Mende, Global "sawtooth" activity in the april 2002 geomagnetic storm, pp. paper presented at 2002 AGU Fall Meeting, American Geophsical Union, San Francisco, CA, 6–10 December, 2002.

Ridley, A. J., and E. Kihn, Polar cap index comparison with amie cross polar cap potential, electric field and polar cap area, *Geophys. Res. Lett*, *31*, L07,801, doi:10.1029/2003GL019113, 2004.

Rothwell, P. L., L. P. Block, C.-G. Falthammar, and M. B. Silevitch, A new model for substorm onsets - The pre-breakup and triggering regimes, *Geophys. Res. Lett.*, *15*, 1279–1282, 1988.

Russell, C. T., and R. L. McPherron, The Magnetotail and Substorms, *Space Science Reviews*, *15*, 205, 1973.

Sauvaud, J.-A., and J. R. Winckler, Dynamics of plasma, energetic particles, and fields near synchronous orbit in the nighttime sector during magnetospheric substorms, *J. Geophys. Res.*, *85*, 2043–2056, 1980.

Sergeev, V., On the state of the magnetosphere during prolonged periods of southward oriented imf, *Phys. Solariterr. Potsdam*, *5*, 39, 1977.

Sergeev, V., R. Pellinen, and T. Pulkkinen, Steady magnetospheric convection: a review of recent results, *Space Sci. Rev.*, *75*, 551–604, 1996.

Sergeev, V. A., and W. Lennartsson, Plasma sheet at X ˜ -20 Re during steady magnetospheric convection, *Planet. Space Sci.*, *36*, 353–370, doi:10.1016/0032-0633(88)90124-9, 1988.

Siscoe, G., and T. Huang, Polar cap inflation and deflation, *J. Geophys. Rev.*, *90*, 543–547, 1985.

Swanson, R. L., Electron intensity and magnetic field changes at synchronous orbit for the auroral electrojet, Ph.D. thesis, Univ. of Minn., Mineapolis, 1978.

Tanskanen, E. I., J. A. Slavin, D. H. Fairfield, D. G. Sibeck, J. Gjerloev, T. Mukai, A. Ieda, and T. Nagai, Magnetotail response to prolonged southward IMF Bz intervals: Loading, unloading, and continuous magnetospheric dissipation, *J. Geophys. Res.*, *110*, 3216–+, doi:10.1029/2004JA010561, 2005.

Torr, M., et al., A far ulraviolet imager for the international solar - terrestrial physics mission, *Space Sci. Rev.*, *71*, 329, 1995.

Walker, R. J., R. L. Swanson, J. R. Winckler, and K. N. Erickson, Substorm-associated particle boundary motion at synchronous orbit, *J. Geophys. Res.*, *81(5)*, 5541–5550, 1976.

Weimer, D., Models of high-latitude electric potentials derived with a least error fit of spherical harmonic coefficients, *J. Geophys. Res.*, *100*, 19,595, 1995.

Weimer, D. R., Correction to "Predicting interplanetary magnetic field (IMF) propagation delay times using the minimum variance technique", *J. Geophys. Res.*, *109*, 12,104–+, doi:10.1029/2004JA010691, 2004.

Weimer, D. R., D. M. Ober, N. C. Maynard, W. J. Burke, M. R. Collier, D. J. McComas, N. F. Ness, and C. W. Smith, Variable time delays in the propagation of the interplanetary magnetic field, *J. Geophys. Res.*, *107*, doi:10.1029/2001JA009102, 2002.

Weimer, D. R., D. M. Ober, N. C. Maynard, M. R. Collier, D. J. McComas, N. F. Ness, C. W. Smith, and J. Watermann, Predicting interplanetary magnetic field (imf) propagation delay times using the minimum variance technique, *J. Geophys. Res.*, *108*, doi:doi:10.1029/2002JA009405, 2003.

Yahnin, A., et al., Features of steady magnetospheric convection, *J. Geophys. Res.*, *99*, 4039–4051, 1994.